



COMPUTATIONAL STUDY OF VOLTAGE-GATED SODIUM/POTASSIUM CHANNELS

vom Fachbereich Biologie
der Technischen Universität Darmstadt

zur Erlangung des Grades
Doctor rerum naturalium (Dr. rer. nat.)

genehmigte Dissertation von

DANIEL BAUER

Erstgutachter: Prof. Dr. Kay Hamacher

Zweitgutachter: Prof. Dr. Gerhard Thiel

DARMSTADT 2021

This document was typeset with [Xe_LTeX](#) and a modified version of [Tufte-LaTeX](#). The bibliography was managed with [Zotero](#) and processed by [Biblatex](#). Used fonts were Vollkorn (serif), Gillius ADF No2 (sans serif) and TeX Gyre Cursor (monospace). Figures and images were generated with [Matplotlib](#), [PyMOL](#), and [MarvinSketch](#).

Bauer, Daniel: Computational Study of Voltage-gated Sodium/Potassium Channels
Darmstadt, Technische Universität Darmstadt,
Jahr der Veröffentlichung der Dissertation auf TUprints: 2021
URN: [urn:nbn:de:tuda-tuprints-186114](https://nbn-resolving.org/urn:nbn:de:tuda-tuprints-186114)
Tag der mündlichen Prüfung: 03. December 2021

 **CC BY-SA 4.0 International**

Attribution - ShareAlike 4.0 International

<https://creativecommons.org/licenses/by-sa/4.0/>

Abstract

Ion channels play a fundamental role in all biological entities ranging from small viruses up to complex animals. They are responsible for a vast number of different processes including virus uptake, regulation of the cells ionic balance, proliferation and cell signaling. Potassium channels are selective ion channels that primarily conduct potassium ions. Most channels of this subfamily are not permanently open, but their conductance can be regulated. This allows them to open or close in response to a broad range of environmental conditions.

In humans, hyperpolarization-activated cyclic nucleotide-gated (HCN) channels are crucial for various biological processes of the neuronal and cardiovascular system. In the heart, they are responsible for the pacemaker current, which drives the action potential in cardiac pacemaker cells. In the brain, HCN channels contribute to various regulatory functions in neurons and are involved in processes such as the sleep-wake cycle, learning, and brain development. Accordingly, malfunctioning of HCN channels is linked to severe diseases such as arrhythmia and epilepsy.

For the present work, molecular dynamics (MD) simulations were used to study several aspects of HCN channels. In the first part, comparative MD simulations were carried out to investigate how the substitution of amino acids at key positions of the HCN₁ gene alters the channels structure and dynamics. In combination with experimental data, this information can provide insight into fundamental principles of channel functioning and assist in the understanding and treatment of HCN-mediated diseases. Therefore, several *de novo* mutations with clinical relevance were investigated. Similar mutational studies were also used to elucidate the role of the conserved HCN domain which is unique for HCN channels. It could be shown that mutation of a single amino acid can disrupt the mechanical connection between domains of the channel and thereby alter gating characteristics.

The second part of this work focused on ion conductance. HCN channels discriminate only moderately between potassium and sodium and show a relatively low conductance. Using MD simulations with an applied electric field, it was possible to obtain insights into a unique mechanism that underlies ion conduction in HCN channels: the presented HCN-specific soft knock-on mechanism is an alternation between two distinct states with either two or one ion bound to the selectivity filter (SF) and separated by a single water molecule. Within this model, a theory is presented on how the low selectivity in HCN channels is a result of potassium and sodium binding to the same binding sites within the SF, but with different affinity. Finally, free energy calculations show that the experimentally determined low conductance of HCN channels is a result of high energy barriers within the SF which are not compatible with diffusion-limited conductance.

Zusammenfassung

Ionenkanäle spielen eine wichtige Rolle in allen Lebensformen—von kleinen Viren bis hin zu komplexen Tieren. Hier sind sie für ein breites Spektrum an verschiedenen Prozessen wie der zellulären Aufnahme von Viren, der Regulation des Ionengleichgewichts der Zelle, der Zellproliferation und der interzellulären Kommunikation verantwortlich. Kaliumkanäle sind selektive Ionenkanäle, die hauptsächlich Kaliumionen leiten. Die meisten Kanäle dieser Unterfamilie sind nicht ständig geöffnet sondern ihre Leitfähigkeit kann reguliert werden. Dadurch können sie auf verschiedene Umweltbedingungen reagieren und sich in Abhängigkeit von äußeren Bedingungen öffnen oder schließen.

Im Menschen sind *hyperpolarization-activated cyclic nucleotide-gated (HCN)* Kanäle entscheidend für unterschiedlichste biologische Prozesse des neuronalen und kardiovaskulären Systems. In den *Pacemaker*-Zellen des Herzens, die als biologischer Herzschrittmacher dienen, steuern sie die rhythmisch auftretenden Aktionspotentiale die das Herz schlagen lassen. Im Gehirn tragen HCN-Kanäle zu verschiedenen regulatorischen Funktionen der Neuronen bei und sind an Prozessen wie dem Schlaf-Wach-Rhythmus, dem Lernen oder der Entwicklung des Gehirns beteiligt. Funktionsstörungen von HCN-Kanälen werden daher mit schweren Krankheiten wie Herzrhythmusstörungen und Epilepsie verbunden.

In der vorliegenden Studie wurden *Molecular dynamics (MD)* Simulationen zur Untersuchung von zwei wesentlichen Aspekten von HCN-Kanälen durchgeführt. Im ersten Teil wurde mithilfe von MD Simulationen untersucht, wie sich die Substitution von Aminosäuren an wichtigen Positionen des HCN₁ Gens auf die Struktur und Dynamik der Kanäle auswirkt. In Kombination mit experimentellen Daten können diese Informationen Aufschluss über grundlegende Prinzipien der Kanalfunktion geben sowie zum Verständnis und zur Behandlung von Krankheiten beitragen. Aus diesem Grund wurden mehrere neu beschriebene Mutationen mit klinischer Relevanz untersucht. Ähnliche Mutationsstudien wurden auch genutzt, um die Rolle der in HCN Kanälen einzigartigen und konservierten HCN Domäne zu beschreiben. Es konnte gezeigt werden, dass die Mutation einer einzigen Aminosäure die mechanische Verbindung zwischen den Domänen des Kanals, und damit die Öffnungsfähigkeit der Kanäle, beeinflussen kann.

Der zweite Teil dieser Studie konzentrierte sich auf die Ionenleitung. HCN Kanäle unterscheiden nur in geringem Maße zwischen Kalium und Natrium und weisen eine relativ geringe Leitfähigkeit auf. Mithilfe von MD Simulationen mit einem angelegten elektrischen Feld war es möglich, Einblicke in den einzigartigen Mechanismus zu erhalten, der der Ionenleitung in HCN-Kanälen zugrunde liegt: Der vorgestellte HCN-spezifische *Soft knock-on* Mechanismus ist eine Alternation zwis-

chen zwei Zuständen in denen entweder ein oder zwei Ionen an dem Selektivitätsfilter (SF) gebunden sind. Dabei sind die Ionen räumlich durch ein Wassermolekül getrennt. Innerhalb dieses Modells wird eine Theorie vorgestellt, die die geringe Selektivität in HCN Kanälen darauf zurück führt, dass sowohl Kalium als auch Natrium an die gleichen Bindungsstellen innerhalb des SF binden—dies jedoch mit unterschiedlicher Affinität. Dies wird durch Berechnungen der freien Energie ergänzt, die die experimentell ermittelte niedrige Leitfähigkeit von HCN Kanälen auf hohe Energiebarrieren innerhalb des SF zurück führt, die eine diffusionslimitierte Ionenleitung nicht erlauben.

Contents

I	INTRODUCTION	I
1	PROLOGUE	3
1.1	Thesis Outline	3
1.2	Publications	4
2	VOLTAGE-GATED POTASSIUM CHANNELS	7
2.1	Classification and Structure	7
2.2	Voltage-dependency and Gating	9
2.3	Ligand-dependency	11
2.4	Conduction and Selectivity	12
3	HCN CHANNELS AND THEIR ROLE IN CARDIOVASCULAR AND NEUROLOGICAL DISEASES	15
3.1	HCN Gene Family and Pathophysiology	15
3.2	Biological Role	15
3.3	Functional Characterization	17
3.4	Channel Structure	18
4	THEORY AND METHODS	21
4.1	Molecular Dynamics Simulations	21
4.2	Molecular Docking	28
4.3	Transition State Theory	29
II	RESULTS	31
5	MODELING MUTATIONS IN HCN CHANNELS	33
5.1	Introduction	33
5.2	Mutation G391C/S/D	34
5.3	Mutation F109W/M/V/A/E	38
6	ION CONDUCTION IN HCN CHANNELS	41
6.1	Introduction	41
6.2	Characterization of the HCN ₄ Pore	42
6.3	Ion Conduction Mechanism	45
6.4	Free Energy Calculations	51
6.5	Ion Permeation Strictly Follows Soft Knock-on	59
III	FINAL REMARKS	61
7	CONCLUSION	63
8	REFERENCES	67
IV	APPENDIX	85
A	ABBREVIATIONS	87
B	SEQUENCE ALIGNMENT OF HCN CHANNELS	89
C	SIMULATION DETAILS	93
D	ADDITIONAL DATA	99
	ACKNOWLEDGEMENTS	III
	EHRENWÖRTLICHE ERKLÄRUNG	III

List of Figures

1.1	A stylized depiction of HCN ₄ with bound ions.	3
2.1	Classification of cation channels	8
2.2	Schematic overview of potassium channels	9
2.3	Domain-swapped and non-domain-swapped channels	9
2.4	Depiction of the membrane potential	10
2.5	Free energy profile of voltage-dependent gating	10
2.6	Voltage-dependent gating mechanism	11
2.7	Ligand cooperativity in HCN ₂	11
2.8	Different conduction models	12
2.9	Pore domain of KcsA	12
2.10	Selectivity filter of different ion channels	13
3.1	Phylogenic tree of HCN channels	15
3.2	Pacemaker action potential	16
3.3	HCN channel structure	18
3.4	HCN selectivity filter	18
4.1	Molecular dynamics workflow	21
4.2	Leap-frog integration	22
4.3	Molecular dynamics potential functions	22
4.4	Molecular dynamics simulation box	25
4.5	Example of a biasing potential	26
4.6	Lamarckian genetic algorithm	28
4.7	Transition state theory	29
5.1	Overview of investigated HCN ₁ mutations	34
5.2	Functional characterization of HCN ₁ _{G391C/S/D}	35
5.3	HCN ₁ _{G391C/S/D} pore radii	35
5.4	HCN ₁ _{G391C/S} hydrogen bonding	36
5.5	HCN ₁ _{G391C/S/D} pore solvation	36
5.6	Ions in homo- and heterozygous HCN ₁ _{TMD,G391D}	37
5.7	Functional characterization of HCN ₂ _{F151W/M/V/A/E}	38
5.8	HCN ₁ _{F109W/M/V/A/E} side chain distances	39
5.9	HCN ₁ _{F109W/M/V/A/E} solvent RDFs for residue 109	39
6.1	HCN ₄ pore and selectivity filter comparison	41
6.2	Sodium binding in KcsA	41
6.3	Open and closed HCN ₄ pore radii	42
6.4	HCN ₄ pore solvation	43
6.5	HCN ₄ pore water exchange rate	43
6.6	Structural formula of ivabradine.	44
6.7	Ivabradine docking	44
6.8	Potassium conduction mechanism	46
6.9	Sodium in the HCN ₄ SF	47
6.10	Mixed sodium conduction mechanism	47

6.11	Selectivity filter flexibility	50
6.12	Sampling multi-ion PMFs in HCN ₄	51
6.13	Free energy landscape: K ⁺ /K ⁺ system	52
6.14	Different K ⁺ conduction mechanisms	53
6.15	1D projection: K ⁺ /K ⁺ energy landscape	53
6.16	Free energy landscape and 1D MFEP: K ⁺ /K ⁺ /K ⁺ system	54
6.17	Free energy landscape: Na ⁺ /Na ⁺ /Na ⁺ conduction	56
6.18	Mixed ion species free energy landscapes	58
6.19	Water intercalation during umbrella simulations	59
7.1	Permeation models in potassium- and HCN channels	64
B.1	Alignment of several HCN channels	91
D.1	HCN _{I_{G301C/S/D}} simulation snapshots	99
D.2	HCN _{I_{G301C/S/D}} RMSD	100
D.3	HCN _{I_{G301C/S/D}} RMSF	100
D.4	HCN _{I_{TMD,G391D}} simulation snapshots	101
D.5	HCN _{I_{TMD,G391D}} RMSD	101
D.6	HCN _{I_{TMD,G391D}} RMSF	102
D.7	HCN _{I_{F109W/M/V/A/E}} RMSD	102
D.8	HCN _{I_{F109W/M/V/A/E}} RMSF	103
D.9	HCN _{I_{F109W/M/V/A/E}} simulation snapshots	103
D.10	Ion conduction trajectories under different conductions	104
D.11	Selectivity filter backbone widths	105
D.12	Umbrella sampling start configurations	106
D.13	Umbrella sampling convergence	107

List of Tables

5.1	HCN _{I_{F109M/W/V/A/E}} functional correlation	39
6.1	Conductance statistics during HCN ₄ simulations	48
6.2	Measured conductance in HCN channels.	54
6.3	Free energy differences of potassium conduction	55
6.4	Free energy differences of sodium conduction	57
C.1	Mutational studies simulation systems.	93
C.2	Ion conduction simulation systems.	97
C.3	Umbrella simulation systems.	98
D.1	Free energy differences of mixed PMFs	108

Part I

Introduction

CHAPTER 1

Prologue

Ion channels play a fundamental role in all biological entities ranging from small viruses such as SARS-CoV-2 up to complex organisms like as humans with their trillions of interconnected cells. HCN channels are representatives of this protein superfamily. From a basic research point of view, they provide an interesting target to transfer, test and expand our knowledge derived from structurally less complex channels to more complex ones. Furthermore, HCN channels are of special interest due to their important role in a broad range of human physiological processes—and consequently because channelopathies involving HCN channels are related to various severe diseases. Therefore, HCN channels have been studied extensively by structural biologists and in the context of neuroscience. Nevertheless, key features such as gating, kinetics, and ion selectivity are only poorly understood for this channel species.

1.1 THESIS OUTLINE

This thesis aims to further our understanding of ion channels in general, and HCN channels in particular. For these channels, the effect of mutation of selected residues with severe impact on channel functioning in human and experiment were evaluated. Here, computational studies showed itself as a valuable tool to close the gap between the static picture of a resolved 3D structure and macroscopic channel recordings. Of special interest for these studies were also the selectivity filter, which is responsible for the discrimination of different ion species through a not yet fully understood mechanism.

The remainder of the introduction ([Part I](#)) describes the biological background and lays the theoretical groundwork for this PhD thesis:

- In [Chapter 2](#), I describe the basic principles underlying ion channel-mediated transport through cell membranes. This includes an overview over important features like voltage- and ligand-dependent gating, selectivity, and conduction kinetics.
- In [Chapter 3](#) follows an overview of HCN channels, which were the focus of my studies.
- In [Chapter 4](#), I describe the theory and methods used throughout this work. This part focuses on the concept of MD simulations and its application to answer the questions outlined above. It also gives a brief introduction in other concepts such as molecular docking and transition state theory (TST).

"... Ion channels are involved in every thought, every perception, every movement, every heartbeat."
- Clay M. Armstrong (1999)

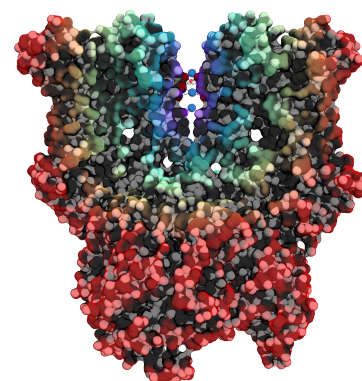


Figure 1.1: A stylized depiction of HCN4 with bound ions.

In [Part II](#), the results of my research will be presented:

- In [Chapter 5](#), I describe the impact of mutation of two key residues of HCN1: mutation of G391 leads to epileptic encephalopathy in human and I investigated how missense mutations of this residue affect the channel structure and dynamics. Residue F109 is part of the unique HCN domain and comparative MD simulations were used to investigate its importance for channel gating.
- In [Chapter 6](#), I present my findings on ion selectivity and conduction in HCN channels. Here, I show how the unique shape of the HCN selectivity filter results in weak potassium-selectivity and slow conduction kinetics. Furthermore, a theory that explains the potassium-dependence of sodium conduction is presented.

Finally, [Part III](#) will summarize all results and give a final conclusion.

1.2 PUBLICATIONS

The following thesis draws on the ideas and writing of the following published works. They are the result of my own research performed during my doctoral studies together with several coworkers and collaborators:

Marini, C., Porro, A., Rastetter, A., Dalle, C., Rivolta, I., **Bauer, D.**, et al. (2018)

[HCN1 mutation spectrum: from neonatal epileptic encephalopathy to benign generalized epilepsy and beyond](#). *Brain* 141.11, pp. 3160–3178. DOI: [10.1093/brain/awy263](https://doi.org/10.1093/brain/awy263).

Porro, A., Saponaro, A., Gasparri, F., **Bauer, D.**, Gross, C., Pisoni, M., et al. (2019)

[The HCN domain couples voltage gating and cAMP response in Hyperpolarization-activated Cyclic Nucleotide-gated channels](#). *eLife* 8, e49672. DOI: [10.7554/eLife.49672](https://doi.org/10.7554/eLife.49672).

Jenewein, T., Kanner, S. A., **Bauer, D.**, Hertel, B., Colecraft, H. M., Moroni, A., et al. (2020)

[The mutation L69P in the PAS domain of the hERG potassium channel results in LQTS by trafficking deficiency](#). *Channels* 13.1, pp. 163–174. DOI: [10.1080/19336950.2020.1751522](https://doi.org/10.1080/19336950.2020.1751522).

Hauf, K., Barsch, L., **Bauer, D.**, Buchert, R., Armbruster, A., Frauenfeld, L., et al. (2020)

[GlyT1 encephalopathy: Characterization of presumably disease causing GlyT1 mutations](#). *Neurochemistry International* 139, p. 104813. DOI: [10.1016/j.neuint.2020.104813](https://doi.org/10.1016/j.neuint.2020.104813).

Schmidt, M., Schroeder, I., **Bauer, D.**, Thiel, G., and Hamacher, K. (2021)

[Inferring functional units in ion channel pores via relative entropy](#).

European biophysics journal 50.1, pp. 37–57. DOI: [10 . 1007 / s00249 – 020-01480-7](https://doi.org/10.1007/s00249-020-01480-7).

Saponaro, A. *, **Bauer, D. ***, Giese, M. H. *, Swuec, P. *, Porro, A., Gasparri, F., et al. (2021)

[Gating Movements and Ion Permeation in HCN4 Pacemaker Channels](#). *Molecular Cell* 81.14, 2929–2943.e6. DOI: [10 . 1016 / j . molcel . 2021 . 05 . 033](https://doi.org/10.1016/j.molcel.2021.05.033).

* indicates equal contribution.

CHAPTER 2

Voltage-gated Potassium Channels

The history of ion translocation in nerve cells goes back to 1889, when Nernst published his famous equations that relate the presence of voltage to different concentrations of ions¹. This finding was picked up by Bernstein, who hypothesized that the action potential in nerve and muscle cells is driven by an electrical gradient related to the presence of changing ion concentrations on both sides of the cellular membrane:

”Es ist einleuchtend, dass die negative Schwankung (resp. Actionsströme [!]) bei der Reizung [...] nach der Membrantheorie durch Zunahme der Durchlässigkeit für das zurückgehaltene Ion in Folge einer chemischen Veränderung im Plasma [erklärt werden kann].”

- Julius Bernstein (1902)²

60 years later, Hodgkin and Huxley published their “equivalent circuit” and thus described the action potential as a result of the flow of potassium (K^+) and sodium (Na^+) ions across the cell membrane³. However, they were still unaware of how ions can pass through this highly hydrophobic and unpolar barrier. The idea of gated ion channels got traction in the 70’s and 80’s, when experiments by Armstrong, Parsegian, Neher and Sakman revealed high ion conductance as well as the possibility to block ion currents with small molecules like tetraethylazanium (TEA^+)—experimental findings that are incompatible with the idea of non-proteinaceous pores or active ion transport via carrier proteins⁴. Finally, the cloning of the Shaker channel from *Drosophila* (1987) and ultimately the solving of the first ion channel structure (KcsA, 1998) paved the way for a more detailed understanding of how ion channels work on a molecular level⁵. With the recent advancements in the Cryo-EM technology, the solving of structures for membrane proteins have become more accessible. This has resulted in several new structures of more complex cation channels from a broad range of subfamilies such as GluA2, ERG1, HCN1, $Na_v1.7$, KAT1 and many others⁶.

2.1 CLASSIFICATION AND STRUCTURE

Ion channels can be classified by a variety of different properties like the ion selectivity, gating characteristics, or conductance. In the context of voltage-gated ion channels (VGICs) like HCN channels, a natural classification scheme is based on conductance and gating properties. [Figure 2.1](#) shows an overview over selected VGICs with different selectivity and gating properties. Voltage-gated channels contain an additional voltage sensor domain (VSD). This domain includes conserved

¹ Nernst (1889).

² Bernstein (1902).

³ Hodgkin and Huxley (1952).

⁴ Armstrong (1966); Parsegian (1975); Neher and Sakmann (1976); Trudeau and Zheng (2015).

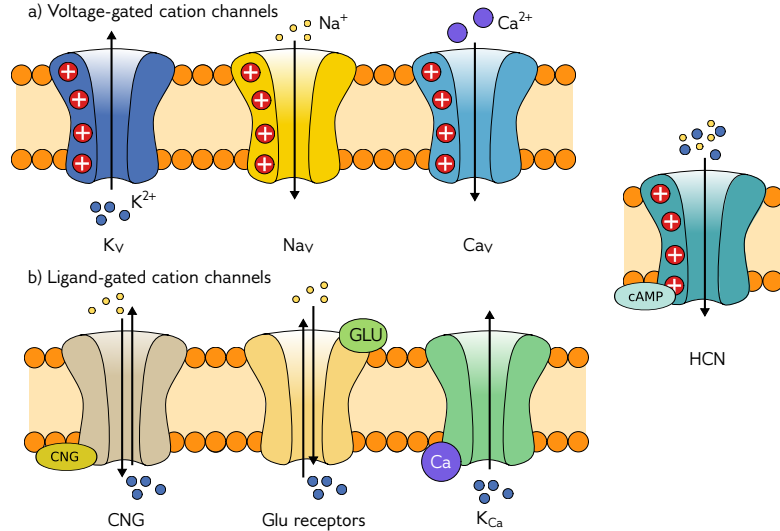
⁵ Papazian et al. (1987); Doyle et al. (1998).

⁶ Twomey et al. (2017); Wang and MacKinnon (2017); Lee and MacKinnon (2017); Shen et al. (2019); S. Li et al. (2020).

positively charged amino acids that "sense" the electric field and alter the channels opening probability depending on the transmembrane voltage (Section 2.2). Ligand-gated ion channels incorporate domains that allow the binding of intra- or extracellular ligands to activate the channel (Section 2.3). More complex channels like HCN exist and depend on several external factors that alter their gating and conductance properties (Chapter 3). Moreover, various channels with more "exotic" gating mechanisms, i.e. pH-sensitivity or light-sensitivity, exist, but won't be covered in detail here⁷.

⁷ Trudeau and Zheng (2015); Kuang, Purhonen, and Hebert (2015).

Figure 2.1: Classification of various cation channels by ion selectivity and gating. a) K_V s, Na_V s, Ca_V s are VGICs mainly transporting K^+ , Na^+ and Ca^{2+} , respectively. b) CNGs are ligand-gated and activate upon binding of cyclic nucleotides. Glutamate receptors (i.e. NMDA and AMPA) open upon binding of extracellular glutamate and K_{Ca} opens upon binding of internal Ca^{2+} . HCN channels are voltage-dependent but also modulated by internal cyclic-adenosine monophosphate (cAMP).



Structurally, potassium channels (K^+ channels) can be classified by the number and arrangement of their domains (Figure 2.2). The vast majority—and HCN channels are no exception to this—are tetrameric proteins that follow the 6TM/P (6 transmembrane domains, one pore) motif. Here, the central pore domain (PD) is composed of four times two transmembrane spanning helices (S5-S6) that incorporate the p-Helix and selectivity filter (SF). The PD is preceded by 4 additional membrane spanning helices (S1-4) which form the VSD. The four VSDs are located at the edges of the central pore unit and can be arranged in two different ways: In domain-swapped channels (i.e. $KvChim$, Figure 2.3a), VSDs are located at the edge of the next subunit and connected to the pore domain via a long alpha-helical linker that acts as a lever and forwards the opening signal from the VSD to the PD. In contrast, non-domain-swapped channels have their VSDs located at the edge of the same subunit (Figure 2.3b). This comes along with a much shorter S4-S5 linker and a different gating mechanism to open the channel pore⁸. HCN channels belong to the latter class⁹.

⁸ Lee and MacKinnon (2017); Tao and MacKinnon (2019).

⁹ Lee and MacKinnon (2017).

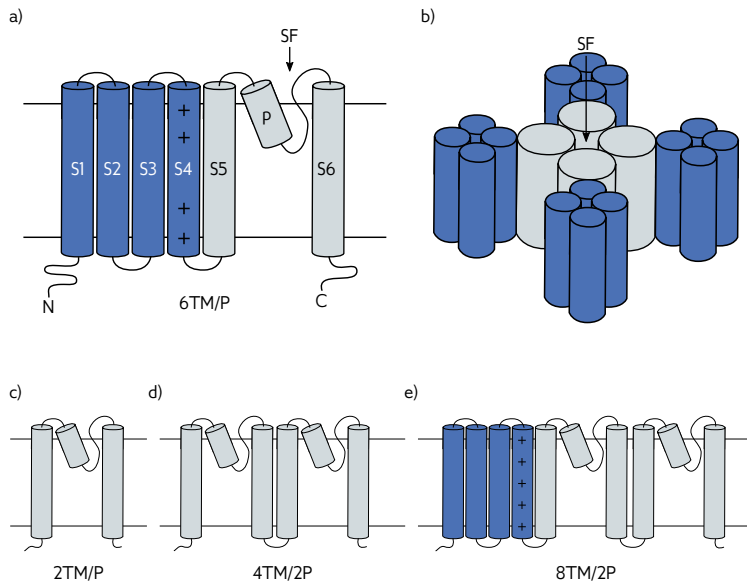


Figure 2.2: Schematic overview and classes of potassium channels. a) The sequence of 6TM/P channels contains one PD and an N-terminally linked VSD per subunit. b) Channels are made of four PDs with the VSDs surrounding the central pore domain. c-e) Several structural variations of this motif exist: c) 2TM/P d) 4TM/2P and e) 6TM/2P. Grey and blue tubes represent transmembrane helices of the PD and VSD, respectively. The plus signs mark S4 as the location of voltage-sensing amino acids.

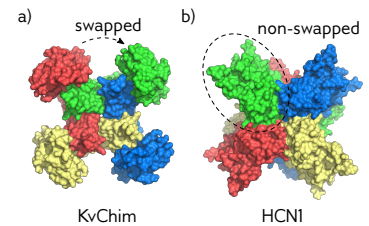


Figure 2.3: Domain-swapped and non-domain-swapped channels: a) The Kv1.2-2.1 paddle chimera (KvChim, PDB: 2R9R), b) HCN1 (PDB: 5U6P).

2TM/P channels (i.e. $KcsA$, K_{IR} , K_{ATP}) consist of only the pore domain and miss a dedicated domain for voltage-sensing*. 4TM/2P and 8TM/2P channels are variations of these motifs where two PDs are linked together in one sequence; they are therefore dimeric channels. Finally, channels where multiple 6TM/2P motifs are chained together exist: Two-pore channels (TPCs) are characterized by two repeats of the 6TM/2P motif; in calcium-selective Ca_{VS} , the same motif is repeated even four times¹⁰. Additional domains are usually found at the cytoplasmic C- and N-terminus (K^+ channels are inserted into the plasma membrane with their termini pointing inside the cell). Common features are a highly conserved tetramerization domain as well as the nucleotide-binding domain (KTN) found in prokaryotic species¹¹. Further domains for ligand binding and regulation usually flank the PD C-terminally for intracellular ligand dependency (i.e. the cyclic-nucleotide binding-domain (CNBD) in HCN channels) or extend the S5-S6 loop for extracellular ligand dependency (K2P). These domains can act as weak regulators having only a small effect on the channels opening probability (HCN channels) or be the only relevant gating mechanism (CNG channels).

2.2 VOLTAGE-DEPENDENCY AND GATING

The cytoplasm of the cell is separated from the outside by the cell membrane—a hydrophobic slab mainly composed of fatty-acid based lipids. This effectively excludes ions from traveling between the extracellular side and the cytosol without the help of specialized proteins. Active transporters—most notably Na^+/K^+ -ATPase—maintain low concentrations of Na^+ inside the cell. This leaves organic anions in

*Nevertheless, several 2TM/P channels have been found to be slightly voltage-dependent: Cordero-Morales, Cuello, and Perozo (2006); Gazzarrini et al. (2009).

¹⁰ Biggin, Roosild, and Choe (2000); Choe (2002).

¹¹ Choe (2002).

¹² Alberts et al. (2017).

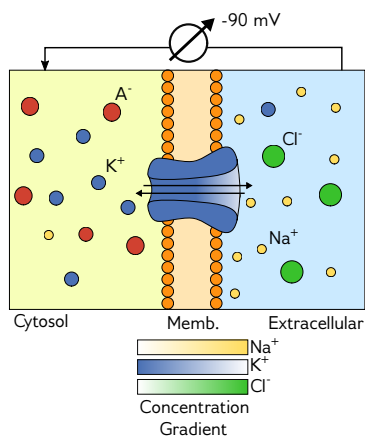


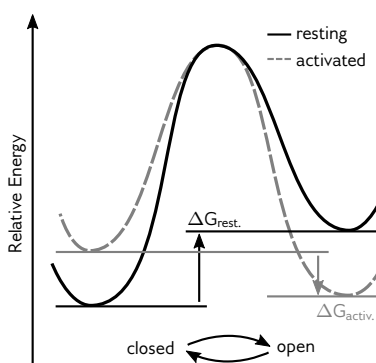
Figure 2.4: Depiction of the membrane potential. The cytosol and extracellular medium are separated by a hydrophobic membrane. A charge imbalance leads to a voltage across the membrane that allows passive cation transport.

the cytosol to be mainly balanced by the presence of higher K^+ concentrations, leading to a K^+ concentration gradient across the membrane (Figure 2.4). Since K^+ is allowed to move freely between the inside and outside of the cell through K^+ leakage channels, an equilibrium arises where the thermodynamic force arising from the K^+ concentration gradient is balanced out by the force arising from an electronic gradient due to charge imbalances across the membrane.

The voltage of this equilibrium depends on the cell type and is of the magnitude of -20 to -120 mV. In nerve cells, this resting potential is at the higher end of the scale, with a potential of approximately -70 (in human).¹²

Broken down to its simplest form, VGICs can exist in two different states: open and closed. The probability of finding a channel in one of these states is directly dependent on the voltage. Thermodynamically, this can be described by a two-state model, where both states correspond to free energy minima in a potential of mean force (PMF). A change in the electric field results in a reweighting of the minima relative to each other, thus making the activated/open state more accessible at corresponding voltages and vice versa (Figure 2.5).

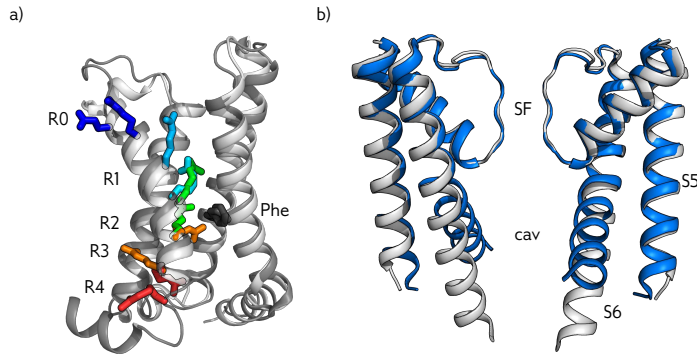
Figure 2.5: Depiction of the free energy profile of voltage-dependent gating in VGICs. Diagram based on Trudeau and Zheng (2015), p. 27.



A VGIC "senses" this voltage by a specialized domain called the VSD, which is made from the first 4 transmembrane helices (TMHs) of each subunit (S1-S4). The four TMHs are arranged to form an hourglass-shaped bundle with water-filled crevices above and below a central phenylalanine (Figure 2.6a). Thus, the drop of the electric field is focused on a very narrow region of the channel. Here, several conserved arginines (R0-R4) are located on the fourth TMH and react to the electric field with their positively charged side chains: when the voltage changes, reorientation of the side chains can trigger a conformational change characterized by an upward- or down movement of the whole TMH corresponding to a gating charge movement of approximately 3 to 4 e^- per subunit¹³. Thereby, the exact value of the gating charge movement depends on the channel species. Furthermore, several models on how the fourth TMH performs this transition exist. The detailed mechanism is still being discussed and also depends on the channel.

¹³ Gandhi and Isacoff (2002).

Ultimately, the activation signal is passed to the PD. Here, the cytosolic entry of the channel is obstructed by an iris-like overlap of the C-



terminal ends of S6. They form a narrow, hydrophobic section along the central axis that does usually not allow passage of water or ions. When VSDs trigger an opening, S5 and S6 swing open, exposing the central cavity to the cytosolic solvent and allowing free passage of ions (Figure 2.6b).

Interestingly, the solved structures of several hyperpolarization-activated VGICs that follow the 6TM/P motif (i.e. HCN₁, HCN₄, KAT₁) revealed that their VSDs have a similar structure to VSDs of depolarization activated channels¹⁴. They feature the same arrangement of four TMHs with arginines in the focused electric field. Nevertheless, activation in this channels must be triggered by a downward movement of the VSDs in contrast to an upward movement in depolarization-activated channels. It is therefore expected that the different gating characteristics in these channels is caused by a different mechanism of how the signal is transferred to the pore domain (see Section 3.4).

2.3 LIGAND-DEPENDENCY

Energetics of ligand-dependent gating are very similar to the ones depicted in Figure 2.5 for voltage-dependency. Binding of a ligand to its corresponding ligand-binding domain (LBD) alters the free-energy landscape of the channel in such a way, that the open state becomes more probable. Further complexities arise since most ligand-dependent channels are multimers and can therefore exhibit some level of cooperativity between subunits. For example, channels that exhibit *opening cooperativity* are more likely to open with binding of more than a single ligand. On the other hand, in channels with *binding cooperativity*, the binding of one ligand directly influences the binding probability of a second ligand to another binding domain, thus making it more (or less) probable to find a given number of ligands bound to the channel. The two cooperativity models are not exclusive and channels can exhibit opening and binding cooperativity together.¹⁵ A good example for cooperativity is the cAMP-dependent HCN₂ channel: consecutive binding of cAMP to all four subunits enhance the channel's opening probability in an additive manner, meaning that each subdomain can contribute to channel opening more or less independently (Figure 2.7).

Figure 2.6: Voltage-dependent gating in ion channels. a) Ci-VSD in its resting (gray, PDB: 4G8o) and activated (white, PDB: 4G8o) state. Colored sticks represent gating-associated voltage-sensing arginines R0-R4 (blue to red). b) MthK in the open (blue, PDB: 3LDC) and closed (white, PDB: 6U5R) state, residues 19-99. For clarity, only two of the four subunits are shown. PDBs from: Q. Li et al. (2014); Ye, Y. Li, and Jiang (2010); Fan et al. (2020).

¹⁴ Lee and MacKinnon (2017); S. Li et al. (2020); Saponaro et al. (2021).

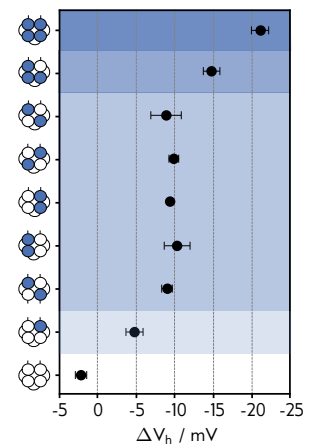


Figure 2.7: Example for ligand cooperativity in a HCN₂ channel construct with concatenated subunits. Filled and empty circles on the y-axis represent subunits with or without bound cAMP, respectively. Adopted from Sunkara et al. (2018).

¹⁵ Trudeau and Zheng (2015).

*Conductance can be close to 1×10^8 ions/s with a selectivity greater 1000:1 $K^+ : Na^+$. See Morais-Cabral, Zhou, and MacKinnon (2001); Doyle et al. (1998).

¹⁶ LeMasurier, Heginbotham, and C. Miller (2001); Armstrong (1966).

¹⁷ Fowler et al. (2013).

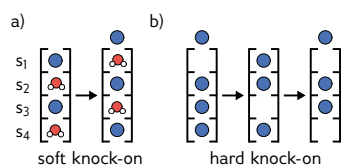


Figure 2.8: Different K^+ conduction models: a) Soft knock-on with water molecules between ions and b) Direct knock-on without co-permeating water.

¹⁸ Morais-Cabral, Zhou, and MacKinnon (2001); Zhou, Morais-Cabral, et al. (2001); Bernèche and Roux (2001).

¹⁹ Köpfer et al. (2014); Kopec et al. (2018); Öster et al. (2019).

²⁰ Simon Bernèche (personal communication, March 2017)

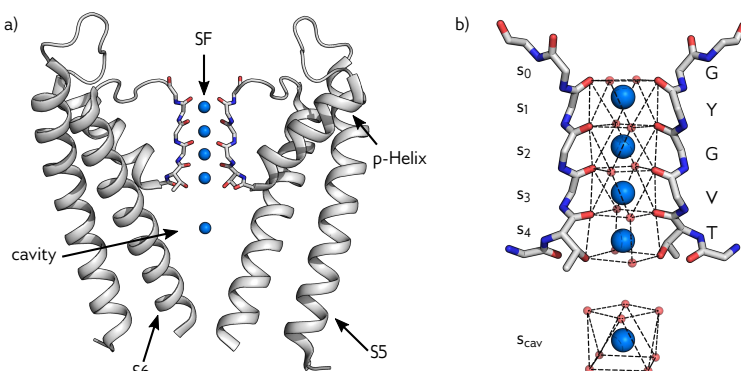
Figure 2.9: Pore domain of KcsA. a) The pore domain as white cartoon with the SF (colored sticks) and possible ion binding sites (blue spheres). For clarity, only two of the four subunits are shown. b) The SF of KcsA forms four binding sites (s_1 - s_4) where K^+ ions are coordinated by eight carbonyl oxygens. s_{cav} (for cavity) is located below the SF. PDB: 1K4C.

2.4 CONDUCTION AND SELECTIVITY

Cation channels in general are highly optimized towards high conductance and selectivity. This is particularly true for K^+ channels that operate at nearly diffusion limit while maintaining high ion-selectivity even between very similar cations*. In general, K^+ selective channels have a selectivity profile of $K^+ \geq Rb^+ > NH_4^+ \gg Na^+, Li^+, Ba^{2+}$ and TEA^+ usually block channels of this type reversibly¹⁶.

When an ion moves through the central pore, it has to pass the SF. In selective K^+ channels, the SF is made of five highly conserved and precisely arranged amino acids: the TxGYG motif (x is usually V or I, Figure 2.9). Here, one loop of each subunit is arranged in such a way that they create four narrow polar oxygen cages (labeled s_0 - s_4 in Figure 2.9b). that act as ion binding sites. Additional binding sites have been identified above (s_0) and below (s_{cav}) the SF motif. When an ion enters the SF, its hydration shell is replaced by interactions with the oxygens pointing towards the central axis. By this, the SF effectively mimics the ions first hydration shell in water, which leads to low energy barriers when the ion moves between consecutive binding sites. This is crucial for maintaining high conduction speed, which is incompatible with energy barriers higher than a few kJ/mol¹⁷.

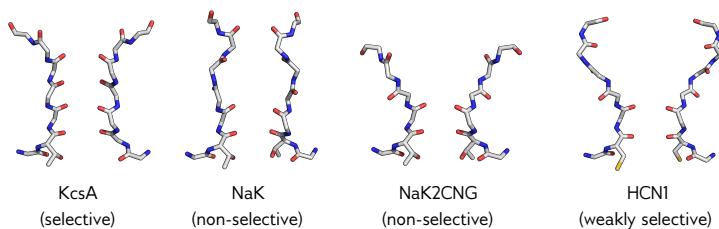
Several mechanisms have been proposed on how the ions move through the SF. In the "soft knock-on" model, the SF is thought to alter between two distinct states with ions bound to either $[s_0, s_2, s_4]$ or $[s_1, s_3]$ while remaining sites are occupied by a single water molecule. Between these states, ions move in concert leading to a water:ion conductance ratio close to 1 (Figure 2.8a)¹⁸. The recently emerged alternative "direct knock-on" model shows ions permeating without any intercalating water. Instead, ions can occupy neighboring binding sites directly (Figure 2.8b). This model has shown promising results for combining high selectivity with experimental conductance in MD simulations while being consistent with experimental data from crystallography, NMR and IR spectra¹⁹. However, the exact mechanism likely depends on the observed channel and channels might even be able to switch between these two mechanisms depending on external conditions like ion concentration and electric field strength²⁰.



While oxygen cages are arranged in a way that they perfectly fit the size of a K^+ , Na^+ is too small to be a good fit for the same binding sites. Instead, Na^+ binds to the planes made by a single group of four oxygens. Upon binding, Na^+ ions are expected to encounter higher energetic barriers for initial binding to the SF as well as moving between binding sites. This leads to high selectivity towards the conduction of K^+ .²¹

It is noteworthy that the SF of potassium channels occupies only a very small portion of the central pore. Below the SF, the channel is filled with water. By this, the region where the conduction rate could be reduced by desolvation and interactions with the protein is focused on a very narrow region of the channel. Inside the central cavity, diffusion along the electrical and concentration gradient can take over again.²²

Recently, the structures of channels with other selectivity characteristics have been resolved (i.e. NaK, CNG, HCN). They share some common features with the canonical SF motif, e.g. the presence of oxygen-cage binding sites, but also show a different number of these sites (Figure 2.10). For example, NaK and a NaK-based chimera construct NaK2CNG-D have only two and three K^+ binding sites, respectively—and they are non-selective. This has led to the hypothesis of four being the “magic number” of sites required for K^+ selectivity. Later, this hypothesis was challenged by the characterization of another NaK chimera with only two consecutive binding sites (NaK2CNG-Dm) that still showed weak selectivity.²³ Clearly, the number of binding sites cannot be the only discriminator for selectivity. Other features like the general backbone flexibility or possible configurational changes that emerge not only from the SF signature sequence alone must play important roles too. This is highlighted by the fact that these channels do not only differ in the number of consecutive binding sites, but also exhibit very different mechanisms on how they conduct ions. For example, NaK is assumed to adopt different configurations for either K^+ or Na^+ conduction²⁴, while HCN channels show now prolonged ion binding to their s_3 site (see Chapter 6)²⁵.



²¹ Noskov, Bernèche, and Roux (2004); Noskov and Roux (2006); Thompson et al. (2009).

²² Yellen (2002).

²³ Derebe et al. (2011); Lam et al. (2015).

²⁴ Shi et al. (2018).

²⁵ Saponaro et al. (2021).

Figure 2.10: The many shapes of ion selectivity. Corresponding PDBs: KcsA: 1K4C, NaK: 3E8G, NaK2CNG: 4ZBM, HCN1: 5U6P. Zhou, Morais-Cabral, et al. (2001); Alam and Jiang (2009); Lam et al. (2015); Lee and MacKinnon (2017).

CHAPTER 3

HCN Channels and Their Role in Cardiovascular and Neurological Diseases

3.1 HCN GENE FAMILY AND PATHOPHYSIOLOGY

The human HCN gene family comprises four members HCN1-4 that share a sequence similarity of 59-67% (Figure 3.1). The core of these channel, which is made by the transmembrane part and CNBD, is highly conserved. In contrast, C- and N-terminal ends differ considerably¹. They are distantly related to other channels of the CNBD superfamily such as hERG1 (identity 18-23%) and the plant K⁺ channel KAT1 (identity 17-18%). HCN expression levels differ widely between different tissue, highlighting the different role of individual subtypes; i.e. HCN3 is expressed mainly in the human cerebellum or during prenatal development while other subtypes can be found in the heart and different regions of the brain. Functionally, HCN subtypes differ mainly in their activation kinetics, voltage-dependency and response to cAMP (Section 3.3).²

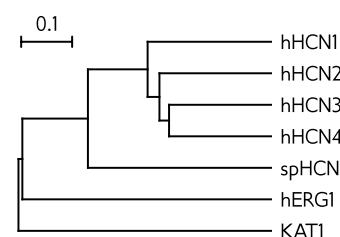


Figure 3.1: Phylogenetic tree of HCN channels and relatives. hHCN1-4, hERG1 from *H. sapiens*, spHCN from *S. purpuratus* and KAT1 from *A. thaliana*.

3.2 BIOLOGICAL ROLE

Several biological processes of the body rely on the generation of a rhythmic and continuous firing of neurons. Examples are not limited to the exactly timed contraction of the cardiac muscle leading to the heart beat and respiration, but also the control of the sleep-wake cycle or memory³. All these processes require the presence of channels that open upon hyperpolarization and rapidly drive the membrane potential back to depolarizing voltages upon previous hyperpolarization.

3.2.1 HCN1 Channels Regulate Neuronal Activity

All isoforms of HCN channels are expressed in the human brain, but with different expression levels depending on the tissue. HCN1 channels are expressed particularly in the cortex.⁴ In general, the current expressed by these channels (I_h for hyperpolarizing current) in brain tissue is involved in a broad range of different processes. One major purpose is the general regulation of the membrane potential of neurons. Because HCN channels are hyperpolarization-activated, they can act as a "feedback mechanism" that counteracts membrane hyperpolarization and thus stabilizes the depolarized state. This in turn also reduces the required resting time between subsequent action potentials because cells can rapidly return to their resting state once an action potential has been dispatched⁵. Furthermore, certain neurons ex-

¹ Biel (2002).

² Santoro and Shah (2020); Ludwig et al. (1998); Moosmang et al. (2001).

³ Ramirez and Richter (1996); McCormick and Bal (1997).

⁴ Monteggia et al. (2000); Moosmang et al. (2001).

⁵ Poolos (2012); Benarroch (2013).

i.e. Chaplan et al. (2003); Strauss et al. (2004); Sun et al. (2005); Marini et al. (2018); Nava et al. (2014); Santoro and Shah (2020).

⁶ Knoll et al. (2016); Arnsten (2011); Santoro and Shah (2020).

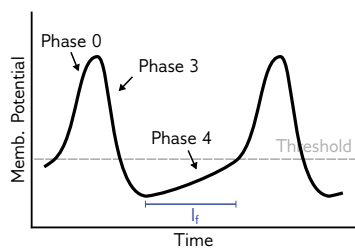


Figure 3.2: Phases of the pacemaker action potential. The blue interval labeled (I_f) corresponds to the time period where HCN channels are primarily open.

⁷ DiFrancesco (1993).

⁸ Biel (2002); Craven and Zagotta (2006).

⁹ Schulze-Bahr et al. (2003); Stieber, Hofmann, and Ludwig (2004); Nof et al. (2007); Laish-Farkash et al. (2010); Jou et al. (2017).

¹⁰ Sulfi and Timmis (2006).

*I.e. EC18, MEL55A, MEL57A. See Romanelli et al. (2019); Dini et al. (2018); Melchiorre et al. (2010); Resta et al. (2018).

press a rhythmic firing comparable to the pacemaker activity in the heart (Section 3.2.2) which also requires the presence of HCN channels. Accordingly, malfunctioning of HCN1 (but also other HCN subtypes) is linked to a broad range of neurological disorders including epilepsy, neuropathic pain, and impaired motor and cognitive development. One prime example for this is the mutation G391D in *hHCN1*, which leads to generalized epileptic encephalopathy in human and is studied in Chapter 5. Furthermore, altering HCN expression levels is discussed as potential target to treat mood disorder, schizophrenia and even learning disorders⁶.

3.2.2 HCN4 Channels Drive Pacemaker Activity

HCN4 is a subtype of HCN channels that is mainly expressed in the sinoatrial node (SAN) of the heart. Here, the rhythmic and continuous heart beat is controlled by specialized pacemaker cells which fire spontaneously—without the requirement of preliminary neuronal activity⁷. The action potential generated by these cells can be divided in three phases (Figure 3.2): the depolarization phase (Phase 0) is characterized by a fast depolarization of the membrane and is primarily caused by the opening of L- and C-type calcium channels (I_{CaT} and I_{CaL} current). In the following repolarization phase (Phase 3), voltage-gated potassium channels (K_v s) open and repolarize the cell membrane (I_K). This influx of K^+ leads to an overshoot of the membrane potential (=hyperpolarization). Subsequently, in Phase 4, HCN4 channels open. Their slow mixed Na^+/K^+ influx (I_f for funny current) then drives the membrane potential back to the threshold required for opening of calcium channels and complete the cycle.⁸ Therefore, without the presence of these specialized hyperpolarization-activated channels, rhythmic pacemaker activity would not be possible. Consequently, mutations of the HCN4 gene have been found in patients suffering from bradycardia and several other forms of SAN dysfunction⁹.

3.2.3 Treatment of HCN-related diseases

One of the key problems in treatment of HCN-related diseases is the absence of potent drugs that can selectively regulate HCN isoforms. While several drugs are known to somehow modulate I_f/I_h , only one of them has been approved as drug that acts specifically on HCN channels: ivabradine, an angina pectoris medication¹⁰. However, ivabradine is not isoform-specific and blocks all HCN subtypes equally by binding inside the hydrophobic cleft of the pore (see Section 6.2.2). Recently, several more specific compounds to target HCN channels have been proposed*. However, they have not been extensively characterized yet and some of them also lack sufficient affinity for medical use in the therapy of neurological diseases.

3.3 FUNCTIONAL CHARACTERIZATION

In contrast to other K^+ channels, HCN channels are only weakly selective and conduct K^+ and Na^+ with a ratio of $P_{K^+}/P_{Na^+} \approx 2$ to $6:1$ ¹¹. Interestingly, the presence of K^+ is required for maintained Na^+ conduction, which has led to the assumption that K^+ somehow takes part in the Na^+ conduction mechanism¹². They do not conduct most divalent ions but show small permeability for Li^+ and Rb^+ . In contrast to other K^+ channels, they are not entirely blocked by Ba^{2+} , but extracellular Cs^+ ¹³. Measured single channel conductance is very low. In fact, HCN channels are among the channels with the smallest conductance rate of all K^+ channels with only approximately 1 to 2 pS (≈ 1 ion every 1.6 μs at -100 mV).

The mechanism underlying low selectivity and conductance in HCN channels was essentially unknown. This was primarily due to the lack of open channel structures that would allow the investigation of ion conduction via MD simulations. However, the recent release of an open structure of HCN4 with accompanied *in-silico* studies revealed that both effects are a result of the unique shape of the SF that comes with altered ion binding and a different conduction mechanism (see Chapter 6)¹⁴.

HCN channels are primarily voltage-gated and open upon hyperpolarization of the membrane. The half-activation voltage $V_{1/2}^*$ is modulated via cAMP, which promotes channel opening at higher voltages ($\Delta V_{1/2} > 0$ mV). This allows regulation via various neurotransmitters, hormones and metabolic stimuli that affect the level of intracellular cAMP¹⁵. They are also weakly sensitive to cyclic-guanosine monophosphate (cGMP) and can be further regulated by a brain-specific auxiliary subunit named TRIP8b¹⁶. Additionally, a regulation of their conductance by the presence of certain ions is known: Na^+ conductance depends on the presence of external K^+ (Chapter 6)¹⁷ and general conductance depends on the presence of Cl^- in HCN2 and HCN4¹⁸. Differences in $V_{1/2}$ between subtypes are hardly comparable because they highly depend on the experimental conditions¹⁹. In general, values between -70 and -100 mV are reported²⁰. Subtypes can easily be distinguished by their activation kinetics though. HCN1 is the fastest subtype while HCN4 is the slowest channel with HCN2-3 lying in between. The magnitude of the response to cAMP is also subtype-dependent and increases with decreasing activation kinetics (HCN1 < HCN2-3 < HCN4). In contrast to many other VGICs, HCN channels show no C-type inactivation. However, especially for the slow subtypes HCN3 and HCN4, the current can be parted in two components: a fast-developing instantaneous current (I_{INS}) and a slowly developing steady-state current (I_{SS}). While I_{INS} can be increased by “priming” channels with consecutive hyperpolarization steps, this is not the case for I_{SS} . This has been interpreted as a portion of the channel population exhibiting incomplete deactivation and, as a result, being not fully closed but in a leaky state.²¹

¹¹ I.e. Ludwig et al. (1998); Santoro, Liu, et al. (1998); Gauss, Seifert, and Kaupp (1998); Moroni et al. (2000).

¹² Gauss, Seifert, and Kaupp (1998); Lyashchenko and Tibbs (2008).

¹³ Biel (2002); Yu, Duan, et al. (2004); Yu, Chen, et al. (2007); Ishii et al. (1999); Ludwig et al. (1998); Gauss, Seifert, and Kaupp (1998).

¹⁴ Saponaro et al. (2021).

*The voltage at which channel exhibit half of the maximal response.

¹⁵ DiFrancesco and Tortora (1991).

¹⁶ Ludwig et al. (1998); Hu et al. (2015); Han et al. (2020).

¹⁷ Lyashchenko and Tibbs (2008).

¹⁸ Wahl-Schott et al. (2005); Mistrík, Pfeifer, and Biel (2006).

¹⁹ Seifert et al. (1999).

²⁰ Biel (2002).

²¹ Altomare et al. (2001); Mistrík, Pfeifer, and Biel (2006).

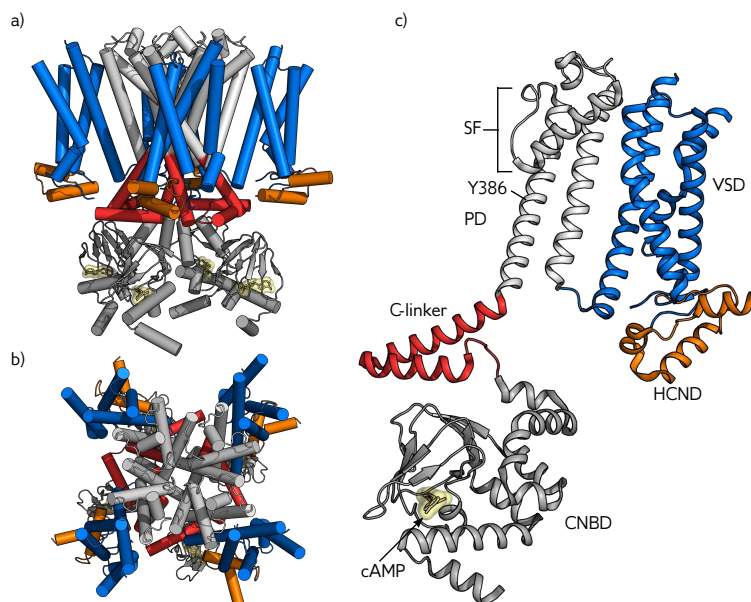
3.4 CHANNEL STRUCTURE

HCN channels are of fourfold symmetry with the canonical 6TM/P architecture of other K_v s (Figure 3.3). VSDs are packed against the PD of the same subunit in a “non-swapped” arrangement. S4, which carries the voltage-sensing arginines is surprisingly long and extends into the cytosol. Cross-linking experiments as well as MD simulations indicated that voltage-activation leads to a downward movement of S4 upon activation. In this process, the helix breaks in the middle and the lower part aligns parallel to the membrane²². The C-terminal end of the PD is followed by the C-linker. Here, a helix-turn-helix motif connects the PD with the CNBD of each subunit. The C-linker is also strongly interconnected with the VSD and N-terminally located HCN domain (HCND). These interconnections are crucial for the forwarding of the signal of cAMP-binding or voltage-change to the central PD (see Chapter 5)²³

²² Kasimova et al. (2019); Lee and MacKinnon (2019); Ramentol, Perez, and Larsson (2021).

²³ Porro et al. (2019).

Figure 3.3: HCN channel structure. a-b) Cartoon representation of HCN1 (PDB: 5u6p) in side and top-down view. c) A single subunit of HCN1. Functional domains are color-encoded in orange (HCND), blue (VSD), white (PD), red (C-linker) and grey (CNBD). The yellow sticks and surface represents bound cAMP.



²⁴ Lee and MacKinnon (2017); Saponaro et al. (2021).

²⁵ Saponaro et al. (2021).

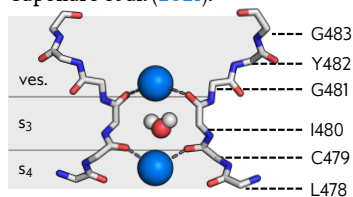


Figure 3.4: 3D structure of the SF backbone of HCN4 (seq: LCIGYG) with two bound K^+ (blue spheres) and a water molecule (red and white spheres). For clarity, only two of the four subunits are shown.

So far, only the structures of HCN1 and HCN4 have been solved²⁴. The biggest differences between the two subtypes can be found in the connections between the C-linker/HCND and other parts of the channel, which leads to their profound difference in cAMP dependence. For example, a Mg^{2+} -binding tetrad formed by residues of the C- and S4-S5 linker is crucial for cAMP-dependence in HCN4. By disrupting it, cAMP-dependence can be reduced to a level similar to HCN1, which does not feature this tetrad naturally and shows only limited effects upon binding of cAMP²⁵.

Even though the SF of HCN channels contains the GYG signature sequence which is common to K^+ channels, it adopts a vastly different conformation (Figure 3.4). Instead of the 4(+1) binding sites (s_0 - s_4) found in K^+ -selective channels, the filter adopts a conformation where

it exhibits only two such sites. Carbonyl oxygens that would normally form s_1 to s_2 are rotated away from the central axis, which gives rise to a large water-filled vestibule (ves.) above the SF. Additionally, because the first T of the TxGYG motif is replaced by C (C479 in HCN4) in HCN (seq: LCIGYG), s_4 is significantly wider in these channels. The side chains of C cannot contribute to ion binding at all, which presumably reduces ion selectivity of this site. This leaves the SF of HCN with only a single canonical K^+ -selective binding site (s_3). With these features, the HCN SF more closely resembles the SF of the non-selective NaK channel or NaK2CNG (compare to [Figure 2.10](#)). NaK also features a vestibule above two potassium binding sites. However, in NaK, we can find an additional ion binding site upstream of the vestibule and s_4 is maintained as selective K^+ binding site with similar shape found in K^+ channels²⁶. Interestingly, even though NaK has one additional selective site, it is basically non-selective for K^+ . The reason for this is presumed to be the ability of NaK ability to adopt different conformations that facilitate either K^+ or Na^+ conduction²⁷. All these differences lead to a vastly different ion conduction mechanism in HCN channels compared to both unselective and selective K^+ channels. In HCN channels, the SF alternates between two distinct states with either one or two ions bound that are separated by high energy barriers, thus reducing conductance ([Chapter 6](#))²⁸.

Below the SF, one can find a water-filled, hydrophobic cavity that can hold an additional (solvated) ion. The end of this cavity is marked by a Y (Y386 in HCN1) residue that can rotate inside the pore ([Figure 3.3](#)).

²⁶ Alam and Jiang (2009).

²⁷ Shi et al. (2018).

²⁸ Saponaro et al. (2021).

CHAPTER 4

Theory and Methods

4.1 MOLECULAR DYNAMICS SIMULATIONS

MD—the science of simulating the motions of a system of particles—applied to biological macromolecules gives the fluctuations in the relative positions of the atoms in a protein as a function of time.

- Karplus and Petsko (1990).

In more simple terms: if we consider a virtual box full of interacting balls (which we imagine to be representing atoms), we can use MD simulations to obtain the motion of these particles. Therefore, the algorithm underlying molecular dynamics is a subsequent iteration of the equations of motion for each particle, resulting in the time-dependent position and velocities for all particles of the system (Figure 4.1). This allows us to study biological systems *in-silico* on an atomistic scale.

In classical MD simulations, the dynamics of a system of particles is approximated using classical mechanics. The Hamiltonian $\mathcal{H}(t, \mathbf{x}, \mathbf{p})$ of a time-dependent system of N particles with spatial coordinates $\mathbf{x} = \{x_1(t), x_2(t), \dots, x_N(t)\}$ and momenta $\mathbf{p} = \{p_1(t), p_2(t), \dots, p_N(t)\}$ is given by

$$\mathcal{H}(t, \mathbf{x}, \mathbf{p}) = U(t, \mathbf{x}) + K(t, \mathbf{p}) = U(t, \mathbf{x}) + \sum_i \frac{p_i(t)^2}{2m_i} \quad (4.1)$$

where $U(t, \mathbf{x})$ is the potential energy function, $K(t, \mathbf{p})$ is the total kinetic energy and all other symbols have their usual meaning. The motion of each particle i can then be described by Hamilton's equations¹:

$$\begin{aligned} -\frac{\partial \mathcal{H}}{\partial x_i} &= -\frac{\partial U}{\partial x_i} = \dot{p}_i = m_i a_i = F_i \\ \frac{\partial \mathcal{H}}{\partial p_i} &= \dot{x}_i = v_i \end{aligned} \quad (4.2)$$

In a multi-particle system where all particles interact with each other, the force F_i at time t naturally depends on the positions of all other particles $F_i = F_i(\mathbf{x})$ and a solution for Equation 4.2 can only be obtained numerically². In MD, the most commonly used numerical integrators to obtain such a solution are variants of the Verlet algorithm—such as the Leap-frog integrator³:

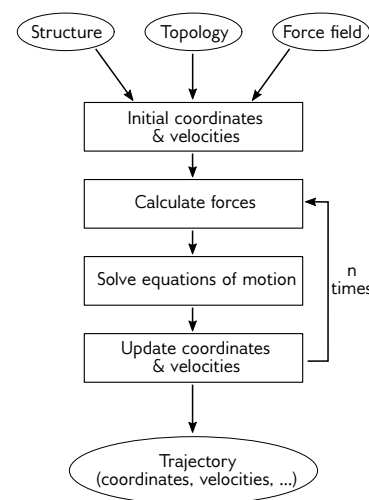


Figure 4.1: High-level overview of the MD workflow.

¹ Tuckerman and Martyna (2000); Hand and Finch (1998).

² Tuckerman and Martyna (2000).

³ Prasad et al. (2018); Hockney, Goel, and J. W. Eastwood (1974); Lindahl et al. (2020).

$$\begin{aligned}
x_i(t + \Delta t) &= x_i(t) + \Delta t v_i(t + \frac{1}{2} \Delta t) \\
v_i(t + \frac{1}{2} \Delta t) &= v_i(t - \frac{1}{2} \Delta t) + \frac{\Delta t}{m_i} F_i(t, \mathbf{x})
\end{aligned}
\tag{4.3}$$

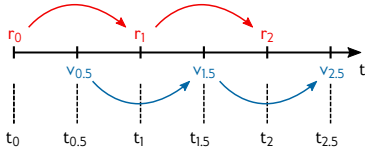


Figure 4.2: Leap-frog integration. Positions and velocities leap ahead of each other by $\frac{\Delta t}{2}$.

Using Leap-frog integration, positions at time t and velocities at time $t + \frac{\Delta t}{2}$ are used to update positions while velocities are updated from velocities at $t - \frac{\Delta t}{2}$. Therefore, velocities "leap" ahead of the position calculation like frogs jumping over each other, leading to the algorithms unusual name (Figure 4.2). In order to obtain velocities at time t (i.e. for saving the trajectories state), a simple time average over velocities at $t \pm \frac{\Delta t}{2}$ can be used.

4.1.1 Force Calculation

Following Equation 4.3, the force $F_i = -\partial U / \partial x_i$ acting on each particle has to be evaluated every time step. For the most common type of force fields, the additive ones, the potential energy function is a sum over all bonded and non-bonded interactions⁴:

⁴ Monticelli and Tieleman (2013).

$$U(t, \mathbf{x}) = U_B(t, \mathbf{x}) + U_{NB}(t, \mathbf{x}) \tag{4.4}$$

where $U_B(t, \mathbf{x})$ and $U_{NB}(t, \mathbf{x})$ are the potential energies of bonded and non-bonded interactions of a given particle, respectively. For the bonded term, 2-, 3- and 4-body interactions of covalently bound atoms are usually considered (Figure 4.3):

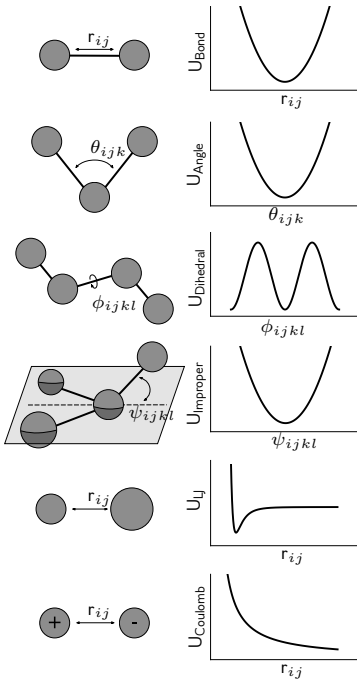


Figure 4.3: Illustration of different interaction types (left) with corresponding potential energy functions (right). From top to bottom: harmonic bond, harmonic angle, proper dihedral angle (torsion), improper dihedral angle (out-of-plane motion), Lennard-Jones potential, Coulomb potential.

$$\begin{aligned}
U_B(t, \mathbf{x}) &= U_{\text{bonds}}(t, \mathbf{x}) + U_{\text{angles}}(t, \mathbf{x}) + U_{\text{dihed.}}(t, \mathbf{x}) + U_{\text{impr.}}(t, \mathbf{x}) \\
&= \sum_{\text{bonds}} k_b (r - r_0)^2 + \sum_{\text{angles}} k_a (\theta - \theta_0)^2 \\
&\quad + \sum_{\text{dihed.}} k_d [1 - \cos(n\Phi + \delta)] \\
&\quad + \sum_{\text{impr.}} k_i (\psi - \psi_0)^2
\end{aligned}
\tag{4.5}$$

An intramolecular bond is usually represented by a harmonic potential (U_{bonds}) with equilibrium distance r_0 and bond stiffness k_b . In a similar manner, the angle between three particles can be represented with a harmonic potential (U_{angle}) too. Torsional potentials are of periodic nature and can therefore be described with a cosine function ($U_{\text{dihed.}}$) where n is the number of minima, Φ is the torsional angle, δ is the phase and k_d another particle-dependent constant. Improper angles describe the out-of-plane motion of particles and impose planarity of certain groups such as sp^2 hybridized carbons—they can also be described by a harmonic potential ($U_{\text{impr.}}$). Here, ψ describes the angle between a bond between two particles and a plane made of three other particles.

In contrast to bonded interactions, non-bonded interactions are not limited to a set of particles and must be calculated between all possible pairs of the system excluding those involved in bonded interactions:

$$\begin{aligned}
 U_{\text{NB}}(t, x) &= U_{\text{LJ}}(t, \mathbf{x}) + U_{\text{C}}(t, \mathbf{x}) \\
 &= \sum_i \sum_{j \neq i} 4\epsilon_{ij} \left[\left(\frac{\sigma_{ij}}{r_{ij}} \right)^{12} - \left(\frac{\sigma_{ij}}{r_{ij}} \right)^6 \right] + \sum_i \sum_{j \neq i} \frac{q_i q_j}{\epsilon r_{ij}^2} \quad (4.6)
 \end{aligned}$$

The Lennard-Jones (LJ) potential represents general Van-der-Waals interactions between neutral atoms. It consists of a repulsive and an attractive term to simulate the effects of close-ranged electron cloud repulsion and long-ranged electrostatic attraction between (implicitly) induced and permanent dipoles, respectively⁵. Most classical force fields parametrize the LJ potential based on particle type. Each particle is described by a set of empirical parameters σ_i and ϵ_i . The LJ term between particles of different species is then evaluated by combining atomic parameters according to some sort of combination rule to obtain σ_{ij} and ϵ_{ij} ^{*}. For charged atoms, an additional Coulomb (C) potential is employed. It depends on the charge q_i and q_j of both particles, their distance r_{ij} as well as the (location-dependent) permittivity ϵ . Both pairwise potentials are expensive to calculate if all particles of a system are considered ($\mathcal{O}(N^2)$). Therefore, several simplifications and tricks are applied to speed up calculations of non-bonded energy terms⁶: for the LJ potential, we can see that its long-ranged contribution decays with r^{-6} while the number of pairwise potentials only grows with r^2 (the surface area of a sphere). The contributions of particles therefore quickly become negligible with distance and a smooth cut-off (usually around 1 nm) together with pair-/neighbor-lists can be employed to save computation time. In contrast, the Coulomb potential only decays with r^{-1} , making a plain cut-off unfeasible. A computationally cheap ($\mathcal{O}(N \log N)$) alternative approach for periodic systems employs particle-mesh Ewald (PME) summation to calculate the long-range contributions of electrostatics and add them to the traditionally calculated short-ranged contribution⁷.

4.1.2 Temperature and Pressure Coupling

Without defining temperature and pressure, the simulated system runs at constant particle count, volume and energy E —the micro-canonical ensemble (NVE). However, experimental data is usually obtained from an isothermal-isobaric ensemble (NpT), where pressure and temperature are constant, but the energy and volume of the system are allowed to change. The temperature of such a system is defined via the average kinetic energy of particles $\langle K \rangle$ and can be deduced from the equipartition theorem. It states that every degree of freedom of a particle contributes equally to its kinetic energy with $\frac{1}{2}k_B T$. Therefore, the temperature T can be defined as⁸:

⁵ J. E. Jones (1924); Cramer (2004).

^{*}Common combination rules are: $\epsilon_{i,j} = \sqrt{\epsilon_i \epsilon_j}$ and $\sigma_{i,j} = \frac{1}{2}(\sigma_i + \sigma_j)$.

⁶ Monticelli and Tieleman (2013).

⁷ Essmann et al. (1995).

⁸ Lindahl et al. (2020).

$$\begin{aligned}\langle K \rangle &= \frac{3}{2}k_B T = \langle \frac{\mathbf{p}^2}{2\mathbf{m}} \rangle = \frac{1}{N} \sum_i \frac{p_i^2}{2m_i} \\ \Leftrightarrow T &= \frac{1}{3Nk_B} \sum_i \frac{p_i^2}{m_i}\end{aligned}\tag{4.7}$$

⁹ M. P. Eastwood et al. (2010).

Here, \mathbf{m} is the diagonal mass matrix⁹. Therefore, to control a systems temperature, we can adjust particles velocities in such a way that the average kinetic energy matches our target temperature. A simple method to do so is applied by the velocity-rescaling thermostat, which imposes a uniform rescaling factor $\alpha = \sqrt{K(t)/K_{\text{target}}}$ to all velocities. However, since this approach suppresses the natural fluctuations of the kinetic energy, it does not allow proper canonical sampling. This can be overcome by an additional stochastic term which ensures correct energy distributions, leading to the the Bussi-Donadio-Parrinello thermostat¹⁰.

¹⁰ Bussi, Donadio, and Parrinello(2007).

Assuming ideal gas statistical mechanics, the pressure of a system can be defined via the virial theorem¹¹:

¹¹ Clausius (1870); de Miguel and Jackson (2006).

$$\begin{aligned}W &= -3PV + \sum_i \sum_{j<i} F_{ij}r_{ij} = -3Nk_B T \\ \Leftrightarrow P &= \frac{1}{3V} [3Nk_B T + \sum_i \sum_{j<i} F_{ij}r_{ij}]\end{aligned}\tag{4.8}$$

where the virial W corresponds to the expectation value of the sum of the products of particle distances r_{ij} and forces acting between the particles F_{ij} . The theorem states that $W = -3Nk_B T$ and allows to express the instantaneous pressure of the system by quantities that are computed by the MD algorithm anyways.

The instantaneous pressure of a simulation system usually fluctuates significantly on small time scales since pressure is a macroscopic property. Therefore, the rolling average of the pressure over several ns is the actual quantity to consider. To scale the pressure of a system, the particles coordinates \mathbf{x} are adjusted alongside the volume of the unit cell¹².

¹² Lindahl et al. (2020).

4.1.3 Simulating Ion Channels

Simulation of membrane proteins is challenging, both for force field developers and their users. Ion channels are naturally embedded in a lipid bilayer which forms the surrounding of the cell. Therefore, simulation systems are heterogeneous in nature and force fields must accurately describe the interactions between protein-solvent, solvent-lipid and lipid-solvent¹³. The most commonly used force fields for ion channel MD simulations are the CHARMM and AMBER force fields. Both exist in various different versions and have been put into use for the simulation of proteins, lipids, DNA/RNA and a large variety of different biomolecules¹⁴.

¹³ Maffeo et al. (2012).

¹⁴ I.e. Klauda et al. (2010); Vanommeslaeghe et al. (2010); Huang and MacKerell (2013); Hart et al. (2012); Högerberg, Nikitin, and Lyubartsev (2008); Lindorff-Larsen et al. (2010); Cordomi, Caltabiano, and Pardo (2012).

While aqueous systems equilibrate rather quickly, the same does not hold for systems including a membrane. The main reason for this can be found in the long lipid tails, which equilibrate only slowly¹⁵. Therefore, it is usually unfeasible to assemble a solvated protein-membrane system such as the one shown in [Figure 4.4](#) from scratch—it's equilibration would take hundreds, if not thousands, of nanoseconds to complete. Therefore, several alternative methods that help with the preparation of an initial system have been developed. They yield sufficiently equilibrated membranes that only require limited time for equilibration prior to the production MD simulation: one strategy is the initial equilibration using a coarse-grained representation of the molecules, i.e. from the MARTINI force field¹⁶. After the lipids assembled around the protein and are sufficiently equilibrated, the system can then be translated to an atomistic representation ("backmapping")¹⁷. Alternative approaches rely on the assembly of a quasi-equilibrated membrane from lipids selected from a rotamer library. A prominent example for this method is the web-based "CHAMM GUI membrane builder"¹⁸. Both methods have been used successfully during the research work presented here ([Chapter 5](#) and [Chapter 6](#), respectively).

In nature, an imbalance in ion distribution across the membrane is the source of an electric field that drives ion transport ([Section 2.2](#)). Explicit modeling of a similar charge imbalance in MD simulations is difficult: MD simulations usually employ periodic boundary conditions (PBC) and therefore the two sides of a membrane actually belong to the same continuous solvent volume. One approach is to prepare a double-bilayer system that contains two membranes to separate the aqueous slab into two compartments with different ion concentrations. However, the transport of a single ion in these systems can already lead to a drastic change in the electric field due to their small volume¹⁹. Therefore, algorithms to keep the charge imbalance at a constant level have to be applied, i.e. by exchanging ions and water molecules between the compartments (this is coined computational electrophysiology)²⁰. An alternative approach that does not require an increase in system size is the application of a fully artificial electric field that mimics the presence of two aqueous salt bath solutions above and below the system. This method allows to fine tune the applied voltage more precisely and to apply oscillating electric fields²¹. Both methods have been used extensively for the study of ion channels²². For this thesis, the latter method was chosen because of its ease of use and comparability to voltage patch clamp experiments (see [Chapter 6](#)).

4.1.4 Enhanced Sampling & Free Energy Calculations

Enhanced sampling techniques and free energy calculations are common strategies to investigate the dynamics underlying systems where the phase space* can hardly be sampled via classical MD simulations alone (i.e. because of high energy barriers between states of interest). The potential of mean force (PMF) of a system shows the free energy

¹⁵ Maffeo et al. (2012).

¹⁶ Marrink et al. (2007); Monticelli, Kandam, et al. (2008); de Jong et al. (2013); Souza et al. (2021).

¹⁷ Wassenaar et al. (2014).

¹⁸ Wu et al. (2014); Jo et al. (2008).

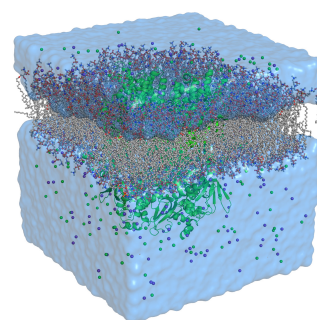


Figure 4.4: Snapshot of an equilibrated protein-membrane simulation. The protein (green) is embedded into a lipid bilayer (colored balls and sticks). The whole lipid slab is solvated with an aqueous KCl solution (blue area with purple and green spheres as ions).

¹⁹ Roux (2008).

²⁰ Kutzner, Grubmüller, et al. (2011).

²¹ Roux (2008); Gumbart et al. (2012).

²² I.e. Jensen, Borhani, et al. (2010); Jensen, Jogini, et al. (2012); Köpfer et al. (2014); Kutzner, Köpfer, et al. (2016); Kopec et al. (2018); Shi et al. (2018); Bernsteiner et al. (2019).

*A set containing all possible states the system may occupy.

surface along a set of chosen variables and allows to study free energy pathways. In the context of ion channels, sampling of a multidimensional PMF is often used to reveal the energy barriers and differences associated with the conduction of ions through the PD of the channel²³.

²³ I.e. Bernèche and Roux (2001); Egwolf and Roux (2010); Fowler et al. (2013); Wojtas-Niziurski et al. (2013); Medovoy, Perozo, and Roux (2016).

There are several methods to obtain the PMFs related to a set of chosen collective variables (CVs) in MD. The most simplest do not require any additional sampling strategies and rely on a Boltzmann inversion of the sampled and binned probabilities:

$$\begin{aligned} P(\lambda) &\propto e^{-\beta A(\lambda)} \\ \Leftrightarrow A(\lambda) &\propto -\frac{1}{\beta} \ln[P(\lambda)] \end{aligned} \quad (4.9)$$

where λ is a possible configuration of the system, $P(\lambda)$ is the probability of finding the system in this state, $A(\lambda)$ is the corresponding Helmholtz free energy and $\beta = (1/k_B T)$. Here, the energy of the most probable state has been chosen as zero point because only the relative difference between free energies has a physical meaning.

For biologically relevant systems, applying Equation 4.9 to the probabilities obtained from an unbiased simulation is unfeasible. The presence of potential energy barriers makes it impossible—or at least very unlikely—to sufficiently sample the whole phase space in finite time. Therefore, enhanced sampling techniques such as metadynamics, the adaptive biasing method or umbrella sampling (US) are used to obtain the PMF of a system with reduced computational effort²⁴.

²⁴ Laio and Parrinello (2002); Darve and Pohorille (2001); Souaille and Roux (2001); Wojtas-Niziurski et al. (2013).

In US, several short and independent simulations are run. In each of them, the system is forced to sample a specific region of phase space by applying a restraint in the form of a potential bias to the system (Figure 4.5). Therefore, the Hamiltonian of the system changes from Equation 4.1 to

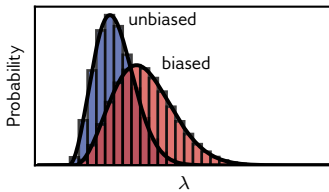


Figure 4.5: Example of a biasing potential: The potential energy function of the system is altered to sample a different region of phase space (red) compared to the unbiased distribution (blue).

$$\mathcal{H}(\mathbf{x}, \mathbf{p}) = U(\mathbf{x}) + U'(\mathbf{x}) + K(\mathbf{p}) \quad (4.10)$$

where $U'(\mathbf{x}) = U'(\lambda)$ is the added biasing potential that depends only on the chosen CVs. Here, the time dependency t has been omitted for simplicity. The free energy $A(\lambda)$ of the system in state λ is then given by

$$A(\lambda) = -\beta \ln[P'(\lambda)] - U'(\lambda) + f \quad (4.11)$$

where $P'(\lambda)$ is the biased probability and f is the free energy change that comes from the addition of $U'(\lambda)$ to the original potential energy function.

The Weighted Histogram Analysis Method (WHAM) can then be used to obtain the “true” unbiased probabilities. For that, a histogram over the sampled phase space is created. Usually, one chooses a smaller bin size than the distance between neighboring US simulations for this; nonetheless sufficient overlap of the probability distributions has to be guaranteed. Unbiased probabilities are then given by the WHAM equations²⁵:

$$P(\lambda) = \frac{\sum_i^N n_i(\lambda)}{\sum_i^N g_i e^{\beta[f_i - U'_i(\lambda)]}} \quad (4.12a)$$

$$f_i = -\frac{1}{\beta} \ln\left(\sum_j^{\lambda} P(j) e^{-\beta U'_i(j)}\right) \quad (4.12b)$$

Here, N is the number of independent simulations, $n_i(\lambda)$ is the number of times the simulation i visited bin λ and $g_i = 1$ is a weight. Starting from an initial guess for f_i , Equation 4.12a and Equation 4.12b can be solved until self-consistency to obtain $P(\lambda)$ and subsequently the PMF via Boltzmann inversion (Equation 4.9).

Since the strength and form of $U'(\lambda)$ can be chosen at will, US+WHAM allow to sample the phase space much more efficient than classical MD simulations. The only requirements that must be met is that the system is still stable under the biasing potential $U'(\lambda)$ and that $P'(\lambda)$ obtained from individual simulations overlap significantly (otherwise, no continuous energy function can be extracted via WHAM).²⁶

4.1.5 Limitations

Even though MD simulations are broadly applied in the field of biophysics and computational chemistry, it is also important to be aware of its limitations in both accuracy and application. After all, molecular mechanics is only an approximation of reality—a rough one. Atoms are considered as classical particles without explicit electrons (Born Oppenheimer approximation). This makes particles in MD insensitive to polarization- and quantum effects. As a result, processes that involve polarization, electron transfer, tunneling or chemical reactions can only hardly be modeled in classical MD*. Also, since all force fields are parametrized more or less empirically, their application is usually limited to a small range of conditions under which they can reproduce a small set of observables of a system²⁷. Therefore, care must be taken when choosing an appropriate force field for a specific use case. Finally, simulation algorithms are prone to numerical errors that lead to an exponential divergence for systems with initially very similar starting configurations. Their accuracy in sampling the time evolution of many-body systems has yet to be proven. Frenkel and Smit therefore conclude (with a wink):

²⁵ Kumar et al. (1992); Grossfield (2003).

²⁶ Kästner (2011).

*Some of these limitations can be overcome by the use of non-classical force fields. Examples are the Drude force field (polarizable), ReaxFF (chemical reactions) or X-POL (QM/MM). See Jing et al. (2019); van Duin et al. (2001); Lemkul et al. (2016); Xie et al. (2009).

²⁷ González (2011); Monticelli and Tieleman (2013); Martín-García et al. (2015).

Hence, our trust in Molecular Dynamics simulation as a tool to study the time evolution of many-body systems is based largely on belief. To conclude this discussion, let us say that there is clearly still a corpse in the closet. We believe this corpse will not haunt us, and we quickly close the closet.

- Frenkel and Smit (1996).

Finally, MD simulations are limited both in time and size (=number of particles) of the system—usually several μ s and significantly less than 10^6 atoms. This leaves many interesting processes such as allosteric transitions, protein folding or ligand-binding out-of-scope for this method²⁸. They happen on entirely different timescales and cannot be achieved even on the largest computing clusters.

²⁸ Fenwick, Esteban-Martín, and Salvatella (2011).

4.2 MOLECULAR DOCKING

Despite the rapid increase of computational power in recent years, finding the correct orientation of a ligand bound to a receptor is still challenging. This is mainly due to the combinatorial explosion associated with the many degrees of freedom of such a system where the receptor and ligand are comprised of dozens or hundreds of atoms²⁹. Therefore, using MD simulations without detailed knowledge of the underlying phase space and a good starting conformation is usually not feasible. Common molecular docking algorithms try to overcome this problem mainly by two important distinctions from MD:

²⁹ Leach (2001).

- Rigid body docking: By treating some or all parts of the molecule as a rigid body, the number of degrees of freedom can be drastically reduced. Most often, this is employed for the receptor only while the ligand is still allowed to explore various different conformations. The “rigid body approximation” has shown itself to still be accurate in many cases where only limited induced fit is expected³⁰.
- Better sampling: MD schemes need to follow a strict physical path to sample the phase space. In contrast, other algorithms like Monte-Carlo sampling, Gaussian shape fitting or genetic algorithms are more suitable for the molecular docking problem³¹. They can generate large sets of different possible structures without the requirement of sampling the physical path connecting them³².

³⁰ Pagadala, Syed, and Tuszynski (2017); E. B. Miller et al. (2021).

³¹ Leach (2001); Morris, Goodsell, et al. (1998); Chaudhary and Mishra (2016).

³² Leach (2001).

³³ Morris, Goodsell, et al. (1998); Morris, Huey, et al. (2009).

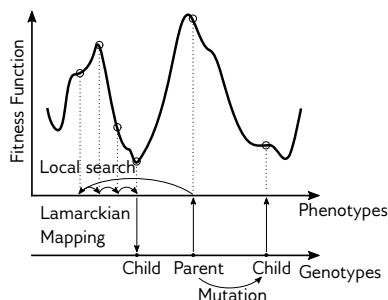


Figure 4.6: Illustration of the Lamarckian genetic algorithm involving inheritance, mutation and a local search. Adapted from Morris, Goodsell, et al. (1998).

AutoDock 4.2, which was used in the present thesis, uses a Lamarckian genetic algorithm as its primary method³³. Here, a set of initial conformations is created and improved successively in further generations. Thereby, “individuals” compete against each other and their performance is measured based on the empirical potential energy function. In each generation, the best performing candidates are allowed to “reproduce” and create the next generation. Parameters of “childs” are thereby inherited from “parents” and random perturbations (“mutations”) can occur analogous to evolution. Finally, best performers are also allowed to sample their surrounding phase space via an iterative local search algorithm (Figure 4.6).

4.3 TRANSITION STATE THEORY

Transition state theory (TST) is a classical approach that has been developed simultaneously by Eyring, Evans and Polanyi to explain experimental reaction rates by the underlying free energy surface³⁴. For a system with only two energy minima A and B (Figure 4.7), TST states that the reaction rate k is a function of the underlying potential of mean force:

$$k = v e^{-\beta \Delta A^\ddagger} \quad (4.13)$$

where ΔA^\ddagger is the free energy difference between the ground state A and transition state and $v = \kappa(k_B T)/h$ is the preexponential “frequency” factor. The transmission coefficient $\kappa \in [0; 1]$ allows for the possibility that a system at the transition state does not lead to a successful transition³⁵. All other symbols have their usual meanings. TST can therefore be seen as an improvement of the previously used Arrhenius equation where the preexponential factor was of empirical nature.

In general, several assumptions underlay TST that limit its application and accuracy. Since TST is derived from equilibrium statistical thermodynamics, it is assumed that the population of all states follows a Boltzmann distribution. However, this is only true if states are long-lived. Furthermore, systems are thought to behave in a classical manner (no tunneling or other quantum effects) and the transition state is postulated as a point-of-no-return, meaning that a system cannot “go back” once the saddle point of the free energy profile has been crossed³⁶. Also, the application of TST to systems with multiple states or competing pathways is limited. While solutions for these systems can be found (i.e. by chaining reaction rates together and solving the underlying set of differential equations), it is often more suitable to define the step with the highest free energy barrier as rate-limiting step. With these approximations, TST can be used to give an upper estimate for the expected height of free energy barriers³⁷.

Originally, TST has been intended to describe reaction rates of chemical reactions. Nevertheless, it has since then been applied to various other processes with known rate constants or potential energy surfaces such as K^+ channel conductance and VSD activation³⁸.

³⁴ Eyring (1935); Evans and Polanyi (1935); Salamon et al. (2015).

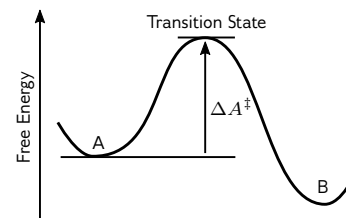


Figure 4.7: In transition state theory, the rate constant for the transition between state A and B depends on the energy difference between the ground state A and the transition state ΔG^\ddagger .

³⁵ Laidler and King (1983).

³⁶ Hänggi, Talkner, and Borkovec (1990).

³⁷ V. B. Luzhkov and Åqvist (2001).

³⁸ V. B. Luzhkov and Åqvist (2001); Delemotte et al. (2015).

Part II

Results

CHAPTER 5

Modeling Mutations in HCN channels

5.1 INTRODUCTION

The first ion channel-related disorder was found in 1989, when Rioridan et al. proposed a mutation of an at this time unknown chloride transporter—the cystic fibrosis transmembrane conductance regulator (CFTR) protein—to be the origin of cystic fibrosis (CF)¹. Since then, the number of mutations in ion channels linked to diseases is ever growing. For CFTR alone, there are now more than 1600 known mutations causing various degrees of this disease². Added to this are a vast number of very different disorders directly or indirectly linked to malfunctioning of ion channels or related proteins. These disease-causing mutations, which have been compromised under the term “channelopathies”, can affect a broad range of different biological systems³.

Functional assays in *in-vitro* and *in-vivo* mutation studies are common techniques used to investigate such channelopathies⁴. They allow to characterize the impact of (single) amino acid exchanges and elucidate their role in functional disorders. However, the absence of corresponding mutated 3D structures often makes it challenging to correctly interpret these experimental results in a molecular context. And even if such a structure is available, it usually does not reveal the full picture: allosteric transitions or dynamic features such as protein flexibility can hardly be deduced from structural information alone. Therefore, a combination of homology modeling and comparative MD simulations are natural partners that can enhance the knowledge of wetlab experiments and give another perspective to further the understanding on the genotype-phenotype relationship of proteins of interest.

HCN channels are another prominent class of ion channels linked to various channelopathies. Functionally, HCN channels differ from other K_V s in several ways: they are not activated by depolarization but by hyperpolarization and they discriminate only poorly between K^+ and Na^+ . In addition to voltage, their opening is also facilitated by binding of cAMP to their cytosolic CNBD (see [Chapter 3](#)). Therefore, cAMP binding orchestrates in an allosteric manner the position of the half activation voltage $V_{1/2}$, which in turn has an impact on the frequency of spontaneous action potentials. Due to their functional role in both the brain and heart, several disease-causing mutations related to HCN channels are known. For example, missense-mutations of the hHCN4 gene can cause different arrhythmia such as sudden arrhythmic death (Brugada syndrome) or bradycardia (i.e. sick sinus syndrome)⁵. For the neural system, pathogenic variants of hHCN1 have been associated

¹ Rioridan et al. (1989).

² Sosnay et al. (2011).

³ Ashcroft (2006).

⁴ Among many others: Marini et al. (2018); Hauf et al. (2020); Prins et al. (2020); Concepcion et al. (2021).

⁵ Baruscotti et al. (2010); Kim (2014); Rivolta et al. (2020).

with a broad spectrum of diseases including impaired learning, generalized epilepsy and even Alzheimer's disease⁶.

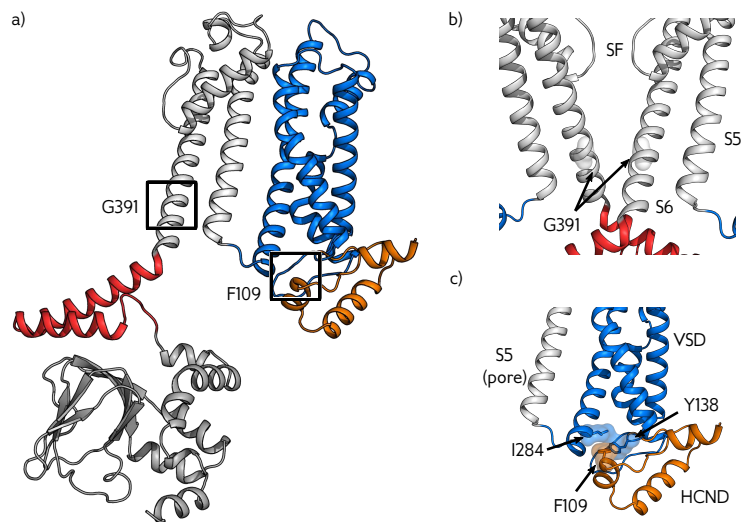
⁶ Santoro and Shah (2020).

⁷ Marini et al. (2018).

A recent genetic screening revealed several distinct missense-mutations of the hHCN1 gene of patients with infantile epilepsy⁷. One particularly interesting candidate was located at the C-terminal gate of S6 (residue G391, Figure 5.1a,b). The question arising from the genetic data was whether functional data of mutants can be linked to structural changes of the channel. In particular, mutation to more polar amino acids (HCN1_{G391D/C/S}) were shown to affect $V_{1/2}$ and/or led to dysfunctional channels (Section 5.2). Finally, residue F109 was another compelling candidate to employ computational mutation studies. Structurally, F109 in HCN1 is embedded into a hydrophobic pocket that interconnects various domains of the channel (Figure 5.1a,c). Here, structural analysis and data from patch-clamp experiments revealed that mutation of the corresponding amino acids in HCN2 (HCN2_{F151W/M/V/A/E}) alters $V_{1/2}$ and cAMP dependence (Section 5.3)⁸. For both residues, electrophysiological data were already present and thus MD simulations could be interpreted in the context of the observed phenotype.

⁸ Porro et al. (2019).

Figure 5.1: Overview of HCN1 (PDB: 5U6O) with investigated mutations. a) Side view of a single subunit of HCN1 in cartoon representation with colored domains: HCND (orange), VSD (blue), PD (white), C-linker (red) and CNBD (grey). b) 2 subunits of the HCN1 PD in side view. G391 is located at S6 and part of the cytosolic gate. c) Close-up view of the HCND. F109, Y138 and I284 form a hydrophobic pocket that interconnects the VSD, C-linker and S5-S6 loop. Relevant residues are represented as sticks with their Van der Waals (VdW) surface. See Appendix B for a structural alignment with other HCN isoforms.



5.2 MUTATION G391C/S/D

The starting point for comparative MD simulations of mutations G391C/S/D was a genetic data collection and experimental studies performed by an international collaboration of scientists focused on characterizing mutations of the HCN1 gene associated with epileptic encephalopathy^{9*}: several patients suffering from these symptoms were carriers of missense variants of the HCN1 gene where residue G391 was mutated to G391C/S/D, respectively. Functional characterization by collaboration partners via patch-clamp experiments showed that variants HCN1_{G391C} and HCN1_{G391S} resulted in a shift of the half activation voltage of -19 mV (Figure 5.2a) and 21 mV (Figure 5.2b), respectively.

⁹ Marini et al. (2018).

*Epileptic encephalopathy is an umbrella term for conditions characterized by seizures that contribute to severe neurological and cognitive impairment. See McTague and Cross (2013).

Heteromeric expression of wildtype (wt) and mutated gene-variants showed intermediate shifts. $\text{HCN1}_{\text{G391D}}$, the variant which leads to the most severe form of epilepsy in human, showed the biggest impact on channel function: cells expressing $\text{HCN1}_{\text{G391D}}$ exhibited close to no current in patch-clamp experiments (Figure 5.2c). If this was due to non-functional proteins or a trafficking deficit was not investigated. However, co-expression of $\text{HCN1}_{\text{wt/G391D}}$ was able to partially recover current in cells. Furthermore, recorded currents showed features specific to co-expressed subunits and were interpreted as evidence for the formation of heteromeric channels with poor conductance properties.

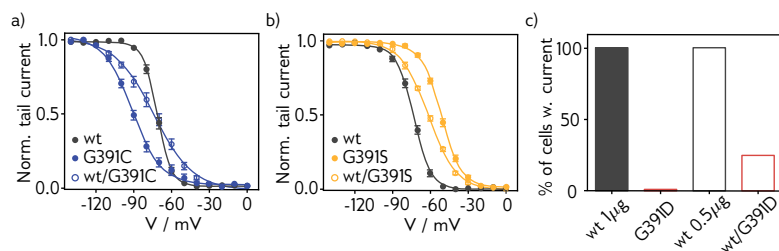


Figure 5.2: Functional impact of G391 mutations in HCN1 . a) Mean activation curves of HCN1_{wt} (black), homozygous $\text{HCN1}_{\text{G391C}}$ (blue, filled circles) and heterozygous $\text{HCN1}_{\text{G391C}}$ (blue, empty circles). b) The same plot as a) but for $\text{HCN1}_{\text{G391S}}$ (orange). c) Histogram over cells expressing a current with HCN1_{wt} (black) and $\text{HCN1}_{\text{G391D}}$ (red). Adopted from Marini et al. (2018).

For the present study, G391C/S/D mutations were introduced into the wt channel using homology modeling. The wt and mutant channels were then simulated for 100 ns to monitor how mutations alter the channels structure compared to the wt simulation (see Appendix C.1.1 for simulation details).

5.2.1 $\text{HCN1}_{\text{G391C/S}}$ show no major impact

In agreement with patch-clamp experiments, MD simulations of $\text{HCN1}_{\text{G391C}}$ and $\text{HCN1}_{\text{G391S}}$ showed no major impact on dynamics and structure of HCN1 when compared to the wt simulation. In both cases, a minimal opening of the central pore was observable, which was attributed to the larger space requirement of cysteine and serine side chains in this part of the protein (Figure 5.3). Both amino acids are ca-

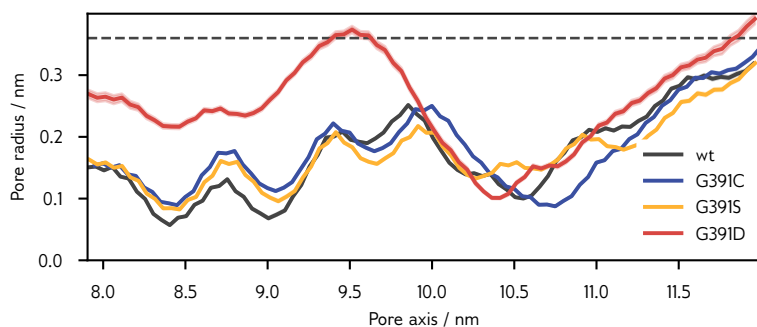


Figure 5.3: Pore radius of HCN1_{wt} and $\text{HCN1}_{\text{C/S/D}}$ during MD simulation. The plot shows the radii averaged over the last 50 ns of simulation. The SF is located approximately between 9.5 to 11.3 nm and the internal gate with residue 391 is located at approximately 8.4 nm. The dotted line corresponds to the estimated radius of hydrated K^+ ; see Moldenhauer et al. (2016).

pable of forming interhelical hydrogen bonds between their respective side chain OH/SH group and the carbonyl oxygen of residues located further downstream in the helix (n-3 or n-4)¹⁰. Analysis of hydrogen bonds in both mutations indeed revealed that they form interhelical hydrogen bonds to A387 (n-4) in all four subunits (Figure 5.4). Overall,

¹⁰ Gray and Matthews (1984); E.N. Baker and Hubbard (1984).

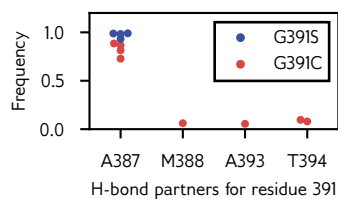
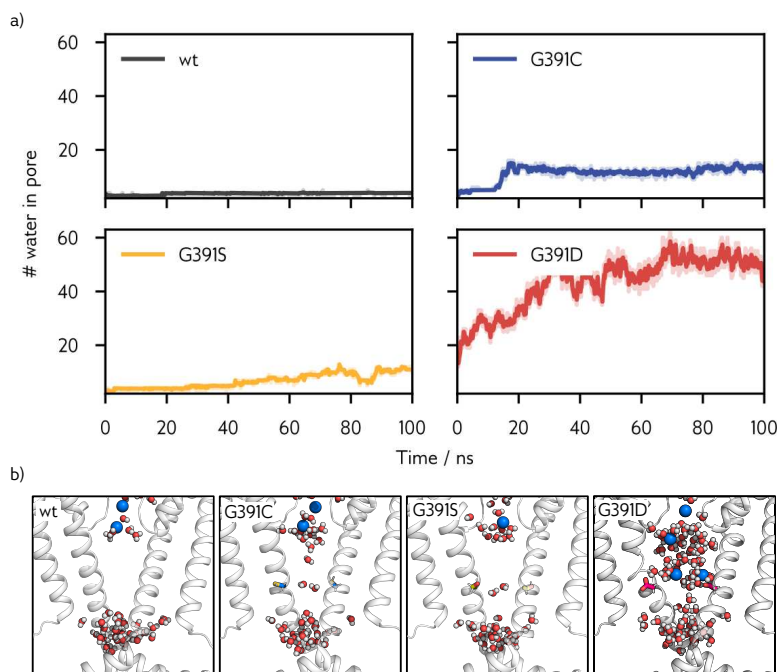


Figure 5.4: Frequency of observed hydrogen bonds between G391C/S and other residues in HCNIG391C/S. Individual observations belong to different subunits of the channel.

*Ions are expected to move through the gate in a solvated manner. This requires a pore radius of approx. 3.6 Å. See Moldenhauer et al. (2016).

Figure 5.5: Pore solvation of HCNIG_{wt} and HCNIG_{391C/S/D}. a) The running average of the number of water molecules inside the central cavity. b) Final snapshots of MD simulations. The internal gate (2 subunits) is shown as white cartoon from the side perspective with water molecules and ions as red/white and blue spheres, respectively. For clarity, only water molecules in proximity to the pore axis are shown. Also see Figure D.1.



resulted in a K⁺ being permanently trapped at the cytosolic entry. In this position, it was tightly coordinated by one or multiple D391 side chains. This finding is in good agreement with experimental data from patch clamp experiments that homomeric channels are not conductive, presumably because the trapped K⁺ blocks other ions from exiting the

these hydrogen bonds were more stable in the case of HCNIG_{391S} than HCNIG_{391C} with an average frequency of 0.97 and 0.82, respectively. For HCNIG_{391C}, the lower frequency was a result of occasional flips of the cysteine side chain to residues A393 and T394 of the neighboring S6 domain, thus cross-linking the two subunits. However, if these tiny difference in hydrogen bonding can lead to a stabilization of the closed state in one mutation, but destabilize it in the other case is questionable—it probably does not.

5.2.2 HCNIG_{391D} opens the channel

In contrast to the minor impact of serine and cysteine mutations, G391D resulted in an opening of the inner gate by approx. 3.2 Å (Figure 5.3). This can be attributed to the increased space requirement of the bulky aspartate side chain as well as to the electrostatic repulsion of four negative charges in close proximity. With a radius of 2.2 Å at the narrowest region of the C-terminal gate, the widening was still not big enough to allow free passage of K⁺ ions through the gate*. Nevertheless, widening of the inner gate resulted in an influx of water molecules into the central cavity of HCNIG_{391D} which was not observable in HCNIG_{wt} or HCNIG_{391C/S} (Figure 5.5). The amount of water inside the cavity after 50 ns of simulation was comparable with what would be expected for the open HCN pore (cf. Figure 5.5b and Figure 6.4b).

The presence of the negatively charged aspartate side chains further

central cavity. A similar inhibition mechanism was also found via MD simulations for Kcv-type K^+ channels previously¹¹.

¹¹ Tayefeh et al. (2007).

To further investigate how G391D influences channel function in homo- and heteromeric channels, MD simulations were performed with a truncated HCN_I variant where the VSD was cut off (Appendix C.1.1, HCN_I_{TMD} from here on) and the mutation was introduced either in all, or only a subset of the channels subunits. For the variant where all subunits were mutated to G391D, results were comparable between HCN_I and HCN_I_{TMD}: the internal gate was opening by several Å during the simulation, allowing influx of water molecules into the central cavity (see Figure D.4 for snapshots). Furthermore, the internal gate was blocked by the presence of tightly bound K^+ ions that did not leave the mutated site over 100 ns of simulation. In contrast, no ion was found at this location for the wt simulation (compare Figure 5.6a,e and b,f). In simulations where only two of the four subunits carried

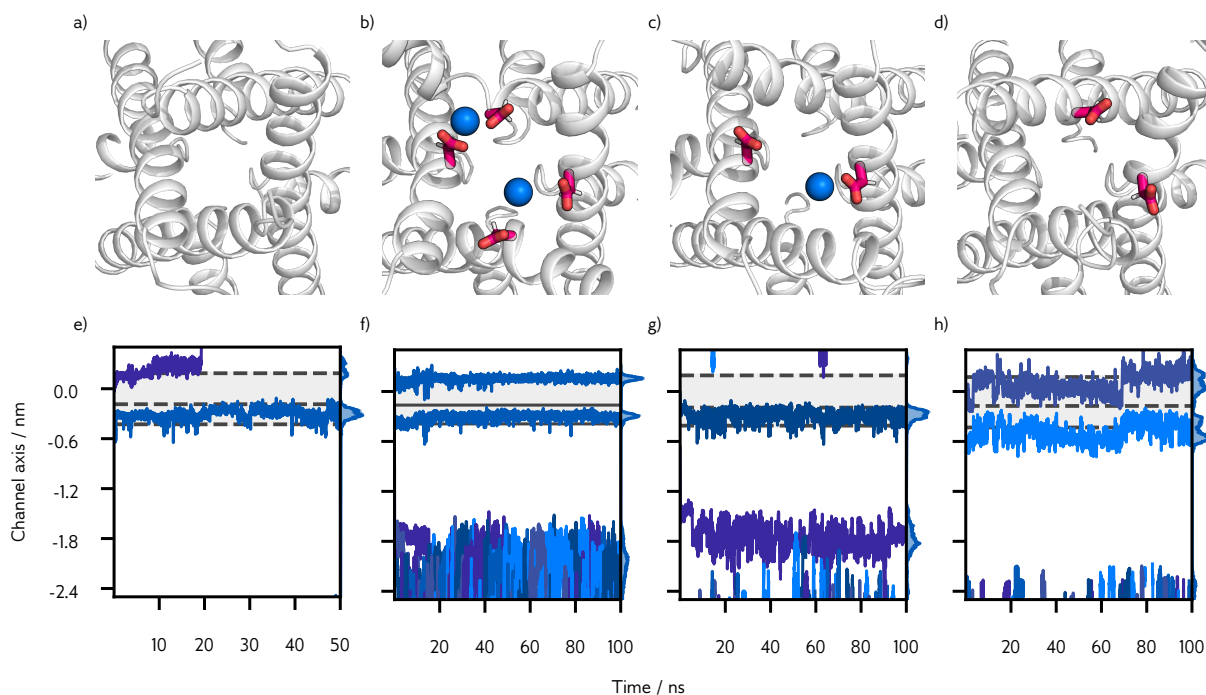


Figure 5.6: Representative snapshots of S6 domains in the bottom-up view and ion trajectories of a,e) HCN_I_{TMD},wt, b,f) homozygous HCN_I_{TMD},G391D, c,g) HCN_I_{TMD},wt/G391D with mutation in opposing subunits and d,h) in neighboring subunits. Trajectories of K^+ ions are shown along the z -axis of the HCN_I PD. The S₃ site is located at 0 nm and residue 391 at approx. -1.8 nm.

the G391D mutation, the phenotype depended on the arrangement of the subunits: When the mutation was introduced in opposing subunits (n and $n+2$), the channel exhibited similar behavior to the homomeric mutant, including solvent influx and trapping of K^+ at the gate (Figure 5.6c,g). However, in the simulation with the aspartate in neighboring subunits, the pore was not blocked by K^+ in proximity to the site of mutation (Figure 5.6d,h). Again, these results were in good agreement with experimental data that showed that at least a fraction of channels must generate a current in cells expressing HCN_I_{wt/G391}. With the combined experimental and computational data from MD simulations, it can be reasoned that this current is generated by heteromeric channels that carry the mutation in either only one or in

two neighboring subunits. Additionally, with the mutation in adjacent subunits, S6 helices show small deformations due to the asymmetric space requirement of mutated and wt subunits (Figure 5.6d). This asymmetric widening of the inner gate might be responsible for the large instantaneous current which was observed in patch clamp experiments¹².

¹² Marini et al. (2018).

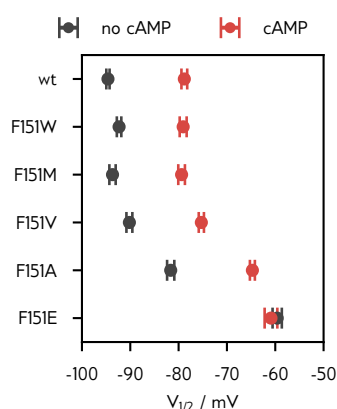


Figure 5.7: Experimentally determined half activation potential $V_{1/2}$ for investigated HCN2 F151 (F109 in HCN1) mutants in the absence (black) and presence (red) of 15 μ M cAMP. Adopted from Porro et al. (2019).

5.3 MUTATION F109W/M/V/A/E

F109 in HCN1 is a hydrophobic phenylalanine residue that is inserted into a hydrophobic pocket formed by F109, Y138, and I284/M287 (Figure 5.1). This pocket therefore interconnects the VSD and the PD and can in this way also transduce the opening signal of cAMP-binding to the CNBD since the HCND is strongly interconnected with the C-linker as well. Mutation of residue F151 in HCN2 (the equivalent of F109 in HCN1) to W/M/V/A/E all resulted in a shift of $V_{1/2}$ to positive values. Of note, F151E additionally resulted in a loss of cAMP-dependence in HCN2 (Figure 5.7), but other mutations did not.

To understand the impact of these amino acids (AAs) on the mechanical connection between different subunits of the channel, all five mutations were modeled on the HCN1 structure (HCN1_{F109W/M/V/A/E}) and investigated via MD simulations (see Appendix C.1.1 for simulation details). This allowed to investigate the effect of these mutations on the hydrophobic pocket in simulations.

5.3.1 HCN1_{wt} and uncharged variants are stable

In HCN1_{wt}, residue F109 was stably inserted into the hydrophobic pocket. Over 50 ns of simulation, none of the four subunits had the F109 side chain rotating out of the pocket. This can be seen by an average minimal distance between F109 and Y138 as well as F109 and I284 of 3.1 Å (95 % CI: 3.09-3.12) and 2.5 Å (95 % CI: 2.53-2.54), respectively (Figure 5.8).

Step wise mutation of F109 to smaller and less hydrophobic residues resulted in a step-wise increase of the minimal distance between residue 109 and Y138 in all subunits, while other distances remain unaffected: In agreement with experimental data that showed no big difference between HCN2_{wt} and HCN2_{F151W}, this mutation also showed no strong effect on the hydrophobic pocket. Chemically, both AAs are equivalent regarding their hydrophobicity and both feature a bulky, aromatic side chain. In HCN1_{F109M}, HCN1_{F109V}, HCN1_{F109A}, the distance increased to 5.49 Å (95 % CI: 5.45-5.53), 6.38 Å (95 % CI: 6.36-6.40) and 6.96 Å (95 % CI: 6.94-6.99), respectively. We can therefore see, that the protein does not compensate the loss in hydrophobic contacts via a tighter packing of respective domains, but rather keeps its conformation at the expense of a loss in interaction potential between AAs that form the hydrophobic pocket*. Strikingly, the increase in distance follows a very similar pattern to the shift in $V_{1/2}$ in corresponding mutations in HCN2 by electrophysiology experiments (Spearman correla-

*The van der Waals interaction potential decreases with r^{-6} and thus quickly becomes small.

tion $\rho_S=0.83$, $p=0.04$, Table 5.1). With this good correlation between structural and functional data it is reasonable to assume that the increase in distance and associated loss in hydrophobic contact surface can be seen as a direct indicator for the observed $V_{1/2}$ shift.

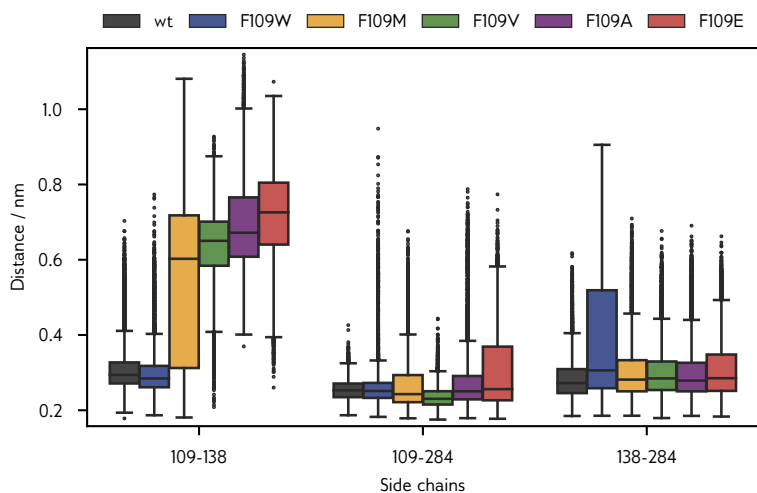


Figure 5.8: Side chain distances between different residues of the hydrophobic pocket made by residues 109, 138 and 284 in HCN1_{wt} and $\text{HCN1}_{\text{F109W/M/V/A/E}}$.

Table 5.1: Spearman correlation coefficients (ρ_S) and corresponding p-values for the average smallest distance (Figure 5.8) and half activation voltage shift $\Delta V_{1/2}$ (Figure 5.7).

Side chain	cAMP?	ρ_S	p
109-138	yes	0.83	0.04
	no	0.83	0.04
109-284	yes	0.43	0.40
	no	0.60	0.21
138-284	yes	-0.09	0.87
	no	0.37	0.47

5.3.2 $\text{HCN1}_{\text{F109E}}$ disrupts the hydrophobic pocket

While mutations F109W/M/V/A still lead to an insertion of the side chain into the hydrophobic pocket, this was not the case for F109E. Instead, the side chain of E109 rotated out of the hydrophobic pocket into to solvent (compare Figure 5.9a and b). This can also be seen in the sol-

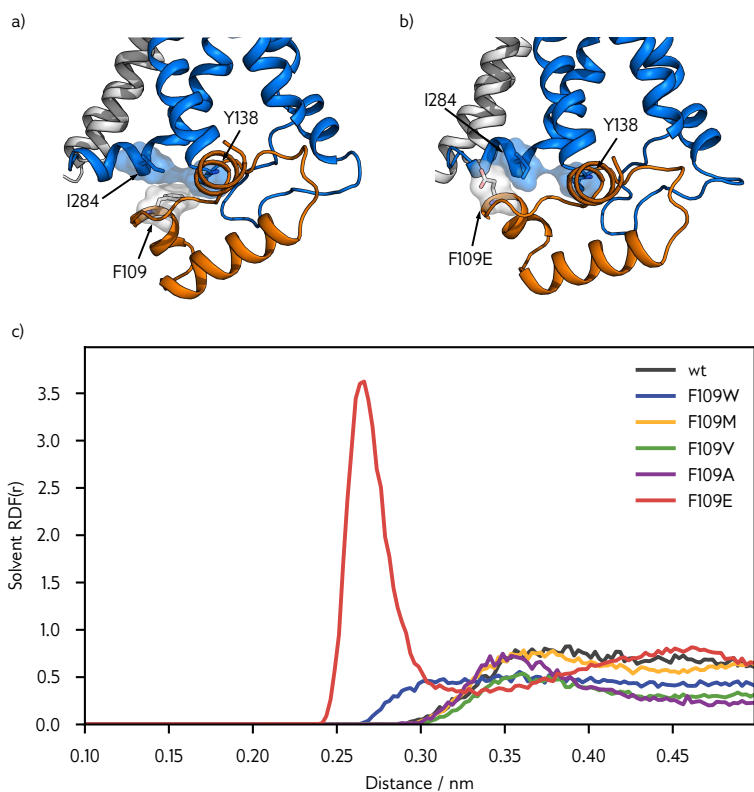


Figure 5.9: a-b) Representative snapshot of the HCND of a) HCN1_{wt} and b) $\text{HCN1}_{\text{F109E}}$. The HCND and VSD are shown as orange and blue cartoon, respectively. Residues 109, 138 and 284 are shown as sticks with their corresponding VdW surface. Snapshots for other mutations can be found in Figure D.9. c) Solvent radial distribution function (RDF) for residue 109 side chains in HCN1_{wt} and $\text{HCN1}_{\text{F109W/M/V/A/E}}$. Only F109E shows the profile of a solvated side chain.

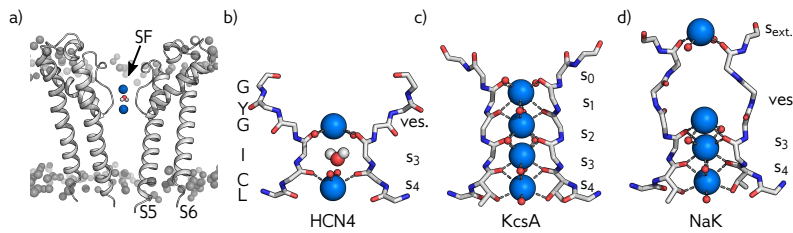
vent radial distribution function $RDF(r)$, that represents the probability of finding a water molecule at the given distance from a given point (Figure 5.9c). In agreement with the distance measurements described above, the RDF of $HCN_{I_{wt}}$ as well as $HCN_{I_{F109W/M/V/A}}$ show the course of buried residues with no solvent contact. In contrast, the prominent peak at 2.6 Å in the RDF plot for $HCN_{I_{F109E}}$ represents the first hydration shell of carboxyl oxygens and thus shows that the glutamic acid side chain is fully solvated in all four subunits. Interestingly, even for $HCN_{I_{F109E}}$, the altered position does not result in a significant change of the relative orientation or stability of the HCND or VSD. Across the whole mutation spectrum, no further disordering of this region was observable in RMSD or RMSF (Figure D.7 and Figure D.8).

In conclusion, the combination of experimental and computational data can give the following explanation for the influence of the hydrophobic pocket on voltage-dependence: Residues F109, Y138 and I284 form a crucial interaction site that connects VSD and PD. Already small changes in the interaction between these residues can therefore lead to a shift in the $V_{1/2}$ value—as can be seen in $HCN_{I_{W,M,V,A}}$. Finally, in case of $HCN_{I_{F109E}}$, the hydrophobic pocket is fully destroyed since one residue rotates out of the pocket. This disruption does not only lead to the largest shift in $V_{1/2}$, but also abolishes the sensitivity of the channels to cAMP binding. Therefore, the HCND is not only a key element for the signal transduction between VSD and PD, but also for the signal transduction between the CNBD and the transmembrane part of HCN channels.

CHAPTER 6

Ion Conduction in HCN Channels

6.1 INTRODUCTION



HCN channels contain the GYG signature sequence in the SF which is common to all selective K^+ channels. Nevertheless, they discriminate only moderately between K^+ and Na^+ with a preference of 2–6:1 while selective K^+ channels typically show selectivity ratios of 10:1 or higher¹. This weak K^+/Na^+ selectivity is mandatory for HCN channel function in that it guarantees an influx of both ions into the cells upon HCN activation. This is the basis for the progressive depolarization, which drives the free running voltage to the threshold for an action potential. A comparison of the canonical SF motif of selective K^+ channels with the respective domain of the Cryo-EM structures of the HCN4 isoforms (Figure 6.1a,b) gives a possible explanation: The SF of selective K^+ channels like KcsA (Figure 6.1c) adopts a conformation with four binding sites (s_1 to s_4) where K^+ is coordinated by eight oxygen atoms². These interactions effectively mimic the hydration shell of an ion when it moves through the SF. A fifth binding site (s_0), where ions are only partially desolvated, has been identified above s_1 . In contrast to K^+ , the smaller Na^+ ions were found not to bind to these oxygen cages. Instead, Na^+ ions preferably occupy the planes (p) between K^+ binding sites (Figure 6.2)³. Here, planes are labeled according to their neighboring K^+ binding sites and thus p_{12} corresponds to the oxygen plane between sites s_1 and s_2 .

Contrary to the SF of canonical K^+ channels, the SF of HCN4 adopts a conformation with only two of the canonical four binding sites (s_3 and s_4)⁴. Carbonyl oxygens of the glycine residue (G481 in HCN4), which would usually form s_2 , are rotated away from the central axis. Binding sites s_0 to s_2 are thus replaced by a funnel-shaped, fully-solvated vestibule above the SF. Additionally, because T is replaced by C (C479 in HCN4) at the beginning of the SF sequence, the s_4 site in HCN4 is significantly wider than s_4 in highly selective K^+ channels. This presumably further reduces selectivity in HCN channels and leaves the SF with only a single canonical binding site (s_3). With these features, the SF of HCN more closely resembles the SF of the non-selective NaK channel (Figure 6.1d). Also, the latter features a similar vestibule above its two K^+

Figure 6.1: Overview of the open HCN4 PD and SF (PDB: 7NP3). a) Side view of the HCN4 PD embedded into a POPC bilayer with K^+ (blue) and water (red/white) inside the SF. Only two subunits are shown for clarity. b) Close-up view of the SF of HCN4 with labeled amino acids (L478–G483) and binding sites. c–d) The SF of KcsA (PDB: 1K4C) and NaK (PDB: 3E8H), respectively. Interactions between the SF and ions are shown as dashed lines and oxygens of the hidden two subunits are shown as red spheres.

¹ Ludwig et al. (1998); Santoro, Liu, et al. (1998); Gauss, Seifert, and Kaupp (1998); Moroni et al. (2000).

² Doyle et al. (1998).

³ Thompson et al. (2009); Egwolf and Roux (2010).

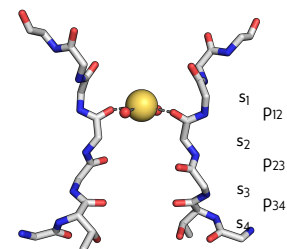


Figure 6.2: X-Ray structure of the KcsA SF with Na^+ bound to a carbonyl plane (PDB: 2ITC).

⁴ Lee and MacKinnon (2017); Saponaro et al. (2021).

binding sites. However, in NaK, we can find an additional ion binding site (s_{ext}) upstream of the basin and s_4 is maintained as selective potassium binding site with a shape similar to the one found in K^+ channels⁵. Interestingly, even though NaK has more ion binding sites than HCN channels, it is basically non-selective for K^+ while HCN channels maintain weak selectivity. The reason for this is presumably related to the ability of NaK to adopt different conformations that facilitate either K^+ or Na^+ conduction⁶.

⁵ Alam and Jiang (2009).

⁶ Shi et al. (2018); Roy et al. (2021).

⁷ Saponaro et al. (2021).

A Cryo-EM structure of HCN4 was recently revealed in several different conformations—some of them featuring a widened PD⁷. In order to confirm that these structures represent an open conformation, the present study presents several methods to characterize the conduction pathway through the pore (Section 6.2). Furthermore, classical MD simulations (Section 6.3) and free energy calculations (Section 6.4) were used to provide insight into the mixed K^+/Na^+ conduction mechanism. Based on this data, a theory explaining unique features of HCN conductance is presented.

6.2 CHARACTERIZATION OF THE HCN4 PORE

⁸ Moldenhauer et al. (2016).

The pore radii of solved HCN4 structures were calculated with HOLE (Appendix C.2.1). Like HCN1 solved in presence of cAMP, also holo HCN4 showed the pore profile of a closed HCN channel (Figure 6.3a,c,e). Surprisingly, this was not the case for the apo structure of HCN4. Here, HOLE calculations revealed that the pore was significantly widened compared to the holo structure (Figure 6.3b,e). The smallest width of the internal gate—located approximately at the position of T515—was 3.38 Å. This is a value close to what has been suggested as the width required for the passage of solvated K^+ and the gate opening should therefore be sufficient to allow passage of ions⁸.

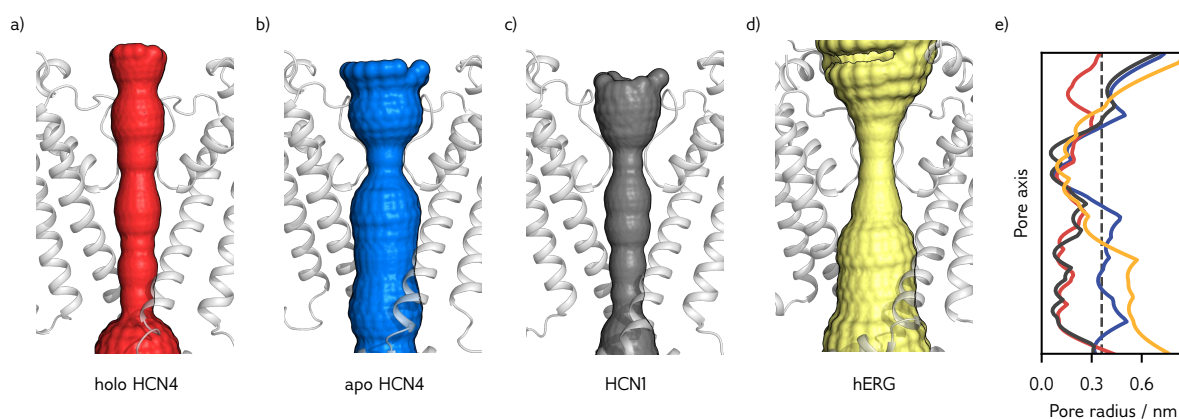
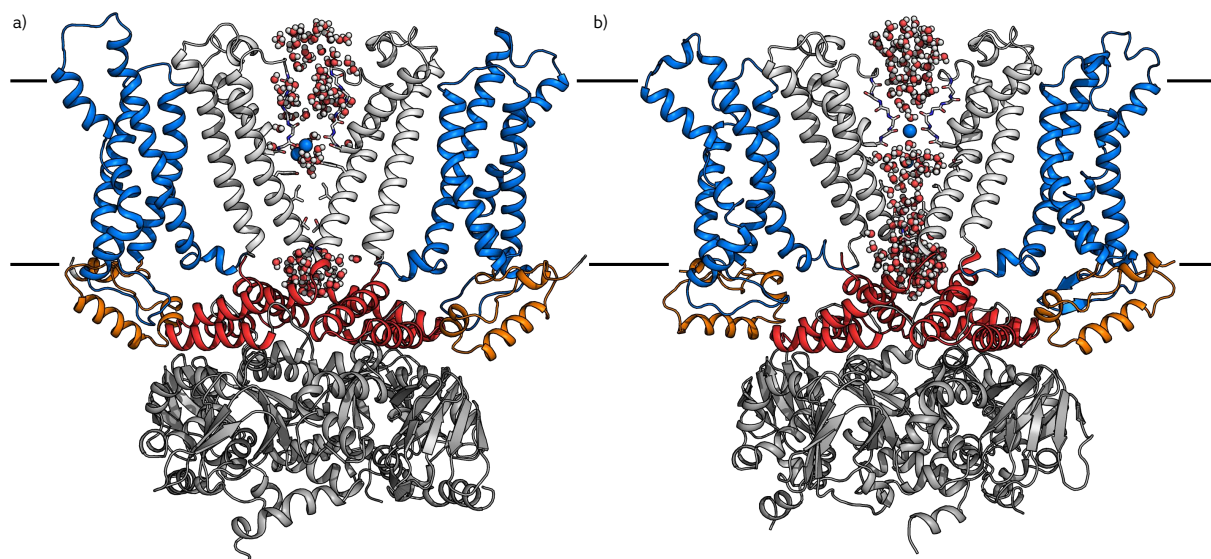


Figure 6.3: Comparison of pore radii of a) closed HCN4_{holo} (red, PDB: 7NP4), b) open HCN4_{apo} (blue, PDB: 7NP3), c) closed HCN1 (grey, PDB: 5U6P) d) open hERG (yellow, PDB: 5VA2). two subunits of the PD are shown as white cartoon with the colored pore surface. e) Plot of the respective pore radii. The dotted line at 3.6 Å represents a solvated K^+ .

At this point, it should be mentioned that the structures of other solved potassium channels in open conformation show an even bigger pore widening: i.e the pore of open hERG (Figure 6.3d,e) features a radius of approximately 5 Å at the internal gate; similar large widths were

reported for the open channel structure of a diverse set of potassium channels including KvChim (PDB: 2R9R), KcsA (PDB: 3F5W), MthK (PDB: 3LDC)⁹.

6.2.1 Pore Solvation



To investigate if the widened gate allows passage of ions, MD simulations of the full HCN4 channels were run (see [Appendix C.2.3](#) for simulation details). In the simulation of HCN4_{holo}, the central pore remained desolvated over the full 100 ns of simulation ([Figure 6.4a](#)), thus confirming that the pore is closed. In contrast, the HCN4_{apo} simulation showed clear signs of an open pore: water molecules were present along the full length of the channel axis ([Figure 6.4b](#)). This finding was also supported by the exchange rate of water molecules between the central cavity and the bulk solvent. To illustrate this, [Figure 6.5](#) shows the number of individual water molecules that visited the central cavity over the simulation. It can be seen that a rapid exchange of water

Figure 6.4: Pore solvation in HCN4. Snapshots of closed HCN4_{holo} (a) and open HCN4_{apo} (b). Proteins are shown as cartoon with water and K⁺ ions along the channel axis as red/white and blue spheres, respectively. For clarity, only two subunits are shown for TMHs. Individual domains of the protein are colored in blue (VSD), white (pore), orange (HCND), red (c-linker) and grey (CNBD).

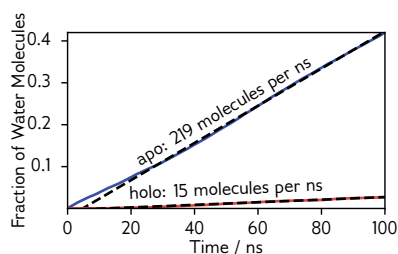


Figure 6.5: The fraction of water molecules that visited the central cavity of HCN4_{holo} (red) and HCN4_{apo} (blue) over the simulation time at least once.

between the cavity and bulk solvent through the cytosolic gate exists only for HCN4_{apo}: here, the slope of the regression line corresponds to 219 molecules/ns. Applying the same method for HCN4_{holo} counts only 15 molecules/ns. Additionally, for HCN4_{holo} water exchange happened exclusively through the collapsed SF. Here, it is important to note that the calculated rate does not correspond to a real exchange rate since

multiple visits of the same molecule are not counted. Nevertheless, it is a meaningful measurement to evaluate the pore width. This approach is much easier to calculate than a real exchange rate where multiple visits of the same molecule must be counted.

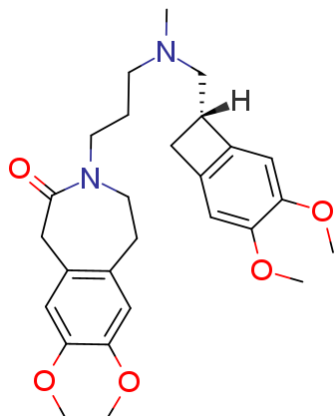


Figure 6.6: Structural formula of ivabradine.

¹⁰ Bucchi, Baruscotti, et al. (2013); Tanguay, Callahan, and D'Avanzo (2019).

¹¹ Bucchi, Tognati, et al. (2006); Bucchi, Baruscotti, et al. (2013); Tanguay, Callahan, and D'Avanzo (2019).

¹² Tanguay, Callahan, and D'Avanzo (2019).

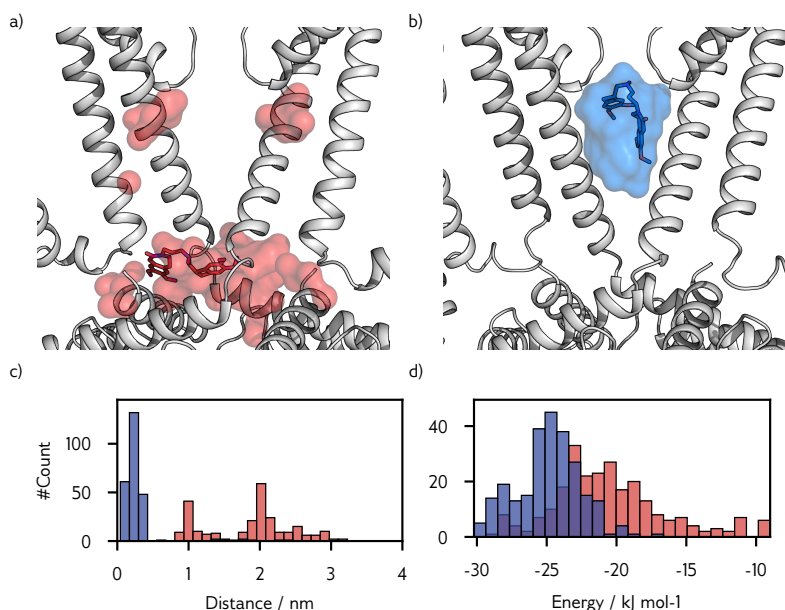
6.2.2 Ivabradine Docking

A final evidence that the structure of HCN₄_{apo} shows a physiologically relevant open pore comes from docking experiments with ivabradine (Figure 6.6). Ivabradine is a known channel blocker for HCN channels that binds inside the central cavity¹⁰. Experimental and computational studies have shown that binding of ivabradine requires pore opening—presumably because the entering pathway is through the cytosolic gate¹¹.

Therefore, docking experiments with ivabradine were performed on several HCN structures (Appendix C.2.2). In agreement with the described mode of blocker action and the expectation that HCN₄_{holo} is a closed structure, docking of ivabradine to HCN₄_{holo} resulted in no successful binding inside the internal cavity. Instead, ivabradine randomly associated to the hydrophobic surface of the membrane-embedded TMHs of the channel or to the cytosolic gate (Figure 6.7a, best binding affinity: $-29.04 \text{ kJ mol}^{-1}$). In this sense the results were very similar to what has been reported for ivabradine docking to closed HCN₁ structures previously¹².

In contrast, docking of ivabradine to HCN₄_{apo} resulted in successful binding of the blocker inside the hydrophobic cleft of the pore (Figure 6.7b, affinity: $-30.21 \text{ kJ mol}^{-1}$). Here, 243 of 250 (97 %) docking attempts resulted in the final pose inside the pore (Figure 6.7c).

Figure 6.7: Docking of ivabradine to a) HCN₄_{holo} and b) HCN₄_{apo}. Two chains of the pore unit are shown as white cartoon, ivabradine is shown as colored sticks (pose with highest affinity only). Transparent surfaces represent regions with high docking density calculated over 250 docking attempts. c) Distances of docked ivabradine poses from the central cavity of the PD of HCN₄_{holo} (red) and HCN₄_{apo} (blue). d) Distribution of binding affinities for ivabradine docking.



From successful docking attempts, it becomes apparent that ivabradine does not show a preferential binding mechanism inside the HCN4 cavity. Instead, results from docking experiments show a quasi-continuum of different poses. This is visualized by the blue surface in [Figure 6.7b](#). These poses differ in their binding affinity ranging from -20 to -33 kJ mol^{-1} ([Figure 6.7d](#)). Contacts between the blocker and HCN4 are mainly of hydrophobic nature and particularly between residues of the S6 helix and residues of the lower part of the SF (residues L478, A508, I511). Again these results are in good agreement with what has been obtained for an artificially open homology model of HCN1, where “bradine’ inhibitors appear to bind to the HCN1 open pore in geometrically unconstrained manner via primarily van der Waals and hydrophobic interactions”¹³.

Therefore, successful docking of ivabradine to HCN4_{apo}, but not HCN4_{holo}, confirms that one structure is in the open state while the other is not. Only for the open structure, the blocker is able to pass the widened gate at the cytosolic entrance of the channel.

¹³ Tanguay, Callahan, and D’Avanzo (2019).

6.3 ION CONDUCTION MECHANISM

Taking advantage of the open HCN4 pore, multiple MD simulations were run on basis of the HCN4_{apo} PD (residues L412 to S523, [Figure 6.1a](#)). Therefore, constant electric fields in the range of -300 to -700 mV and different concentrations of KCl and NaCl ranging from 150 to 900 mM were used (see [Appendix C.2.3](#) for simulation details). These unphysiologically high electric fields and ion concentrations are generally used to increase the conduction rate and thus the probability to observe ion conduction events during limited simulation times. It is important to mention that simulations with lower voltages gave similar results ([Appendix D.3](#)). Hence the high electrical fields, which were used in a majority of simulations were not causing an artifact. This has also been seen in several other studies¹⁴.

6.3.1 Potassium conduction

In 900 mM KCl and with an applied electric field of -500 mV the conduction of a total of 9 K^+ ions was observable over four independent simulations with a total simulation time of 2100 ns. This conduction rate of 4.3 ions/ μs closely resembles the low pS conductance of HCN channels (approximately 1 to 10 ions/ μs) which has been experimentally determined for HCN channels¹⁵.

In [Figure 6.8a](#), an example trajectory of a K^+ ion moving through the SF is shown. Full trajectories including several transitions and trajectories recorded under different conditions are shown in the appendix ([Appendix D.3](#)). Here, dashed lines represent carbonyl oxygens of residues L478 to I480 and binding sites are labeled as described in [Section 6.1](#). K^+ conduction occurred as an alternation between two main ion configurations with either a single ion bound to the SF (state: $[\text{p}_{34}, \text{cav}]$) or two ions bound to the SF (state: $[\text{p}_{23}, \text{s}_4, \text{cav}]$), respectively ([Fig-](#)

¹⁴ i.e. Stock et al. (2013); Köpfer et al. (2014); Andersson, Kasimova, and Delemotte (2018).

¹⁵ DiFrancesco (1986); Johnson and Zagotta (2005).

Figure 6.8: K^+ conduction mechanism. a) Trajectory of K^+ ions along the channel axis. Different ions are shown in different shades of blue. The shaded area corresponds to the SF and the position of carbonyl oxygens of residues L478 to I480 are shown as dashed lines. The K^+ probably density is shown on the right y-axis. The labels 1-5 above the plot correspond to the structures in subplot b. b) Snapshots of the SF following the trajectory of a single ion from the external side into the central cavity. The SF of HCN₄ is shown as colored sticks and K^+ ions and water are shown as blue and red/white spheres, respectively. For clarity, only two of the four subunits of HCN₄ are shown.

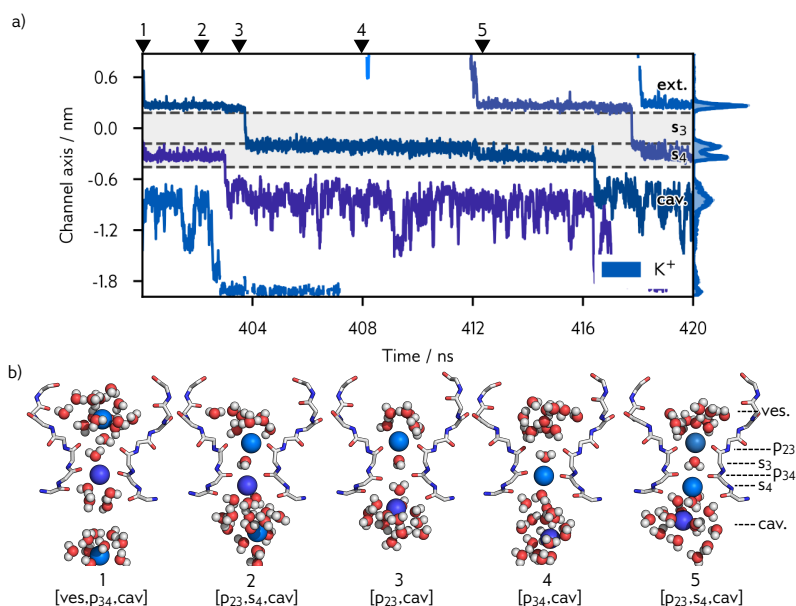


Figure 6.8b): starting from a configuration with a single bound ion (state 1: $[ves, p_{34}, cav]$), a newly arriving ion can move through the funnel-shaped vestibule and bind to p_{23} . Here, it is coordinated by carbonyl oxygens from I480. Binding of this second ion displaces the already bound ion from the carbonyl plane p_{34} (G479 oxygens) into s_4 (state 2, $[p_{23}, s_4, cav]$). In this state both ions are only weakly coordinated by a single carbonyl oxygen plane (either G479 or I480) and partially solvated by water molecules from the central cavity below or vestibule above the SF, respectively. With two ions bound, conduction then takes place once the lower ion leaves s_4 into the central cavity (state 3: $[p_{23}, cav]$). At the same time, the upper ion moves through s_3 and to the p_{34} plane (state 4, $[p_{34}, cav]$)—thus resetting the initial configuration with only a single ion bound to the SF. Subsequently, a new ion can bind to repeat the conduction process (state 5: $[p_{23}, s_4, cav]$).

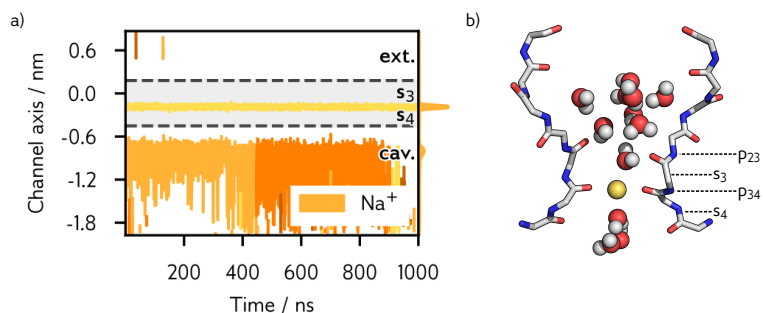
With this mechanism, K^+ conduction in HCN channels follows a “soft knock-on” mechanism. Ions move through the SF by visiting sites p_{23} , p_{34} and s_4 while staying separated by at least a single water molecule (cf. Section 6.5). Remarkably, binding to s_3 cannot be seen as a stable configuration for K^+ in these simulations. Instead, K^+ ions prefer binding to the carbonyl oxygen planes of C479 (p_{34}) and I480 (p_{23}). This coordination mode has been reported for Na^+ ions in other channels (i.e. NaK) but has never been reported for a K^+ ion¹⁶. The observed conduction mechanism for K^+ in HCN₄ is hence remarkably different from what has been reported previously for canonical K^+ channels.

¹⁶ Vora, Bisset, and Chung (2008).

6.3.2 Sodium and Mixed Sodium/Potassium Conduction

In contrast to simulations in KCl solution, simulations with only NaCl did not produce subsequent ion conduction events independent of the applied transmembrane potential or ion concentration (total simula-

tion time: 4500 ns). Instead, Na^+ binds tightly to p_{34} (state $[p_{34},\text{cav}]$) over long simulation periods (Figure 6.9). Here, it is coordinated in a similar fashion to K^+ in the one-ion configuration and interacts with carbonyl oxygens of G479 as well as water molecules bound to s_3 and s_4 . This finding is in good agreement with experimental data which has shown that Na^+ can not conduct alone through HCN channels but requires the presence of K^+ ¹⁷.



¹⁷ Lyashchenko and Tibbs (2008).

Figure 6.9: Sodium is not conducted through the SF. a) Trajectory of Na^+ ions along the channel axis analogous to Figure 6.8. Different Na^+ ions are shown in different shades of yellow. b) Representative snapshots of the HCN4 selectivity filter with a bound Na^+ .

To test the hypothesis whether Na^+ conduction is diminished in the absence of K^+ because a second Na^+ fails to displace an already bound Na^+ from the p_{34} plane, several simulations were run with both ion species present in solution. In these simulations, Na^+ showed similar binding patterns to the SF than K^+ and several conduction events—for K^+ as well as Na^+ —where observable. The trajectory in Figure 6.10a,b shows how a Na^+ ion that was initially placed in the SF (state 1: $[p_{34},\text{cav}]$) is replaced by K^+ . Of note, the state with two ions bound to p_{23} and s_4 (state 2: $[p_{23},s_4,\text{cav}]$) seen in KCl simulations was only transiently observable when a K^+ replaces a Na^+ in the SF in all cases. After several K^+ conduction events that lead to state 3: $[p_{34},\text{cav}]$, another Na^+ enters the SF (state 4: $[p_{23},s_4]$) and resets the initial configuration (state 5, $[p_{34},\text{cav}]$). Here, the two-ion state is again visible—probably because binding of K^+

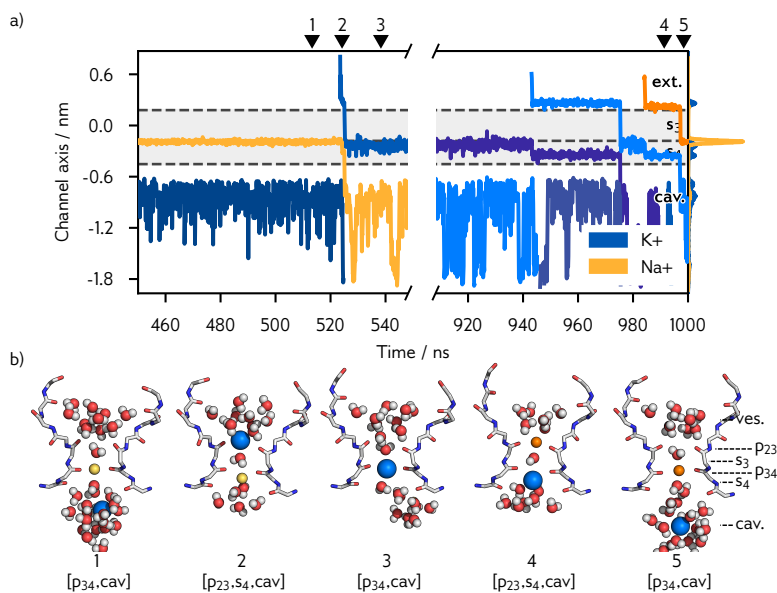


Figure 6.10: Mixed Na^+/K^+ conduction mechanism. a) Trajectory of K^+ and Na^+ ions along the channel axis. Different ions are shown in different shades of blue (K^+) and orange (Na^+). The shaded area corresponds to the SF and the position of carbonyl oxygens of residues L478 to L480 are indicated as dashed lines. The ion probability density is shown on the right y-axis. The labels 1-5 above the plot correspond to the structures in subplot b. b) Snapshots of the MD simulation following the trajectory of a single Na^+ ion from the SF into the central cavity and subsequently another Na^+ into the SF. The SF of HCN4 is shown as colored sticks and K^+ ions and water are shown as blue and red/white spheres, respectively. For clarity, only two of the four subunits of HCN4 are shown.

to s_4 is more favorable than the same state for Na^+ . This is a plausible assumption given that (partial) desolvation of Na^+ usually comes with a higher loss in free energy compared to K^+ under similar conditions ($\Delta G_{\text{hyd}}(\text{Na}^+) = -365 \text{ kJ mol}^{-1}$ and $\Delta G_{\text{hyd}}(\text{K}^+) = -295 \text{ kJ mol}^{-1}$)¹⁸.

¹⁸ Marcus (1994).

In total, over 7600 ns of simulations with mixed ion species, Na^+ was displaced from its position by K^+ 3 times while the same event happened only once without the presence of K^+ (although K^+ was still present in solution, Table 6.1). These simulations therefore represent a plausible mechanism for the experimental finding that conduction of Na^+ is limited by the absence of K^+ while K^+ conduction is not. For K^+ , both ion species are capable of displacing an already bound ion out of the p_{34} plane into s_4 and subsequently into the cavity. This allows K^+ to conduct through the pore independent of the incoming second ions species. In contrast, the same “kick-off” for Na^+ conduction apparently requires the presence of K^+ . This results in intrinsic selectivity for K^+ over Na^+ since only the former can conduct independently of the incoming second ion.

Finally, even though the statistics are rather low, the ratio of observed conduction events in mixed simulations is in overall good agreement with experimentally determined selectivity in HCN channels in general (Table 6.1). For K^+ , 11 full conduction events were observable while only four Na^+ ions were conducted through the SF (ratio $\approx 3:1$). Experimental data suggests a 2-6:1 ratio for K^+ over Na^+ ¹⁹. In agreement with data from pure KCl simulations, the water/ions permeation ratio was 1.0 in mixed simulations, indicating that also mixed ion conduction follows a soft knock-on mechanism.

¹⁹ Ludwig et al. (1998); Santoro, Liu, et al. (1998); Gauss, Seifert, and Kaupp (1998); Moroni et al. (2000).

Table 6.1: Statistics of ion conductance in simulations with different ion species. Details on simulation parameters can be found in the Table C.2.

Simulation	Pure K^+	Pure Na^+	1:1 $\text{K}^+:\text{Na}^+$
# Independent Simulations	4	5	15
Total simulation time / ns	2100	4500	7600
Simulations w/ conduction	2	0	7
Simulations w/o conduction	2	5	8
Permeation			
K^+	9	-	11
Na^+	-	0	4
Water	9	0	15
Co-permeation (water:ions)	1.0	1.0	1.0
Selectivity ($\text{K}^+:\text{Na}^+$)	-	-	2.75
Selectivity			
K^+ replacing K^+	9	0	7
K^+ replacing Na^+	-	-	3
Na^+ replacing K^+	-	-	4
Na^+ replacing Na^+	-	0	1

6.3.3 Increased SF Flexibility Facilitates Unusual Binding Patterns

Experimental data such as electron density maps and NMR data, but also various *in-silico* studies show that K^+ almost exclusively binds to carbonyl oxygen cages (s_1 to s_4) in the canonical SF motif which is common to all K^+ channels²⁰. Binding to carbonyl planes (p_{12} to p_{34}) has only been reported for smaller and harder cations such as Na^+ and Li^+ , i.e. in channels like KcsA, MthK and NaK²¹. Furthermore, several studies explicitly link these K^+ binding patterns to the observed diffusion-limited conduction speed and selectivity. In K^+ channels, distances between carbonyl oxygens are thought to be tailored in such a way that they provide a solvent-like milieu for K^+ . This in turn lowers free energy barriers encountered by K^+ while entering the SF and subsequently moving between binding sites. For Na^+ , a similar ideal environment is not available in K^+ channels and thus transition between the carbonyl planes comes with a much higher energetic cost.

To support the typical fast conduction for K^+ , the SF of K^+ channels has to be rather rigid during conduction. Ions move through the selective SF motif with a speed that does not give room for any dynamic adaption of the SF. Otherwise, this adaption would be the a limiting factor for channel conductance in K^+ channels. Therefore, the conformation—and more specifically the width of binding sites—stays almost constant during individual conduction events and does not depend on the position of bound ions²². In contrast, in this study the SF of HCN4 shows itself to be highly dynamic during K^+ conduction. Figure 6.11a,b shows the probability density function of the width of the SF at the height of carbonyl oxygen atoms of residues C479 and I480 during a single K^+ conduction event. With a single K^+ bound to p_{34} , the distance between carbonyl oxygens atoms of C479 significantly increase by $\approx 0.5 \text{ \AA}$ compared to the Cryo-EM structure (5.3 \AA vs. 4.8 \AA). For residue I480, carbonyl oxygen atoms adopt a state where they are closer together compared to the Cryo-EM structure (5.9 \AA vs. 6.3 \AA). With two ions bound to $[p_{23}, s_4]$, these distances are then reduced and the width at C479 returns to a value close to that measured in the Cryo-EM structure (4.7 \AA). A similar shrinking is also observable for I480 (5.5 \AA vs. 5.9 \AA). However, this position shows to be much more flexible in general and changes are only hardly distinguishable from the thermal motion of atoms itself. Close inspection of the SF shows that changes in dimension are mainly a result of carbonyl distortions: carbonyl oxygen atoms rotate laterally away from the principal axis of the channel with only limited movement of the carbonyl backbone (cf. Figure D.11).

Of note, binding of Na^+ to p_{34} does not result in such a widening of the SF. Instead, carbonyl distances of C479 and I480 remain at 4.7 \AA and 5.7 \AA , respectively (Figure 6.11c,d). Widening of the SF is therefore a unique adaption of HCN channels to K^+ ions. By this, K^+ as well as Na^+ can bind to carbonyl oxygen planes which in turn increases the number of possible binding sites for K^+ from (the canonical s_3 site) to three (p_{23} , p_{34} and s_4). It is reasonable to assume that this increased flexibility

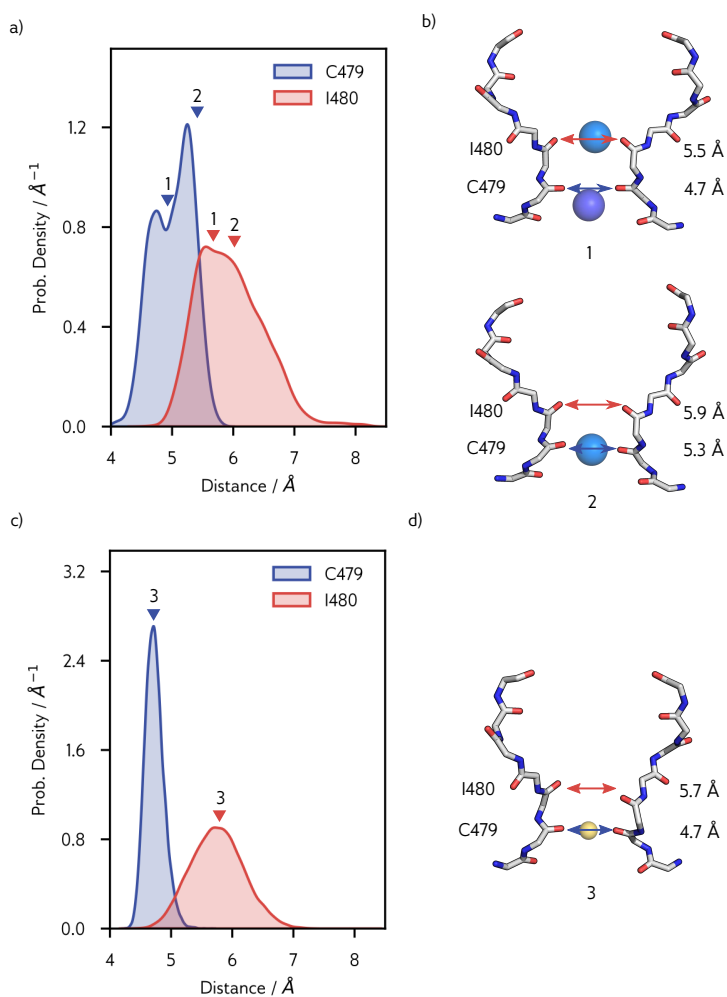
²⁰ i.e. Doyle et al. (1998); Zhou, Morais-Cabral, et al. (2001); Zhou and MacKinnon (2003); K. A. Baker et al. (2007); Derebe et al. (2011). Also see Mironenko et al. (2021).

²¹ Vora, Bisset, and Chung (2008); Thompson et al. (2009); Egwolf and Roux (2010); Kopec et al. (2018).

²² Heer et al. (2017); J. Li et al. (2018).

of the SF and dynamic adaption of binding sites to the bound ion contributes to the retained selectivity in HCN channels compared to non-selective channels like NaK.

Figure 6.11: The width of the SF depends on the ion configuration during K^+ conduction. a) Probability density of the distance between opposing carbonyl oxygen atoms of C479 (blue) and I480 (red) during K^+ conduction. Distances were measured for $t=[400;420]$ ns of the trajectory depicted in Figure 6.8 and smoothed using a Gaussian kernel density estimator. Maxima of the probability density are labeled (1-2) b) Snapshots with distances corresponding to labeled maxima 1 and 2. c-d) The same measurement as shown in a,b but measured for $t=[0;1000]$ ns of the Na^+ trajectory depicted in Figure 6.9.



6.4 FREE ENERGY CALCULATIONS

A common strategy to investigate the dynamics underlying ion channel conductance in proteinaceous pores is the sampling of a multidimensional PMF. This reveals possible low- and high energy states associated with a set of initially chosen CVs and allows to extract a minimal free energy pathway (MFEP) as most probable pathway through the free energy surface. To study ion conduction, a natural choice for CVs is the position of individual ions along the principal axis (z) of the channel. The movements of these ions (either K^+ or Na^+ in case of HCN channels) represent the most important degrees of freedom in the otherwise rather static system of the SF. Therefore, the PMF basically follows the trajectory of the inward current from the extracellular medium into the central cavity, out of the pore and into the cytosol.

In the open pore of the HCN4 channel, the SF alternates between two major states with one or two bound ions (Section 6.3). Additionally, a third ion can occupy the cavity below the SF. The present study investigates the energetics underlying ion conduction on two different sets of CVs (see Appendix C.3 for simulation details): the more simple case involves only the position of the two ions (z_1 and z_2) in the SF as CVs (Figure 6.12a). In this scenario, no third ion is present inside the cavity of the pore domain. The more complex case involves a third ion placed inside the central cavity (z_3). However, to reduce the complexity of the latter system, the position of the two lower ions were combined into a single CV ($z_{2,3}$) that represents the centroid of these ions (Figure 6.12b). This approach can be justified by the fact that ions move between states on distinct pathways with a limited set of stable configurations (see Section 6.3.1). Therefore, there is no ambiguity in the position of ions with a combined representation in the PMF and only little information is lost compared to the sampling of a 3-dimensional PMF while the combinatorial explosion is kept within acceptable bounds²³.

6.4.1 High Energy Barriers During K^+ Conduction

Figure 6.13 shows the 2D PMF of ion conduction in a system where z_1 and z_2 represent the positions of two K^+ ions (K^+/K^+ system). Configurations representing local minima of the PMF are shown next to the PMF and labeled according to the positions of the ions*. In general, MFEPs following the inward transition of K^+ are in good agreement with MD simulations carried out with an applied electric field (Section 6.3). During a transition from the vestibule (ves), through the SF and into the central cavity (cav), ions visit carbonyl oxygen planes p_{23} and p_{34} as well as canonical binding sites s_3 and s_4 . The conduction mechanism thereby follows a sequence of states labeled 1-5 that connect the two major minima with either two ions (state 2, $[p_{23}, s_4]$) or a single ion (state 5, $[p_{34}, cav]$) inside the pore. With a single ion bound to p_{34} (state 1, $[ves, p_{34}]$), a newly arriving ion can fit into the vestibule above the SF where it keeps its first hydration shell. When the newly arriving ion binds to p_{23} , it displaces the lower ion from the p_{34} plane

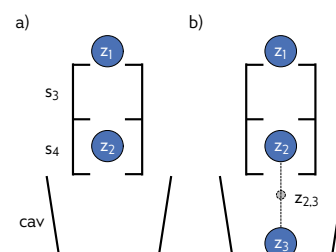


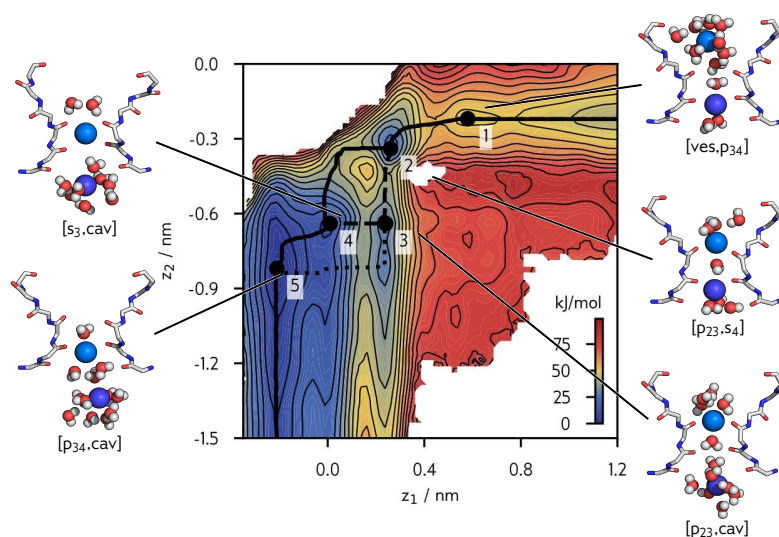
Figure 6.12: Comparison of two approaches to sample multi-ion PMFs in HCN4. a) Only the z -coordinate of two ions (z_1 and z_2) are considered as CVs. b) The system incorporates a third ion. The centroid of the lower two ions is used as second CV ($z_{2,3} = (z_2 + z_3)/2$).

²³ Egwolf and Roux (2010).

*i.e. $[ves, p_{34}]$ corresponds to a configuration of the SF where the upper ion is located in the vestibule and the lower ion is bound to p_{34} , see also Section 6.1.

towards s_4 (state 2, $[p_{23}, s_4]$). In this configuration, both ions are still partially solvated and can interact with water molecules from the vestibule and the central cavity, respectively. Following the MFEP (solid line), the lower ion then leaves s_4 into the central cavity (state 5, $[p_{23}, \text{cav}]$). Finally, the upper ion moves through the shallow minima in s_3 ($[s_3, \text{cav}]$) to p_{34} ($[p_{34}, \text{cav}]$), thus resetting the initial state with a single ion bound to the SF motif.

Figure 6.13: Free energy landscape of K^+ conduction involving two K^+ ions. The free energy is shown as function of the position of two ions z_1 and z_2 along the principal axis of the channel. The s_3 binding site is located at $z=0$ nm. Black solid and dashed lines represent possible paths through the 2D landscape. Local minima are labeled numerically (1-5) and corresponding snapshots of the SF are shown next to the plot.



Interesting to note is that the PMF allows the ions to explore several alternative pathways in addition to the MFEP: starting from state 2, $[p_{23}, s_4]$ ions can also move in concert between $[p_{23}, s_4]$ and $[p_{34}, \text{cav}]$ (dashed line between state 2&4, Figure 6.13) or the upper ion can hold its position while the ion in the cavity already starts leaving the pore (dotted line between state 3&5, Figure 6.13). Scrutiny of the data reported in Section 6.3.1 confirmed this assumption. Several simulations showed conduction events where ions either moved in concert (corresponding to the dashed line, Figure 6.14a) or where the upper ion follows movement of the lower ion with a delay of approximately 1 ns (corresponding to the solid line, Figure 6.14b). This confirms that slightly different mechanisms are indeed possible for K^+ conduction in HCN4. The exact mechanism therefore appears to be mainly driven by a high bias of ions to bind to p_{34} . This state can be reached via various pathways through the energy landscape.

Figure 6.15 shows a 1D projection of the MFEPs along the reaction coordinate λ . Here, $\lambda \in [0; 1]$ is a one-dimensional coordinate that connects the start and end state during ion movement through the two-dimensional PMF (Figure 6.13) and thus represents the progress of an ion conduction event. The paths show the energy barriers that have to be overcome when following one of the paths through the potential energy surface. Here, all paths require the K^+/K^+ system to overcome exceptionally high energy differences during ion conduction. To leave state 2, $[p_{23}, s_4]$, the system has to overcome an energy barrier of at least

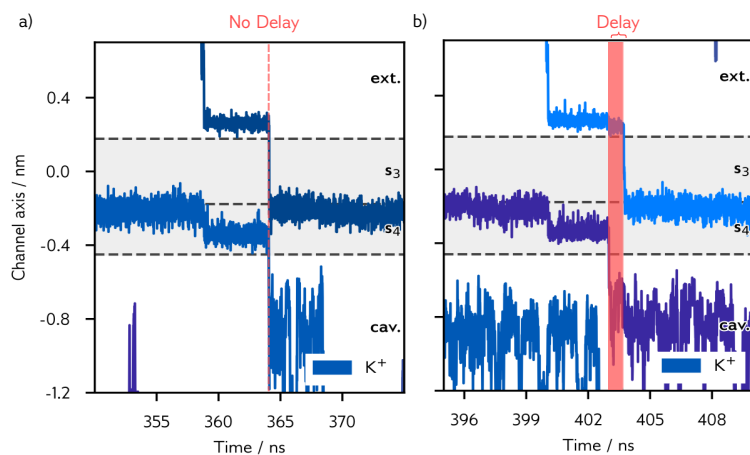


Figure 6.14: Ion trajectories for K^+ conduction under hyperpolarizing voltages. a) Ions move in concert with no observable delay. b) Movement of the upper ion is delayed by approximately 1 ns (red area).

$\Delta A_{2 \rightarrow 3}^\ddagger(K^+/K^+) \approx 19 \text{ kJ mol}^{-1}$ —more than 4 times higher than what has been observed for canonical K^+ channels such as KcsA²⁴. Furthermore, state 5, $[p_{34}, \text{cav}]$ and state 1, $[\text{ves}, p_{34}]$ are separated by an energy barrier of at least $\Delta A_{5 \rightarrow 1}^\ddagger(K^+/K^+) \approx 51 \text{ kJ mol}^{-1}$. Here, it is assumed that there are no other major barriers between these two states and that the system can move from state 5 to 1 across the unsampled region and periodic boundary between $\lambda=1$ and $\lambda=0$.

²⁴ Bernèche and Roux (2001); Fowler et al. (2013).

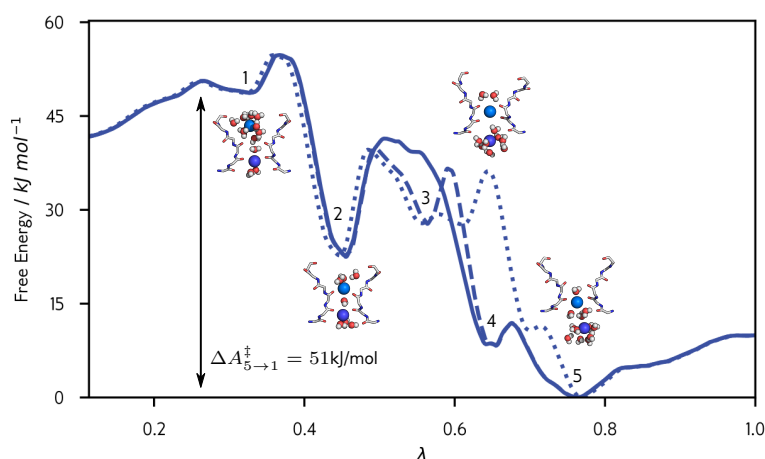


Figure 6.15: 1D projection of various paths through the free energy landscape of K^+ conduction along the reaction coordinate $\lambda \in [0; 1]$. The solid line represents the MFEP and dashed and dotted lines correspond to other thermodynamically possible paths. Minima of the MFEP are labeled according to Figure 6.13.

Transition state theory (TST) is a simple technique that can also be applied to biological systems to estimate rate constants from free energies and vice versa (Section 4.3)²⁵. Applied to ion conductance, TST can provide us with an upper estimate for the rate-limiting free energy barrier $\Delta A_{\text{max}}^\ddagger$ observed during ion conduction²⁶. Experimentally measured conductance in HCN channels is in the order of 1 to 2 pS (Table 6.2). For the lower end of the scale ($k=6.05 \times 10^5 \text{ s}^{-1}$), this corresponds to a rate constant of $6.05 \times 10^5 \text{ s}^{-1}$. Therefore, by assuming $\kappa = 1$ in Equation 4.13, the upper estimate for $\Delta A_{\text{max}}^\ddagger$ during K^+ conduction in HCN is approximately:

$$\Delta A_{\text{max}}^\ddagger = -RT \ln\left(\frac{6.05 \times 10^5 \text{ s}^{-1}}{6.46 \times 10^{12} \text{ s}^{-1}}\right) \approx 40 \text{ kJ mol}^{-1} \quad (6.1)$$

²⁵ Eyring (1935); Evans and Polanyi (1935); Salamon et al. (2015).

²⁶ V. B. Luzhkov and Åqvist (2001).

Table 6.2: Measured conductance in HCN channels and estimated rate constants at -100 mV. Rate constants were obtained from: ¹ DiFrancesco (1986), ² DiFrancesco and Mangoni (1994), ³ Dekker and Yellen (2006), ⁴ Thon, Schmauder, and Benndorf (2013).

Conductance / pS	k / s^{-1}
1.00^1	6.24×10^5
0.97^2	6.05×10^5
1.50^3	9.36×10^5
1.67^4	1.04×10^6

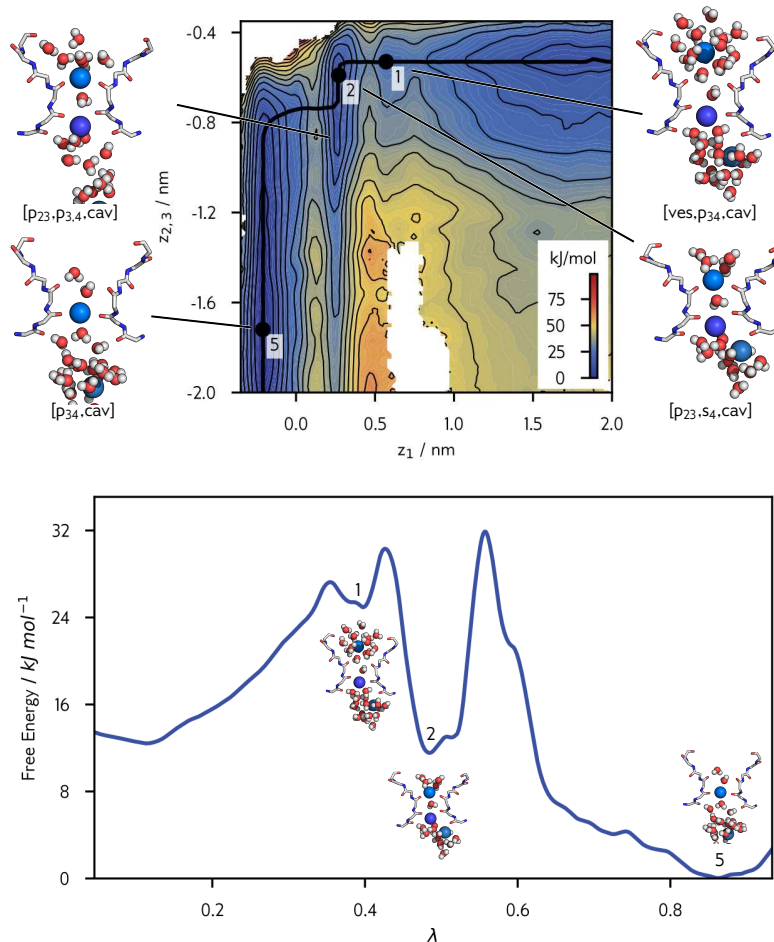
* i.e. the same index is assigned to [ves,p₃₄] in the K⁺/K⁺ system and [ves,p₃₄,cav] in the K⁺/K⁺/K⁺ system based on the approximate position of the upper two ions.

This calculated highest energy barrier in Figure 6.15 is much higher than this estimate ($\Delta A_{5 \rightarrow 1}^\ddagger \approx 51$ kJ mol⁻¹). This leads to the hypothesis that the third ion inside the cavity of the pore may play a crucial role in the process of ion conduction. This influence of a third ion could explain the high energetic difference between the two very similar states 5 and 1 as free energy gain from bringing an additional ion from the bulk solvent into the central cavity of the pore.

Therefore, a second PMF with an additional ion placed in the central cavity was calculated (K⁺/K⁺/K⁺ system, Figure 6.16a). Here, z_2 was replaced by the centroid of the lower two ions $z_{2,3}$ as CV (Figure 6.12). Also, only the MFEP will be considered for further discussion and minima of the PMFs with 3 ions were labeled in a way that makes them comparable to the K⁺/K⁺ system*.

The first important point to notice is that the two ions inside the SF follow the same overall mechanism observed for the 2-ion PMF with the exception that the minima corresponding to [s₃,cav] is missing: [ves,p₃₄,cav] → [p₂₃,s₄,cav] → [p₃₄,cav] (Figure 6.16a,b). However, free energy differences and energy barriers between the states differ signif-

Figure 6.16: a) Free energy landscape of K⁺ conduction involving three K⁺ ions. The free energy is shown as function of the position of the upper ion (z_1) and the centroid of the two lower ions ($z_{2,3}$) along the principal axis of the channel. The s₃ binding site is located at $z=0$ nm. The black solid line represent the MFEP through the 2D landscape. Local minima are labeled numerically (1-5) and corresponding snapshots of the SF are shown next to the plot. b) 1D projection of the MFEP through the free energy landscape in a) along the reaction coordinate $\lambda \in [0; 1]$. Minima of the MFEP are labeled according to a).



icantly between the two systems once two ions are bound to the SF: while the free energy barrier between state 1: $[\text{ves}, \text{p}_{34}, (\text{cav})]$ and state 2: $[\text{p}_{23}, \text{s}_4, (\text{cav})]$ is very similar ($\Delta\Delta A_{1\rightarrow 2}^\ddagger \approx -1 \text{ kJ mol}^{-1}$)*, the free energy gain is significantly lower for the system with three ions ($\Delta\Delta A_{2\rightarrow 5}^\ddagger \approx 13 \text{ kJ mol}^{-1}$, Table 6.3). The same is true for the actual conduction step where the lower ion leaves the SF and the upper ion moves from p_{23} to p_{34} (state 2: $[\text{p}_{23}, \text{s}_4, \text{cav}] \rightarrow$ state 4: $[\text{p}_{34}, \text{cav}]$). Again, the free energy barrier is very similar for both systems ($\Delta\Delta A_{1\rightarrow 2}^\ddagger \approx 2 \text{ kJ mol}^{-1}$), but the K^+/K^+ system has a higher free energy gain relative to state 1 than the $\text{K}^+/\text{K}^+/\text{K}^+$ system ($\Delta\Delta A_{2\rightarrow 5}^\ddagger \approx 11 \text{ kJ mol}^{-1}$). Finally, the unrealistically high energy barrier for the transition from $\lambda=1$ to $\lambda=0$ over the periodic boundary shrinks drastically in the $\text{K}^+/\text{K}^+/\text{K}^+$ system. Here, the barrier for the transition $5 \rightarrow 1$ is reduced by $\Delta\Delta A_{5\rightarrow 1}^\ddagger \approx -21 \text{ kJ mol}^{-1}$ to $\Delta A_{5\rightarrow 1}^\ddagger(\text{KKK}) \approx 30 \text{ kJ mol}^{-1}$. This value is much more compatible with the experimentally measured pS conductance as well as simulations with an applied electric field (Section 6.3)²⁷.

This finding highlights the importance of a third ion inside the central cavity for the conduction mechanism. Only the setup with three ions produces a PMF compatible with the experimentally determined conductance. Therefore, the following discussion will only refer to systems incorporating three ions in the PD.

Transition	Free Energy / kJ mol^{-1}	
	K^+/K^+	$\text{K}^+/\text{K}^+/\text{K}^+$
$\Delta A_{1\rightarrow 2}^\ddagger$	$+6.05 \pm 0.72$	$+4.95 \pm 0.33$
$\Delta A_{1\rightarrow 2}$	-26.12 ± 0.74	-13.44 ± 0.32
$\Delta A_{2\rightarrow 4}^\ddagger$	$+18.82 \pm 0.60$	-
$\Delta A_{2\rightarrow 4}$	-14.25 ± 0.45	-
$\Delta A_{4\rightarrow 5}^\ddagger$	$+3.40 \pm 0.14$	-
$\Delta A_{4\rightarrow 5}$	-8.26 ± 0.08	-
$\Delta A_{2\rightarrow 5}^\ddagger$	-	$+20.30 \pm 0.30$
$\Delta A_{2\rightarrow 5}$	-	-11.48 ± 0.18
$\Delta A_{5\rightarrow 1}^\ddagger$	$+50.55 \pm 0.37$	$+29.65 \pm 0.18$
$\Delta A_{5\rightarrow 1}$	$+51.46 \pm 0.30$	$+24.92 \pm 0.18$

In comparison with PMFs obtained from selective K^+ channels²⁸, it becomes apparent that energy minima in HCN are separated by exceptionally high energy barriers in both investigated systems. In previous works it has been discussed that energy barriers need to be in the range of ≤ 3 to 5 kJ mol^{-1} in order to support the nearly diffusion-limited conductance in K^+ channels²⁹. In HCN, both major transitions between states 2 and 5 and states 5 and 1 do not meet this criteria with free energy barriers of $\Delta A_{4\rightarrow 5}^\ddagger(\text{K}^+/\text{K}^+/\text{K}^+) \approx 20 \text{ kJ mol}^{-1}$ and $\Delta A_{4\rightarrow 5}^\ddagger(\text{K}^+/\text{K}^+) \approx 30 \text{ kJ mol}^{-1}$, respectively. With the finding of these high energy barriers, free energy simulations provide an explanation for the exceptionally low unitary conductance of HCN channels observed in experiments and also seen in MD simulations with applied electric field (Section 6.3): the exceptionally low unitary conductance of HCN channels is hence based on the fact that the system has to

$$*\Delta\Delta A = \Delta A(\text{K}^+/\text{K}^+/\text{K}^+) - \Delta A(\text{K}^+/\text{K}^+)$$

²⁷ DiFrancesco (1986); DiFrancesco and Mangoni (1994); Dekker and Yellen (2006); Thon, Schmauder, and Bendorf (2013); Saponaro et al. (2021).

Table 6.3: Calculated free energy differences between minima $A_{i\rightarrow j}$ and the height of energy barriers for corresponding transitions $A_{i\rightarrow j}^\ddagger$ in the K^+/K^+ system ($\Delta A(z_1, z_2)$) and corresponding transitions in the $\text{K}^+/\text{K}^+/\text{K}^+$ system ($\Delta A(z_1, z_2, z_3)$). The shown uncertainties are the result of 100 bayesian bootstrapping runs for the 2D PMF calculation.

²⁸ Bernèche and Roux (2001); Egwolf and Roux (2010); Fowler et al. (2013); Medovoy, Perozo, and Roux (2016); Wojtas-Niziurski et al. (2013).

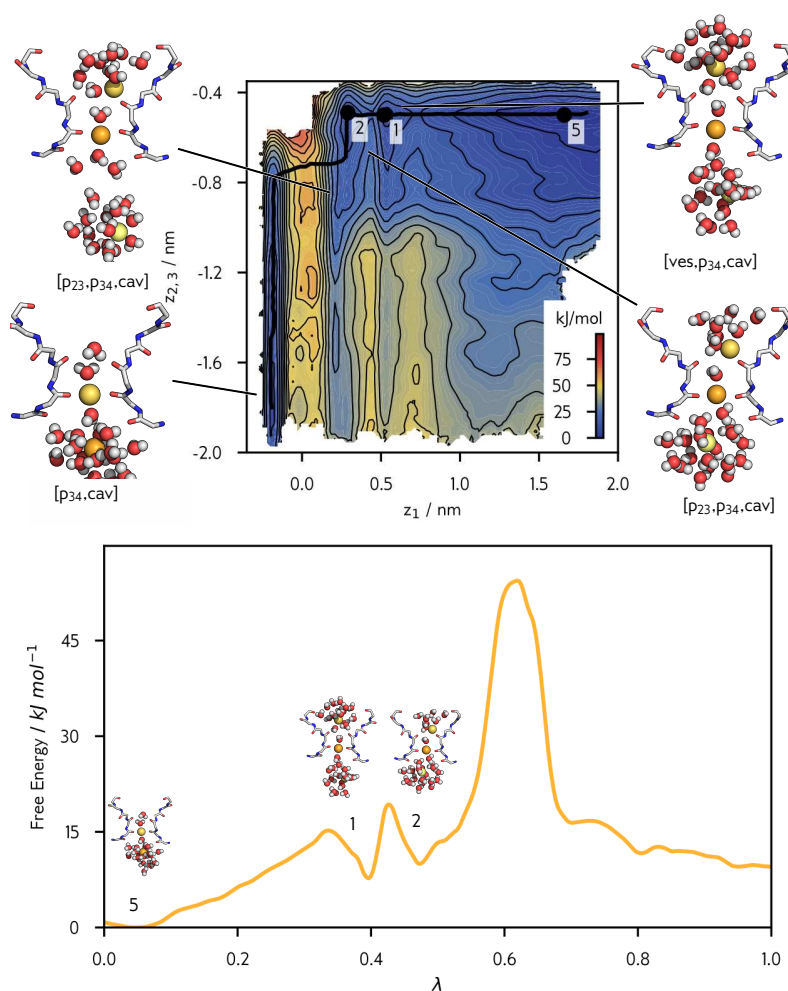
²⁹ Bernèche and Roux (2001); V. Luzhkov and Åqvist (2005); Fowler et al. (2013).

overcome much higher energy differences when conducting ions and is therefore slowed down kinetically (=high barriers) compared to related K^+ channels with a high(er) unitary conductance.

6.4.2 Reduced Conductance With Only Sodium

The free energy surface of Na^+ conduction ($Na^+/Na^+/Na^+$ system) follows a similar scheme to the one observed for the $K^+/K^+/K^+$ system (Figure 6.17a). The PMF has its minimum of potential energy with a single ion bound to p_{34} of the SF and the other two ions in the bulk solvent and central cavity [p_{34},cav]. With a Na^+ bound to p_{34} , a second Na^+ can potentially enter the vestibule (state 1, [ves,p_{34},cav]) and bind to p_{23} (state 2, [p_{23},p_{34},cav]). In contrast to the $K^+/K^+/K^+$ system, this does not immediately result in a displacement of the lower Na^+ into s_4 . Instead, binding of two Na^+ is also a valid configuration and resembles the general tendency of Na^+ to bind to carbonyl planes instead of oxygen cages in cation channels. Finally, the lower ion can leave the SF by moving through s_4 into the cavity while the upper ion replaces it in p_{34} (sequence: state 2, [p_{23},p_{34},cav]→state 5, [p_{34},cav]). Also in agreement with data from classical MD simulations (Section 6.3.2), Na^+ shows no

Figure 6.17: a) Free energy landscape of Na^+ conduction involving three Na^+ ions. The free energy is shown as function of the position of the upper ion (z_1) and the centroid of the two lower ions ($z_{2,3}$) along the principal axis of the channel. The s_3 binding site is located at $z=0$ nm. The solid line represents the MFEP through the 2D landscape. Local minima are labeled numerically (1-5) and corresponding snapshots of the SF are shown next to the plot. b) 1D projection of the MFEP through the free energy landscape in a) along the reaction coordinate $\lambda \in [0; 1]$. Minima of the MFEP are labeled according to a).



tendency to stay in s_3 in HCN₄ at all. This can be seen by the missing minimum at $z_1 = 0.0$ nm corresponding to state 4, [s_3, cav] in the K^+/K^+ system (cf. [Figure 6.13](#) and [Figure 6.17](#)).

Interestingly, the 1D projection of the MFEP of the $\text{Na}^+/\text{Na}^+/\text{Na}^+$ system reveals a high potential energy barrier between states 2 and 5* of $\Delta A_{2 \rightarrow 5}^\ddagger(\text{Na}^+/\text{Na}^+/\text{Na}^+) \approx 44 \text{ kJ mol}^{-1}$ ([Figure 6.17b](#) and [Table 6.4](#)). The corresponding rate for this transition—calculated via TST—is two orders of magnitude smaller than the corresponding rate from the biggest energy barrier in the $\text{K}^+/\text{K}^+/\text{K}^+$ system ($2.4 \times 10^5 \text{ s}^{-1}$ vs. $6.5 \times 10^7 \text{ s}^{-1}$). It can therefore be concluded that subsequent Na^+ conduction must be a rare event that is physiologically irrelevant for HCN₄ conductance. In fact, the free energy barrier for Na^+ conduction is so high that Na^+ can be considered as a weak channel-blocking agent that cannot be released from the SF by binding of another Na^+ . This assumption is also supported by experimental findings showing only limited or no Na^+ conductance in absence of K^+ in HCN channels³⁰.

6.4.3 Potassium Binding Facilitates Sodium Conduction

Free energy calculations of the $\text{Na}^+/\text{Na}^+/\text{Na}^+$ system successfully predict impaired conductance of HCN₄ in pure Na^+ solutions³¹. However, they do not explain how the SF becomes conductive for Na^+ in the presence of K^+ . In this context, MD simulations with an applied electronic field showed that Na^+ conduction is indeed possible if K^+ takes place in the conduction process ([Section 6.3.2](#)). Therefore, additional free energy profiles were sampled for systems where the approaching upper ion (z_1) and the ions already present in the PD (z_2, z_3) are different: in the $\text{Na}^+/\text{K}^+/\text{K}^+$ system, a Na^+ approaches an SF with bound K^+ and the $\text{K}^+/\text{Na}^+/\text{Na}^+$ system corresponds to the opposite case.

The PMF and its 1D projection of the MFEP for the $\text{Na}^+/\text{K}^+/\text{K}^+$ system ([Figure 6.18a,b](#)) looks strikingly similar to the $\text{Na}^+/\text{Na}^+/\text{Na}^+$ system: again, a high energy barrier ($\Delta A_{2 \rightarrow 5}^\ddagger(\text{Na}^+/\text{K}^+/\text{K}^+) \approx 34 \text{ kJ mol}^{-1}$, [Table D.1](#)) between state 2: [$p_{23}, p_{34}, \text{cav}$] and state 5: [p_{34}, cav] is present. It can therefore be reasoned, that the rate limiting factor for Na^+ conduction is related to the interaction of the upper Na^+ with the p_{23} plane; after all, the z_1 ion is the only constant between the two systems. However, this free energy barrier is significantly lower in the $\text{Na}^+/\text{K}^+/\text{K}^+$ system compared to the $\text{Na}^+/\text{Na}^+/\text{Na}^+$ system due to the replacement of the lower two Na^+ in the SF by K^+ ($\Delta \Delta A_{2 \rightarrow 5}^\ddagger \approx -10 \text{ kJ mol}^{-1}$). In contrast to the $\text{Na}^+/\text{Na}^+/\text{Na}^+$ system, the energy barrier of the $\text{K}^+/\text{Na}^+/\text{Na}^+$ system is in accordance with the upper threshold of $\Delta A_{max}^\ddagger \approx 40 \text{ kJ mol}^{-1}$ for an energy barrier during ion conduction as calculated via TST ([Section 6.4.1](#)). Therefore, while binding and transition of a newly arriving Na^+ to an SF with an already present Na^+ appears to be highly unlikely, Na^+ ions can more easily replace K^+ in the SF.

Table 6.4: Calculated free energy differences between minima $A_{i \rightarrow j}$ and the height of energy barriers for corresponding transitions $A_{i \rightarrow j}^\ddagger$ in the $\text{Na}^+/\text{Na}^+/\text{Na}^+$ system ($\Delta A(z_1, z_{2,3})$)

Transition	Free Energy / kJ mol^{-1}
$\Delta A_{1 \rightarrow 2}^\ddagger$	$+10.80 \pm 0.18$
$\Delta A_{1 \rightarrow 2}$	$+1.92 \pm 0.19$
$\Delta A_{2 \rightarrow 5}^\ddagger$	$+44.14 \pm 0.67$
$\Delta A_{2 \rightarrow 5}$	-10.07 ± 0.68
$\Delta A_{5 \rightarrow 1}^\ddagger$	$+15.15 \pm 0.10$
$\Delta A_{5 \rightarrow 1}$	$+8.15 \pm 0.11$

*In this case, state 5 was assigned close to $\lambda = 0$ instead of $\lambda = 1$. This choice has been made to follow the general pattern of assigning state 5 to the lowest energy state. The state where the lowest ion leaves the central pore is identical to the state with the upper ion inside the bulk due to the periodic nature of the system ($A(\lim_{\lambda \rightarrow 1}) \approx A(\lambda = 0)$).

³⁰ Lyashchenko and Tibbs (2008).

³¹ V. B. Luzhkov and Åqvist (2001).

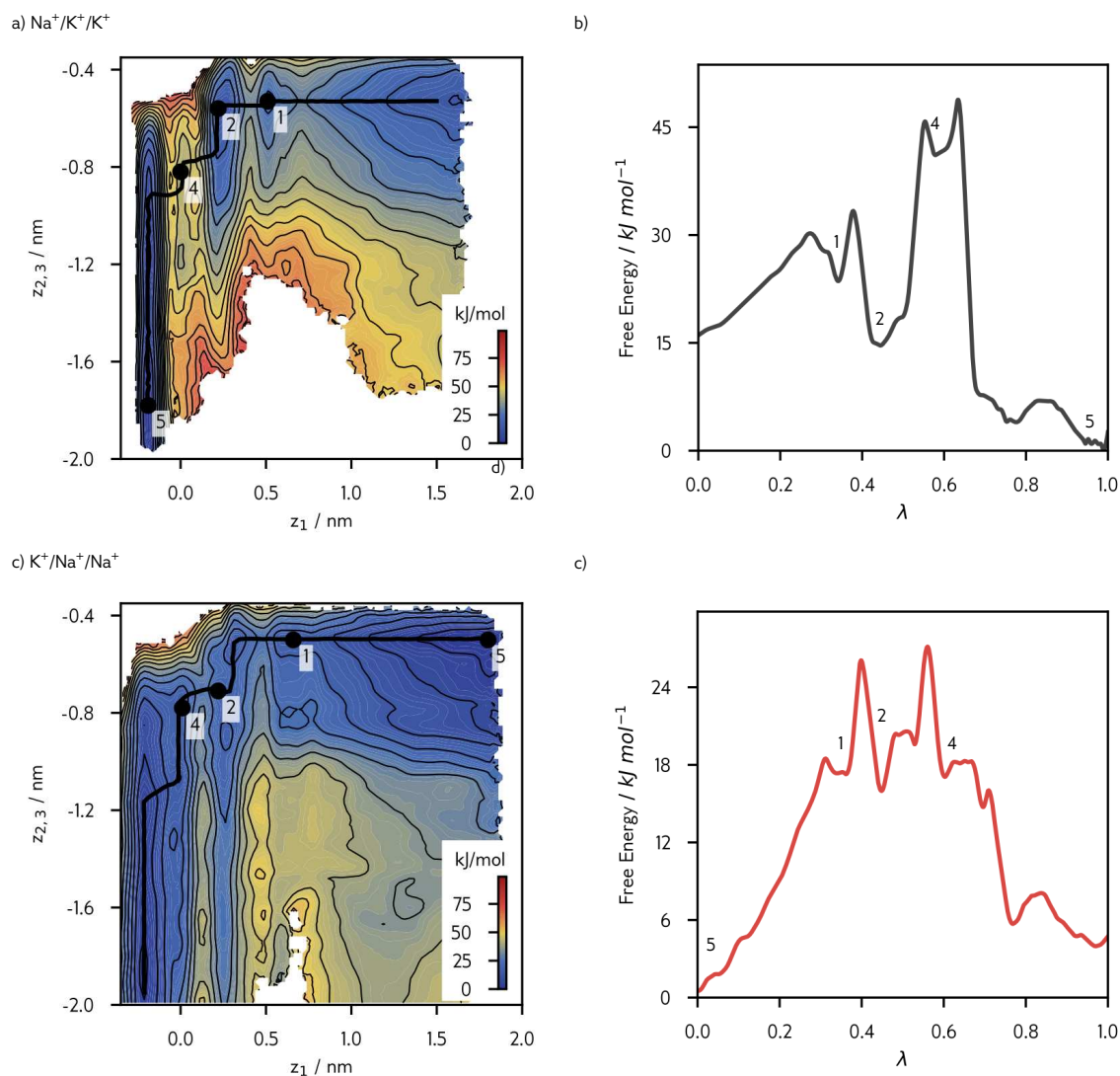


Figure 6.18: Free energy landscapes of ion conduction and corresponding 1D projections of the MFEP along the reaction coordinate $\lambda \in [0; 1]$. a-b) The $\text{Na}^+/\text{K}^+/\text{K}^+$ system shows the free energy profile for the approach of a Na^+ to the pore with with two K^+ ions. c-d) The $\text{K}^+/\text{Na}^+/\text{Na}^+$ system shows the opposite case where K^+ approaches a SF primed with Na^+ . The free energy is shown as function of the position of the upper ion (z_1) and the centroid of the two lower ions ($z_{2,3}$) along the principal axis of the channel. The s_3 binding site is located at $z=0$ nm. The solid line represents the MFEP through the 2D landscape. Local minima are labeled numerically (1-5).

Finally, Figure 6.18c,d show the opposite case: a K^+ approaches the SF with already bound sodium ($\text{K}^+/\text{Na}^+/\text{Na}^+$ system). Again, all free energy barriers are below the 40 kJ mol^{-1} mark and thus are in agreement with experimental results. Therefore, the presence of K^+ in the system facilitates both binding and unbinding of Na^+ from the SF of HCN4. This directly increases conductivity for sodium compared to the case where no K^+ is present.

In conclusion, this enables the SF to support consecutive conduction for K^+ , but Na^+ conduction events must be separated by at least one conducting K^+ which lowers observed free energy barriers. This in turn likely contributes to the observed weak selectivity of HCN channels compared to the non-selective NaK channel: K^+ can always conduct through the pore independent of its current state and thus has a higher probability to do so. In contrast, Na^+ can only conduct under specific circumstances (the presence of K^+ in the SF) which requires alternation of K^+ and Na^+ conduction.

6.5 ION PERMEATION STRICTLY FOLLOWS SOFT KNOCK-ON

For canonical K^+ channels, two different mechanisms have been proposed for K^+ ion conduction (see Section 2.4). In contrast, conduction events in HCN4 show water molecules co-permeating with K^+ as well as Na^+ ions in every observed conduction event and independent of starting conditions (Section 6.3 and Appendix D.3).

For a quantitative measurement of this observation, intercalation of water molecules between ions was monitored during umbrella simulations (Section 6.4). Figure 6.19 shows the probability of finding the given number of water molecules between two adjacent ions inside the SF dependent on the position of the upper ion (z_1).

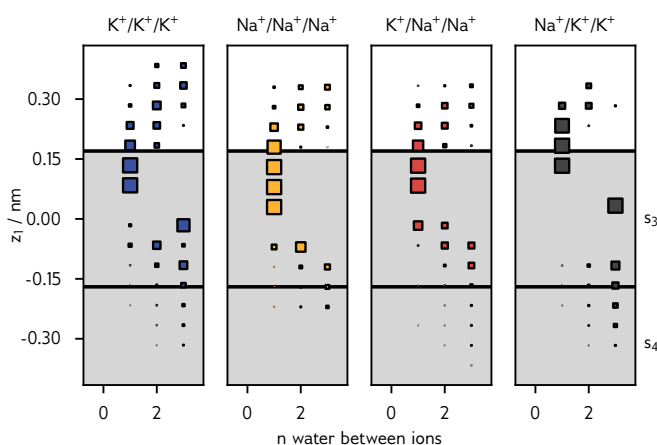


Figure 6.19: The number of water molecules between adjacent ions in the SF as function of the coordinate of z_1 in umbrella simulations with three ions inside the pore (Section 6.4, Appendix C.2.3). The volume of each square equals to the density calculated over all US runs along the given z coordinate. For clarity, the density is only shown for $n=[0;3]$ because higher n correspond to nonphysical configurations with ions far apart from each other (i.e. [ves,cav,(cav)]). From left to right: $K^+/K^+/K^+$ (blue), $Na^+/Na^+/Na^+$ (orange), $K^+/Na^+/Na^+$ (red), $Na^+/K^+/K^+$ (grey). The shaded area corresponds to binding sites s_3 and s_4 .

It can be seen that ions are always separated by at least one water molecule inside the SF (no density at $n=0$ independent of the position of z_1). For US, this is especially relevant because ion-water alternation was not enforced in these simulations and the system is also not biased due to the initial ion placement (some of the adaptive US runs started from an initial configuration with only a single ion in the SF and water was allowed to freely bind to, or leave it). Together with simulations with an applied electric field (Section 6.3), US simulations therefore suggest that ion permeation in HCN indeed strictly follows a soft knock-on mechanism and that hard knock-on permeation is not possible in HCN4. These data are hence in good agreement with the general prediction that an exclusion of water is functionally coupled to high ion selectivity and high conductance in K^+ channels since the opposite is the case for slowly conducting HCN channels³².

Worth mentioning here is also that simulations of HCN4 with co-conducting water did not show the occasional escape of water molecules which were squeezing past ions. Also configurations with more than one water molecule at individual binding sites were not observed. These kinds of events have been reported from simulations of canonical SFs that enforced soft knock-on in umbrella simulations³³.

³² Kopec et al. (2018).

³³ Fowler et al. (2013).

Part III

Final Remarks

CHAPTER 7

Conclusion

Many aspects of the molecular basis underlying ligand- and voltage-dependent gating, as well as conductance, in hyperpolarization-activated cyclic nucleotide-gated (HCN) channels are yet to be fully understood. This thesis employed various computational techniques such as molecular dynamics (MD) simulations, homology modeling and *in-silico* mutation studies to further our understanding of this unique channel species.

IN-SILICO MUTATIONAL STUDIES

Homology modeling and comparative MD simulations were used to study how mutation of two critical residues which influence channel functioning changes the channels structure and dynamics (Chapter 5). Three recently discovered and characterized missense mutations of a glycine residue located at the cytosolic gate of human HCN1 (HCN1_{G391S/C/D}) cause severe forms of infantile epilepsy. Electrophysiological characterization revealed shifts in the half-activation voltage for G391S/C. G391D, the variant that caused the most severe form of epilepsy, led to non-functional channels when expressed alone. In contrast, co-expression with HCN1_{wt} was able to recover conductance.¹ MD simulations presented in this work were able to give a molecular explanation for the observed electrophysiological properties: The introduction of negatively charged aspartate side chains in HCN1_{G391D} forces the channel open due to the increase space requirement as well as electrostatic repulsion between the closely spaced subunits. Subsequently, cations are complexed by one or several aspartates and thus block the channel from conducting ions (Section 5.2). Thereby, the observed molecular phenotype strongly depended on the number and arrangement of mutated side chains in the tetrameric protein: only channels with the mutation in at least two opposing subunits showed similar behavior to the fully mutated variant. If the mutation was introduced in neighboring subunits, wt-like behavior was observable. This finding explains how cells carrying the mutation heterozygously were still able to produce a fraction of functioning channels in patch-clamp experiments.

For another residue, F109 in HCN1, it could be shown that its side chain is stably inserted into a hydrophobic pocket that interconnects the cyclic-nucleotide binding-domain (CNBD), voltage sensor domain (VSD) and pore domain (PD). In patch-clamp experiments, gradual mutation of the corresponding amino acid in HCN2 (F151) to more hydrophilic and less bulky amino acids (HCN2_{F151W/M/V/A/E}) led to significant shifts of the half-activation voltage to more positive values². Here, computational mutation studies were able to show that these shifts

¹ Marini et al. (2018).

² Porro et al. (2019).

strongly correlate with increased intramolecular distances between residues forming the hydrophobic pocket. Furthermore, it could be shown that the loss of cAMP-dependence for HCN_{2F151E} was a result of a disruption of the hydrophobic pocket. In contrast to other tested mutations, the glutamate side chain rotates out of the pocket and thus completely disrupts the network of interconnections between domains. In both cases, comparative MD simulations were used to close the gap between experimental data from mutational characterization studies and structural information from Cryo-EM structures. By this, experimental results could be interpreted in a molecular context and conclusions could be drawn that were hardly obtainable from structural information of the wt structure alone (Section 5.3).

ION CONDUCTION

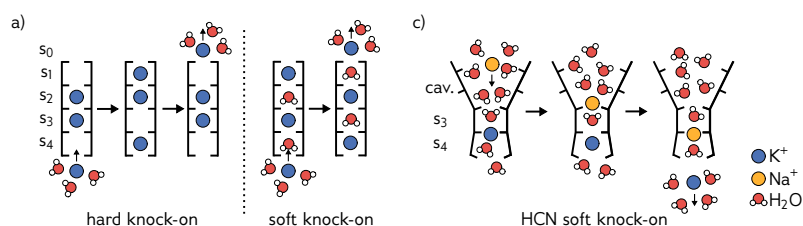
One of the key features of cation channels is their ability to discriminate between different ion species. For K⁺ channels, two competing mechanisms on how ions move through the selectivity filter (SF) have been proposed (Figure 7.1a): in the hard knock-on model, ions are in direct contact with no intercalating water. In contrast, the soft knock-on model predicts water co-permeation. In both models, K⁺ ions exclusively bind to cages made by eight carbonyl oxygens (s₁ to s₄)³. This thesis proposes an alternative conduction mechanism that is unique for HCN channels and explains the observed weak cation selectivity as well as low conductance compared to other K⁺ channels (Chapter 6). In MD simulations, the SF of the open HCN₄ shows itself to be very flexible in the orientation and distance between carbonyl oxygens of opposing subunits (Section 6.3.3). This allows the SF to adopt its conformation to the ions present in the SF and ultimately K⁺ ions can not only bind to oxygen cages, but also to the carbonyl planes between them (Section 6.3). The resulting HCN-specific soft knock-on mechanism is an alternation between two distinct states with either one or two ions bound to the SF (Figure 7.1b). Similar to the soft knock-on mechanism, water co-conducts with ions with a permeation ratio of exactly 1:1 (Section 6.3 and Section 6.5). This has previously been linked to low conductance in other channels and can therefore also contribute to the low conductance typical for HCN channels⁴.

³ i.e. Morais-Cabral, Zhou, and MacKinnon (2001); Zhou, Morais-Cabral, et al. (2001); Bernèche and Roux (2001); Köpfer et al. (2014); Kopec et al. (2018); Öster et al. (2019).

⁴ Kopec et al. (2018).

Finally, free energy landscape calculations revealed that states visited during conduction are separated by energy barriers that are incompatible with diffusion-limited conductance (Section 6.4). Therefore, this

Figure 7.1: Models of ion permeation. a) Proposed conduction models for selective K⁺ channels. In the hard knock-on model, ions permeate without water. The soft knock-on model predicts water co-permeation. K⁺ binds to carbonyl oxygen cages s₁-s₄. b) HCN-specific soft knock on mechanism: K⁺ and Na⁺ can bind to carbonyl oxygen planes as well as cages. Permeation strictly follows a soft knock on model with co-permeating water.



this thesis identifies the SF of HCN channels as the major contributor to low conductance in this channel species. Finally, free energy simulations were used to explain the observed low conductance for Na^+ in absence of K^+ by a high energy barrier that prevents Na^+ to be released from the SF once bound to a carbonyl plane ([Section 6.4.2](#) and [Section 6.4.3](#)).

To conclude, the proposed conduction mechanism can explain several features unique for HCN channels including low picoSiemens conductance and low ion selectivity with a preference for K^+ over Na^+ .

CHAPTER 8

References

- Abraham, M. J., Murtola, T., Schulz, R., Páll, S., Smith, J. C., Hess, B., et al. (2015)
[GROMACS: High Performance Molecular Simulations through Multi-Level Parallelism from Laptops to Supercomputers](#). *SoftwareX* 1, pp. 19–25. DOI: [10.1016/j.softx.2015.06.001](https://doi.org/10.1016/j.softx.2015.06.001) (cited on p. 96).
- Alam, A. and Jiang, Y. (2009a)
[High-Resolution Structure of the Open NaK Channel](#). *Nature Structural & Molecular Biology* 16.1, pp. 30–34. DOI: [10.1038/nsmb.1531](https://doi.org/10.1038/nsmb.1531) (cited on pp. 19, 42).
- Alam, A. and Jiang, Y. (2009b)
[Structural Analysis of Ion Selectivity in the NaK Channel](#). *Nature Structural & Molecular Biology* 16.1, pp. 35–41. DOI: [10.1038/nsmb.1537](https://doi.org/10.1038/nsmb.1537) (cited on p. 13).
- Alberts, B., Johnson, A., Lewis, J., Morgan, D., Raff, M., Roberts, K., et al. (2017)
 Molecular Biology of the Cell. 6th ed. Garland Science (cited on p. 10).
- Altomare, C., Bucchi, A., Camatini, E., Baruscotti, M., Viscomi, C., Moroni, A., et al. (2001)
[Integrated Allosteric Model of Voltage Gating of Hcn Channels](#). *The Journal of General Physiology* 117.6, pp. 519–532. DOI: [10.1085/jgp.117.6.519](https://doi.org/10.1085/jgp.117.6.519) (cited on p. 17).
- Andersson, A. E. V., Kasimova, M. A., and Delemotte, L. (2018)
[Exploring the Viral Channel KcvPBCV-1 Function via Computation](#). *The Journal of Membrane Biology* 251.3, pp. 419–430. DOI: [10.1007/s00232-018-0022-2](https://doi.org/10.1007/s00232-018-0022-2) (cited on pp. 45, 96).
- Armstrong, C. M. (1966)
 Time Course of TEA+-Induced Anomalous Rectification in Squid Giant Axons. *The Journal of General Physiology* 50.2, pp. 491–503 (cited on pp. 7, 12).
- Arnsten, A. F. (2011)
[Prefrontal Cortical Network Connections: Key Site of Vulnerability in Stress and Schizophrenia](#). *International Journal of Developmental Neuroscience* 29.3, pp. 215–223. DOI: [10.1016/j.ijdevneu.2011.02.006](https://doi.org/10.1016/j.ijdevneu.2011.02.006) (cited on p. 16).
- Ashcroft, F. M. (2006)
[From Molecule to Malady](#). *Nature* 440.7083, pp. 440–447. DOI: [10.1038/nature04707](https://doi.org/10.1038/nature04707) (cited on p. 33).
- Baker, E. N. and Hubbard, R. E. (1984)
[Hydrogen Bonding in Globular Proteins](#). *Progress in Biophysics and Molecular Biology* 44.2, pp. 97–179. DOI: [10.1016/0079-6107\(84\)90007-5](https://doi.org/10.1016/0079-6107(84)90007-5) (cited on pp. 35, 94).
- Baker, K. A., Tzitzilonis, C., Kwiatkowski, W., Choe, S., and Riek, R. (2007)
[Conformational Dynamics of the KcsA Potassium Channel Governs Gating Properties](#). *Nature Structural & Molecular Biology* 14.11, pp. 1089–1095. DOI: [10.1038/nsmb1311](https://doi.org/10.1038/nsmb1311) (cited on p. 49).
- Baruscotti, M., Bottelli, G., Milanesi, R., DiFrancesco, J. C., and DiFrancesco, D. (2010)
[HCN-Related Channelopathies](#). *Pflügers Archiv - European Journal of Physiology* 460.2, pp. 405–415. DOI: [10.1007/s00424-010-0810-8](https://doi.org/10.1007/s00424-010-0810-8) (cited on p. 33).
- Bauer, D. (2020)
[An Efficient Weighted Histogram Analysis Implementation Written in Rust](#). Version 1.0.0. Zenodo. DOI: [10.5281/zenodo.4075070](https://doi.org/10.5281/zenodo.4075070) (cited on p. 98).

- Benarroch, E. E. (2013)
[HCN Channels: Function and Clinical Implications](#). *Neurology* 80.3, pp. 304–310. DOI: [10.1212/WNL.0b013e31827dec42](#) (cited on p. 15).
- Bernèche, S. and Roux, B. (2001)
[Energetics of Ion Conduction through the K⁺ Channel](#). *Nature* 414.6859, pp. 73–77. DOI: [10.1038/35102067](#) (cited on pp. 12, 26, 53, 55, 64).
- Bernstein, J. (1902)
[Untersuchungen Zur Thermodynamik Der Bioelektrischen Ströme](#). *Pflüger Archiv für die Gesamte Physiologie des Menschen und der Thiere* 92.10–12, pp. 521–562. DOI: [10.1007/bf01790181](#) (cited on p. 7).
- Bernsteiner, H., Zangerl-Plessl, E.-M., Chen, X., and Stary-Weinzinger, A. (2019)
[Conduction through a Narrow Inward-Rectifier K⁺ Channel Pore](#). *Journal of General Physiology* 151.10, pp. 1231–1246. DOI: [10.1085/jgp.201912359](#) (cited on p. 25).
- Best, R. B. and Hummer, G. (2009)
[Optimized Molecular Dynamics Force Fields Applied to the Helix–Coil Transition of Polypeptides](#). *The Journal of Physical Chemistry B* 113.26, pp. 9004–9015. DOI: [10.1021/jp901540t](#) (cited on p. 96).
- Biel, M. (2002)
[Cardiac HCN Channels Structure, Function, and Modulation](#). *Trends in Cardiovascular Medicine* 12.5, pp. 206–213. DOI: [10.1016/S1050-1738\(02\)00162-7](#) (cited on pp. 15–17).
- Biggin, P. C., Roosild, T., and Choe, S. (2000)
[Potassium Channel Structure: Domain by Domain](#). *Current Opinion in Structural Biology* 10.4, pp. 456–461. DOI: [10.1016/S0959-440X\(00\)00114-7](#) (cited on p. 9).
- Bucchi, A., Tognati, A., Milanese, R., Baruscotti, M., and DiFrancesco, D. (2006)
[Properties of Ivabradine-Induced Block of HCN₁ and HCN₄ Pacemaker Channels](#). *The Journal of Physiology* 572.2, pp. 335–346. DOI: [10.1113/jphysiol.2005.100776](#) (cited on p. 44).
- Bucchi, A., Baruscotti, M., Nardini, M., Barbuti, A., Micheloni, S., Bolognesi, M., et al. (2013)
[Identification of the Molecular Site of Ivabradine Binding to HCN₄ Channels](#). *PLoS One* 8.1, e53132. DOI: [10.1371/journal.pone.0053132](#) (cited on p. 44).
- Bussi, G., Donadio, D., and Parrinello, M. (2007)
[Canonical Sampling through Velocity Rescaling](#). *The Journal of Chemical Physics* 126.1, p. 014101. DOI: [10.1063/1.2408420](#) (cited on pp. 24, 94, 96).
- Chaplan, S. R., Guo, H.-Q., Lee, D. H., Luo, L., Liu, C., Kuei, C., et al. (2003)
[Neuronal Hyperpolarization-Activated Pacemaker Channels Drive Neuropathic Pain](#). *The Journal of Neuroscience: The Official Journal of the Society for Neuroscience* 23.4, pp. 1169–1178. DOI: [10.1523/JNEUROSCI.23-04-01169.2003](#) (cited on p. 16).
- Chaudhary, K. K. and Mishra, N. (2016)
 A Review on Molecular Docking: Novel Tool for Drug Discovery. *Databases* 3.4, p. 1029 (cited on p. 28).
- Choe, S. (2002)
[Potassium Channel Structures](#). *Nature Reviews Neuroscience* 3.2, pp. 115–121. DOI: [10.1038/nrn727](#) (cited on p. 9).
- Clausius, R. (1870)
[Ueber einen auf die Wärme anwendbaren mechanischen Satz](#). *Annalen der Physik und Chemie* 217.9, pp. 124–130. DOI: [10.1002/andp.18702170911](#) (cited on p. 24).

- Concepcion, F. A., Khan, M. N., Ju Wang, J.-D., Wei, A. D., Ojemann, J. G., Ko, A. L., et al. (2021)
[HCN Channel Phosphorylation Sites Mapped by Mass Spectrometry in Human Epilepsy Patients and in an Animal Model of Temporal Lobe Epilepsy](#). *Neuroscience* 460, pp. 13–30. DOI: [10.1016/j.neuroscience.2021.01.038](#) (cited on p. 33).
- Cordero-Morales, J. F., Cuello, L. G., and Perozo, E. (2006)
[Voltage-Dependent Gating at the KcsA Selectivity Filter](#). *Nature Structural & Molecular Biology* 13.4, pp. 319–322. DOI: [10.1038/nsmb1070](#) (cited on p. 9).
- Cordomí, A., Caltabiano, G., and Pardo, L. (2012)
[Membrane Protein Simulations Using AMBER Force Field and Berger Lipid Parameters](#). *Journal of Chemical Theory and Computation* 8.3, pp. 948–958. DOI: [10.1021/ct200491c](#) (cited on pp. 24, 96).
- Cramer, C. J. (2004)
 Essentials of Computational Chemistry: Theories and Models. 2nd ed. Chichester, West Sussex, England ; Hoboken, NJ: Wiley. 618 pp. (cited on p. 23).
- Craven, K. B. and Zagotta, W. N. (2006)
[CNG and HCN Channels: Two Peas, One Pod](#). *Annual Review of Physiology* 68.1, pp. 375–401. DOI: [10.1146/annurev.physiol.68.040104.134728](#) (cited on p. 16).
- Darve, E. and Pohorille, A. (2001)
[Calculating Free Energies Using Average Force](#). *The Journal of Chemical Physics* 115.20, pp. 9169–9183. DOI: [10.1063/1.1410978](#) (cited on p. 26).
- De Jong, D. H., Singh, G., Bennett, W. F. D., Arnarez, C., Wassenaar, T. A., Schäfer, L. V., et al. (2013)
[Improved Parameters for the Martini Coarse-Grained Protein Force Field](#). *Journal of Chemical Theory and Computation* 9.1, pp. 687–697. DOI: [10.1021/ct300646g](#) (cited on p. 25).
- De Miguel, E. and Jackson, G. (2006)
[The Nature of the Calculation of the Pressure in Molecular Simulations of Continuous Models from Volume Perturbations](#). *The Journal of Chemical Physics* 125.16, p. 164109. DOI: [10.1063/1.2363381](#) (cited on p. 24).
- Dekker, J. P. and Yellen, G. (2006)
[Cooperative Gating between Single HCN Pacemaker Channels](#). *The Journal of General Physiology* 128.5, pp. 561–567. DOI: [10.1085/jgp.200609599](#) (cited on pp. 54, 55).
- Delemotte, L., Kasimova, M. A., Klein, M. L., Tarek, M., and Carnevale, V. (2015)
[Free-Energy Landscape of Ion-Channel Voltage-Sensor-Domain Activation](#). *Proceedings of the National Academy of Sciences* 112.1, pp. 124–129. DOI: [10.1073/pnas.1416959112](#) (cited on p. 29).
- Derebe, M. G., Sauer, D. B., Zeng, W., Alam, A., Shi, N., and Jiang, Y. (2011)
[Tuning the Ion Selectivity of Tetrameric Cation Channels by Changing the Number of Ion Binding Sites](#). *Proceedings of the National Academy of Sciences* 108.2, pp. 598–602. DOI: [10.1073/pnas.1013636108](#) (cited on pp. 13, 49).
- DiFrancesco, D. (1993)
[Pacemaker Mechanisms in Cardiac Tissue](#). *Annual Review of Physiology* 55.1, pp. 455–472. DOI: [10.1146/annurev.ph.55.030193.002323](#) (cited on p. 16).
- DiFrancesco, D. (1986–10)
[Characterization of Single Pacemaker Channels in Cardiac Sino-Atrial Node Cells](#). *Nature* 324.6096, pp. 470–473. DOI: [10.1038/324470a0](#) (cited on pp. 45, 54, 55).

- DiFrancesco, D. and Mangoni, M. (1994)
 Modulation of Single Hyperpolarization-Activated Channels (i(f)) by cAMP in the Rabbit Sino-Atrial Node. *The Journal of Physiology* 474.3, pp. 473–482. DOI: 10.1113/jphysiol.1994.sp020038 (cited on pp. 54, 55).
- DiFrancesco, D. and Tortora, P. (1991)
 Direct Activation of Cardiac Pacemaker Channels by Intracellular Cyclic AMP. *Nature* 351.6322 (6322), pp. 145–147. DOI: 10.1038/351145a0 (cited on p. 17).
- Dini, L., Del Lungo, M., Resta, F., Melchiorre, M., Spinelli, V., Di Cesare Mannelli, L., et al. (2018)
 Selective Blockade of HCN1/HCN2 Channels as a Potential Pharmacological Strategy Against Pain. *Frontiers in Pharmacology* 9, p. 1252. DOI: 10.3389/fphar.2018.01252 (cited on p. 16).
- Doyle, D. A., Cabral, J. M., Pfuetzner, R. A., Kuo, A., Gulbis, J. M., Cohen, S. L., et al. (1998)
 The Structure of the Potassium Channel: Molecular Basis of K⁺ Conduction and Selectivity. *Science* 280.5360, pp. 69–77. DOI: 10.1126/science.280.5360.69 (cited on pp. 7, 12, 41, 49).
- Eastwood, M. P., Stafford, K. A., Lippert, R. A., Jensen, M. Ø., Maragakis, P., Predescu, C., et al. (2010)
 Equipartition and the Calculation of Temperature in Biomolecular Simulations. *Journal of Chemical Theory and Computation* 6.7, pp. 2045–2058. DOI: 10.1021/ct9002916 (cited on p. 24).
- Egwolf, B. and Roux, B. (2010)
 Ion Selectivity of the KcsA Channel: A Perspective from Multi-Ion Free Energy Landscapes. *Journal of Molecular Biology* 401.5, pp. 831–842. DOI: 10.1016/j.jmb.2010.07.006 (cited on pp. 26, 41, 49, 51, 55).
- Essmann, U., Perera, L., Berkowitz, M. L., Darden, T., Lee, H., and Pedersen, L. G. (1995)
 A Smooth Particle Mesh Ewald Method. *The Journal of Chemical Physics* 103.19, pp. 8577–8593. DOI: 10.1063/1.470117 (cited on pp. 23, 94, 96).
- Evans, M. G. and Polanyi, M. (1935)
 Some Applications of the Transition State Method to the Calculation of Reaction Velocities, Especially in Solution. *Transactions of the Faraday Society* 31, p. 875. DOI: 10.1039/TF9353100875 (cited on pp. 29, 53).
- Eyring, H. (1935)
 The Activated Complex in Chemical Reactions. *The Journal of Chemical Physics* 3.2, pp. 107–115. DOI: 10.1063/1.1749604 (cited on pp. 29, 53).
- Fan, C., Sukomon, N., Flood, E., Rheinberger, J., Allen, T. W., and Nimigean, C. M. (2020)
 Ball-and-Chain Inactivation in a Calcium-Gated Potassium Channel. *Nature* 580.7802 (7802), pp. 288–293. DOI: 10.1038/s41586-020-2116-0 (cited on p. 11).
- Feenstra, K. A., Hess, B., and Berendsen, H. J. C. (1999)
 Improving Efficiency of Large Time-Scale Molecular Dynamics Simulations of Hydrogen-Rich Systems. *Journal of Computational Chemistry* 20.8, pp. 786–798. DOI: 10.1002/(SICI)1096-987X(199906)20:8<786::AID-JCC5>3.0.CO;2-B (cited on p. 96).
- Fenwick, R. B., Esteban-Martín, S., and Salvatella, X. (2011)
 Understanding Biomolecular Motion, Recognition, and Allostery by Use of Conformational Ensembles. *European Biophysics Journal* 40.12, pp. 1339–1355. DOI: 10.1007/s00249-011-0754-8 (cited on p. 28).

- Fiser, A., Do, R. K. G., and Šali, A. (2000)
[Modeling of Loops in Protein Structures](#). *Protein Science* 9.9, pp. 1753–1773. DOI: 2019040412534100024 (cited on p. 93).
- Fowler, P. W., Abad, E., Beckstein, O., and Sansom, M. S. P. (2013)
[Energetics of Multi-Ion Conduction Pathways in Potassium Ion Channels](#). *Journal of Chemical Theory and Computation* 9.11, pp. 5176–5189. DOI: 10.1021/ct4005933 (cited on pp. 12, 26, 53, 55, 59).
- Frenkel, D. and Smit, B. (1996)
 Understanding Molecular Simulation: From Algorithms to Applications. Vol. 1. London: Academic Press (cited on p. 28).
- Gandhi, C. S. and Isacoff, E. Y. (2002)
[Molecular Models of Voltage Sensing](#). *The Journal of General Physiology* 120.4, pp. 455–463. DOI: 10.1085/jgp.20028678 (cited on p. 10).
- Gauss, R., Seifert, R., and Kaupp, U. B. (1998)
[Molecular Identification of a Hyperpolarization-Activated Channel in Sea Urchin Sperm](#). *Nature* 393.6685, pp. 583–587. DOI: 10.1038/31248 (cited on pp. 17, 41, 48).
- Gazzarrini, S., Kang, M., Abenavoli, A., Romani, G., Olivari, C., Gaslini, D., et al. (2009)
[Chlorella Virus ATCV-1 Encodes a Functional Potassium Channel of 82 Amino Acids](#). *The Biochemical Journal* 420.2, pp. 295–303. DOI: 10.1042/BJ20090095 (cited on p. 9).
- González, M. A. (2011)
[Force Fields and Molecular Dynamics Simulations](#). *Collection SFN* 12, pp. 169–200. DOI: 10.1051/sfn/201112009 (cited on p. 27).
- Gowers, R. J., Linke, M., Barnoud, J., Reddy, T. J. E., Melo, M. N., Seyler, S. L., et al. (2016)
 “MDAnalysis: A Python Package for the Rapid Analysis of Molecular Dynamics Simulations”. *Proceedings of the 15th Python in Science Conference*. DOI: 10.25080/Majora-629e541a-00e (cited on p. 94).
- Gray, T. M. and Matthews, B. W. (1984)
[Intrahelical Hydrogen Bonding of Serine, Threonine and Cysteine Residues within Alpha-Helices and Its Relevance to Membrane-Bound Proteins](#). *Journal of Molecular Biology* 175.1, pp. 75–81. DOI: 10.1016/0022-2836(84)90446-7 (cited on p. 35).
- Grossfield, A. (2003)
 “WHAM - The Weighted Histogram Analysis Method” (cited on p. 27).
- Gumbart, J., Khalili-Araghi, F., Sotomayor, M., and Roux, B. (2012)
[Constant Electric Field Simulations of the Membrane Potential Illustrated with Simple Systems](#). *Biochimica et Biophysica Acta - Biomembranes* 1818.2, pp. 294–302. DOI: 10.1016/j.bbamem.2011.09.030 (cited on p. 25).
- Han, Y., Lyman, K. A., Foote, K. M., and Chetkovich, D. M. (2020)
[The Structure and Function of TRIP8b, an Auxiliary Subunit of Hyperpolarization-Activated Cyclic-Nucleotide Gated Channels](#). *Channels* 14.1, pp. 110–122. DOI: 10.1080/19336950.2020.1740501 (cited on p. 17).
- Hand, L. N. and Finch, J. D. (1998)
 Analytical Mechanics. 1st ed. Cambridge University Press (cited on p. 21).

- Hänggi, P., Talkner, P., and Borkovec, M. (1990)
[Reaction-Rate Theory: Fifty Years after Kramers](#). *Reviews of Modern Physics* 62.2, pp. 251–341. DOI: 10.1103/RevModPhys.62.251 (cited on p. 29).
- Hanwell, M. D., Curtis, D. E., Lonie, D. C., Vandermeersch, T., Zurek, E., and Hutchison, G. R. (2012)
[Avogadro: An Advanced Semantic Chemical Editor, Visualization, and Analysis Platform](#). *Journal of Cheminformatics* 4.1, p. 17. DOI: 10.1186/1758-2946-4-17 (cited on p. 95).
- Hart, K., Foloppe, N., Baker, C. M., Denning, E. J., Nilsson, L., and MacKerell, A. D. (2012)
[Optimization of the CHARMM Additive Force Field for DNA: Improved Treatment of the BI/BII Conformational Equilibrium](#). *Journal of Chemical Theory and Computation* 8.1, pp. 348–362. DOI: 10.1021/ct200723y (cited on p. 24).
- Hauf, K., Barsch, L., Bauer, D., Buchert, R., Armbruster, A., Frauenfeld, L., et al. (2020)
[GlyT1 Encephalopathy: Characterization of Presumably Disease Causing GlyT1 Mutations](#). *Neurochemistry International* 139, p. 104813. DOI: 10.1016/j.neuint.2020.104813 (cited on p. 33).
- Heer, F. T., Posson, D. J., Wojtas-Niziuski, W., Nimigean, C. M., and Bernèche, S. (2017)
[Mechanism of Activation at the Selectivity Filter of the KcsA K⁺ Channel](#). *eLife* 6, e25844. DOI: 10.7554/eLife.25844 (cited on p. 49).
- Henkelman, G. and Jónsson, H. (2000)
[Improved Tangent Estimate in the Nudged Elastic Band Method for Finding Minimum Energy Paths and Saddle Points](#). *The Journal of Chemical Physics* 113.22, pp. 9978–9985. DOI: 10.1063/1.1323224 (cited on p. 98).
- Hess, B., Bekker, H., Berendsen, H. J. C., and Fraaije, J. G. E. M. (1997)
[LINCS: A Linear Constraint Solver for Molecular Simulations](#). *Journal of Computational Chemistry* 18.12, pp. 1463–1472. DOI: 10.1002/(SICI)1096-987X(199709)18:12<1463::AID-JCC4>3.0.CO;2-H (cited on pp. 94, 96).
- Hockney, R. W., Goel, S., and Eastwood, J. W. (1974)
[Quiet High-Resolution Computer Models of a Plasma](#). *Journal of Computational Physics* 14.2, pp. 148–158. DOI: 10.1016/0021-9991(74)90010-2 (cited on p. 21).
- Hodgkin, A. L. and Huxley, A. F. (1952)
[A Quantitative Description of Membrane Current and Its Application to Conduction and Excitation in Nerve](#). *The Journal of Physiology* 117.4, pp. 500–544. DOI: 10.1113/jphysiol.1952.sp004764 (cited on p. 7).
- Högberg, C.-J., Nikitin, A. M., and Lyubartsev, A. P. (2008)
[Modification of the CHARMM Force Field for DMPC Lipid Bilayer](#). *Journal of Computational Chemistry* 29.14, pp. 2359–2369. DOI: 10.1002/jcc.20974 (cited on p. 24).
- Hu, L., Santoro, B., Saponaro, A., Liu, H., Moroni, A., and Siegelbaum, S. (2013)
[Binding of the Auxiliary Subunit TRIP8b to HCN Channels Shifts the Mode of Action of cAMP](#). *The Journal of General Physiology* 142.6, pp. 599–612. DOI: 10.1085/jgp.201311013 (cited on p. 17).
- Huang, J. and MacKerell, A. D. (2013)
[CHARMM36 All-Atom Additive Protein Force Field: Validation Based on Comparison to NMR Data](#). *Journal of Computational Chemistry* 34.25, pp. 2135–2145. DOI: 10.1002/jcc.23354 (cited on pp. 24, 93).
- Ishii, T. M., Takano, M., Xie, L. H., Noma, A., and Ohmori, H. (1999)
[Molecular Characterization of the Hyperpolarization-Activated Cation Channel in Rabbit Heart](#)

- Sinoatrial Node. *The Journal of Biological Chemistry* 274.18, pp. 12835–12839. DOI: [10.1074/jbc.274.18.12835](https://doi.org/10.1074/jbc.274.18.12835) (cited on p. 17).
- Jensen, M. Ø., Jogini, V., Borhani, D. W., Leffler, A. E., Dror, R. O., and Shaw, D. E. (2012)
[Mechanism of Voltage Gating in Potassium Channels](#). *Science* 336.6078, pp. 229–233. DOI: [10.1126/science.1216533](https://doi.org/10.1126/science.1216533) (cited on p. 25).
- Jensen, M. Ø., Borhani, D. W., Lindorff-Larsen, K., Maragakis, P., Jogini, V., Eastwood, M. P., et al. (2010)
[Principles of Conduction and Hydrophobic Gating in K⁺ Channels](#). *Proceedings of the National Academy of Sciences* 107.13, pp. 5833–5838. DOI: [10.1073/pnas.0911691107](https://doi.org/10.1073/pnas.0911691107) (cited on p. 25).
- Jing, Z., Liu, C., Cheng, S. Y., Qi, R., Walker, B. D., Piquemal, J.-P., et al. (2019)
[Polarizable Force Fields for Biomolecular Simulations: Recent Advances and Applications](#). *Annual Review of Biophysics* 48.1, pp. 371–394. DOI: [10.1146/annurev-biophys-070317-033349](https://doi.org/10.1146/annurev-biophys-070317-033349) (cited on p. 27).
- Jo, S., Kim, T., Iyer, V. G., and Im, W. (2008)
[CHARMM-GUI: A Web-Based Graphical User Interface for CHARMM](#). *Journal of Computational Chemistry* 29.11, pp. 1859–1865. DOI: [10.1002/jcc.20945](https://doi.org/10.1002/jcc.20945) (cited on pp. 25, 95).
- Johnson, J. P. and Zagotta, W. N. (2005)
[The Carboxyl-Terminal Region of Cyclic Nucleotide-Modulated Channels Is a Gating Ring, Not a Permeation Path](#). *Proceedings of the National Academy of Sciences* 102.8, pp. 2742–2747. DOI: [10.1073/pnas.0408323102](https://doi.org/10.1073/pnas.0408323102) (cited on p. 45).
- Jones, J. E. (1924)
[On the Determination of Molecular Fields. —II. From the Equation of State of a Gas](#). *Proceedings of the Royal Society of London. Series A* 106.738, pp. 463–477. DOI: [10.1098/rspa.1924.0082](https://doi.org/10.1098/rspa.1924.0082) (cited on p. 23).
- Jorgensen, W. L., Chandrasekhar, J., Madura, J. D., Impey, R. W., and Klein, M. L. (1983)
[Comparison of Simple Potential Functions for Simulating Liquid Water](#). *The Journal of Chemical Physics* 79.2, pp. 926–935. DOI: [10.1063/1.445869](https://doi.org/10.1063/1.445869) (cited on pp. 93, 96).
- Jou, C. J., Arrington, C. B., Barnett, S., Shen, J., Cho, S., Sheng, X., et al. (2017)
[A Functional Assay for Sick Sinus Syndrome Genetic Variants](#). *Cellular Physiology and Biochemistry* 42.5, pp. 2021–2029. DOI: [10.1159/000479897](https://doi.org/10.1159/000479897) (cited on p. 16).
- Joung, I. S. and Cheatham, T. E. (2008)
[Determination of Alkali and Halide Monovalent Ion Parameters for Use in Explicitly Solvated Biomolecular Simulations](#). *The Journal of Physical Chemistry B* 112.30, pp. 9020–9041. DOI: [10.1021/jp8001614](https://doi.org/10.1021/jp8001614) (cited on p. 96).
- Karplus, M. and Petsko, G. A. (1990)
[Molecular Dynamics Simulations in Biology](#). *Nature* 347.6294 (6294), pp. 631–639. DOI: [10.1038/347631a0](https://doi.org/10.1038/347631a0) (cited on p. 21).
- Kasimova, M. A., Tewari, D., Cowgill, J., Carrasquel Ursulaez, W., Lin, J., Delemotte, L., et al. (2019)
[Helix Breaking Transition in the S4 of HCN Channel Is Critical for Hyperpolarization-Dependent Gating](#). *SSRN Electronic Journal*. DOI: [10.2139/ssrn.3468492](https://doi.org/10.2139/ssrn.3468492) (cited on p. 18).
- Kästner, J. (2011)
[Umbrella Sampling: Umbrella Sampling](#). *Wiley Interdisciplinary Reviews: Computational Molecular Science* 1.6, pp. 932–942. DOI: [10.1002/wcms.66](https://doi.org/10.1002/wcms.66) (cited on p. 27).

- Kim, J.-B. (2014)
[Channelopathies](#). *Korean Journal of Pediatrics* 57.1, pp. 1–18. DOI: [10.3345/kjp.2014.57.1.1](#) (cited on p. 33).
- Klauda, J. B., Venable, R. M., Freites, J. A., O'Connor, J. W., Tobias, D. J., Mondragon-Ramirez, C., et al. (2010)
[Update of the CHARMM All-Atom Additive Force Field for Lipids: Validation on Six Lipid Types](#). *The Journal of Physical Chemistry B* 114.23, pp. 7830–7843. DOI: [10.1021/jp101759q](#) (cited on p. 24).
- Kleywegt, G. J. and Jones, T. A. (1994)
[Detection, Delineation, Measurement and Display of Cavities in Macromolecular Structures](#). *Acta Crystallographica Section D Biological Crystallography* 50.2, pp. 178–185. DOI: [10.1107/S0907444993011333](#) (cited on pp. 93, 95).
- Knoll, A. T., Halladay, L. R., Holmes, A., and Levitt, P. (2016)
[Quantitative Trait Loci and a Novel Genetic Candidate for Fear Learning](#). *Journal of Neuroscience* 36.23, pp. 6258–6268. DOI: [10.1523/JNEUROSCI.0177-16.2016](#) (cited on p. 16).
- Kopec, W., Köpfer, D. A., Vickery, O. N., Bondarenko, A. S., Jansen, T. L., de Groot, B. L., et al. (2018)
[Direct Knock-on of Desolvated Ions Governs Strict Ion Selectivity in K⁺ channels](#). *Nature Chemistry* 10.8, pp. 813–820. DOI: [10.1038/s41557-018-0105-9](#) (cited on pp. 12, 25, 49, 59, 64, 96).
- Köpfer, D. A., Song, C., Gruene, T., Sheldrick, G. M., Zachariae, U., and de Groot, B. L. (2014)
[Ion Permeation in K⁺ Channels Occurs by Direct Coulomb Knock-On](#). *Science* 346.6207, pp. 352–355. DOI: [10.1126/science.1254840](#) (cited on pp. 12, 25, 45, 64, 96).
- Kuang, Q., Purhonen, P., and Hebert, H. (2015)
[Structure of Potassium Channels](#). *Cellular and Molecular Life Sciences* 72, pp. 3677–3693. DOI: [10.1007/s00018-015-1948-5](#) (cited on p. 8).
- Kumar, S., Rosenberg, J. M., Bouzida, D., Swendsen, R. H., and Kollman, P. A. (1992)
[THE Weighted Histogram Analysis Method for Free-Energy Calculations on Biomolecules. I. The Method](#). *Journal of Computational Chemistry* 13.8, pp. 1011–1021. DOI: [10.1002/jcc.540130812](#) (cited on pp. 27, 98).
- Kunzmann, P. and Hamacher, K. (2018)
[Biotite: A Unifying Open Source Computational Biology Framework in Python](#). *BMC Bioinformatics* 19.1, p. 346. DOI: [10.1186/s12859-018-2367-z](#) (cited on pp. 94, 96).
- Kutzner, C., Grubmüller, H., de Groot, B. L., Zachariae, U., de Groot, B. L., and Zachariae, U. (2011)
[Computational Electrophysiology: The Molecular Dynamics of Ion Channel Permeation and Selectivity in Atomistic Detail](#). *Biophysical Journal* 101.4, pp. 809–817. DOI: [10.1016/j.bpj.2011.06.010](#) (cited on p. 25).
- Kutzner, C., Köpfer, D. A., Machtens, J.-P., de Groot, B. L., Song, C., and Zachariae, U. (2016)
[Insights into the Function of Ion Channels by Computational Electrophysiology Simulations](#). *Biochimica et Biophysica Acta (BBA) - Biomembranes* 1858.7, pp. 1741–1752. DOI: [10.1016/j.bbame.2016.02.006](#) (cited on p. 25).
- Laidler, K. J. and King, M. C. (1983)
[Development of Transition-State Theory](#). *The Journal of Physical Chemistry* 87.15, pp. 2657–2664. DOI: [10.1021/j100238a002](#) (cited on p. 29).

- Laio, A. and Parrinello, M. (2002)
[Escaping Free-Energy Minima](#). *Proceedings of the National Academy of Sciences* 99.20, pp. 12562–12566. DOI: [10.1073/pnas.202427399](#) (cited on p. 26).
- Laish-Farkash, A., Brass, D., Marek-Yagel, D., Pras, E., Dascal, N., Antzelevitch, C., et al. (2010)
[A NOVEL MUTATION IN THE HCN₄ GENE CAUSES SYMPTOMATIC SINUS BRADYCARDIA IN MO-ROCCAN JEWS](#). *Journal of Cardiovascular Electrophysiology* 21.12, pp. 1365–1372. DOI: [10.1111/j.1540-8167.2010.01844.x](#) (cited on p. 16).
- Lam, Y. L., Zeng, W., Derebe, M. G., and Jiang, Y. (2015)
[Structural Implications of Weak Ca²⁺ Block in Drosophila Cyclic Nucleotide-Gated Channels](#). *Journal of General Physiology* 146.3, pp. 255–263. DOI: [10.1085/jgp.201511431](#) (cited on p. 13).
- Larkin, M. A., Blackshields, G., Brown, N. P., Chenna, R., McGettigan, P. A., McWilliam, H., et al. (2007)
[Clustal W and Clustal X Version 2.0](#). *Bioinformatics* 23.21, pp. 2947–2948. DOI: [10.1093/bioinformatics/btm404](#) (cited on p. 91).
- Leach, A. R. (2001)
 Molecular Modeling: Principles and Applications. 2nd ed. Pearson Education (cited on p. 28).
- Lee, C.-H. and MacKinnon, R. (2017)
[Structures of the Human HCN₁ Hyperpolarization-Activated Channel](#). *Cell* 168.1-2, 111–120.e11. DOI: [10.1016/j.cell.2016.12.023](#) (cited on pp. 7, 8, 11, 13, 18, 41, 93).
- Lee, C.-H. and MacKinnon, R. (2019)
[Voltage Sensor Movements during Hyperpolarization in the HCN Channel](#). *Cell* 179.7. DOI: [10.1016/j.cell.2019.11.006](#) (cited on p. 18).
- LeMasurier, M., Heginbotham, L., and Miller, C. (2001)
[KcsA: It's a Potassium Channel](#). *The Journal of General Physiology* 118.3, pp. 303–314. DOI: [10.1085/jgp.118.3.303](#) (cited on p. 12).
- Lemkul, J. A., Huang, J., Roux, B., and Mackerell, A. D. (2016)
[An Empirical Polarizable Force Field Based on the Classical Drude Oscillator Model: Development History and Recent Applications](#). *Chemical Reviews* 116.9, pp. 4983–5013. DOI: [10.1021/acs.chemrev.5b00505](#) (cited on p. 27).
- Li, J., Ostmeier, J., Cuello, L. G., Perozo, E., and Roux, B. (2018)
[Rapid Constriction of the Selectivity Filter Underlies C-Type Inactivation in the KcsA Potassium Channel](#). *The Journal of General Physiology* 150.10, pp. 1408–1420. DOI: [10.1085/jgp.201812082](#) (cited on p. 49).
- Li, Q., Wanderling, S., Paduch, M., Medovoy, D., Singharoy, A., McGreevy, R., et al. (2014)
[Structural Mechanism of Voltage-Dependent Gating in an Isolated Voltage-Sensing Domain](#). *Nature Structural & Molecular Biology* 21.3 (3), pp. 244–252. DOI: [10.1038/nsmb.2768](#) (cited on p. 11).
- Li, S., Yang, F., Sun, D., Zhang, Y., Zhang, M., Liu, S., et al. (2020)
[Cryo-EM Structure of the Hyperpolarization-Activated Inwardly Rectifying Potassium Channel KAT₁ from Arabidopsis](#). *Cell Research* 30.11 (11), pp. 1049–1052. DOI: [10.1038/s41422-020-00407-3](#) (cited on pp. 7, 11).
- Lindahl, Abraham, Hess, and van der Spoel (2020)
[GROMACS 2019.6 Manual](#). *Zenodo*. DOI: [10.5281/zenodo.3685925](#) (cited on pp. 21, 23, 24).

- Lindorff-Larsen, K., Piana, S., Palmo, K., Maragakis, P., Klepeis, J. L., Dror, R. O., et al. (2010)
[Improved Side-Chain Torsion Potentials for the Amber ff99SB Protein Force Field](#). *Proteins* 78.8, pp. 1950–1958. DOI: [10.1002/prot.22711](#) (cited on pp. 24, 96).
- Long, S. B., Tao, X., Campbell, E. B., and MacKinnon, R. (2007)
[Atomic Structure of a Voltage-Dependent K⁺ Channel in a Lipid Membrane-like Environment](#). *Nature* 450.7168 (7168), pp. 376–382. DOI: [10.1038/nature06265](#) (cited on p. 43).
- Ludwig, A., Zong, X., Jeglitsch, M., Hofmann, F., and Biel, M. (1998)
[A Family of Hyperpolarization-Activated Mammalian Cation Channels](#). *Nature* 393.6685, pp. 587–591. DOI: [10.1038/31255](#) (cited on pp. 15, 17, 41, 48).
- Luzhkov, V. and Åqvist, J. (2005)
[Ions and Blockers in Potassium Channels: Insights from Free Energy Simulations](#). *Biochimica et Biophysica Acta (BBA) - Proteins and Proteomics* 1747.1, pp. 109–120. DOI: [10.1016/j.bbapap.2004.10.006](#) (cited on p. 55).
- Luzhkov, V. B. and Åqvist, J. (2001)
[K⁺/Na⁺ Selectivity of the KcsA Potassium Channel from Microscopic Free Energy Perturbation Calculations](#). *Biochimica et Biophysica Acta - Protein Structure and Molecular Enzymology* 1548.2, pp. 194–202. DOI: [10.1016/S0167-4838\(01\)00213-8](#) (cited on pp. 29, 53, 57).
- Lyashchenko, A. K. and Tibbs, G. R. (2008)
[Ion Binding in the Open HCN Pacemaker Channel Pore: Fast Mechanisms to Shape "Slow" Channels](#). *The Journal of General Physiology* 131.3, pp. 227–243. DOI: [10.1085/jgp.200709868](#) (cited on pp. 17, 47, 57).
- Maffeo, C., Bhattacharya, S., Yoo, J., Wells, D., and Aksimentiev, A. (2012)
[Modeling and Simulation of Ion Channels](#). *Chemical Reviews* 112.12, pp. 6250–6284. DOI: [10.1021/cr3002609](#) (cited on pp. 24, 25).
- Marcus, Y. (1994)
[A Simple Empirical Model Describing the Thermodynamics of Hydration of Ions of Widely Varying Charges, Sizes, and Shapes](#). *Biophysical Chemistry* 51.2–3, pp. 111–127. DOI: [10.1016/0301-4622\(94\)00051-4](#) (cited on p. 48).
- Marini, C., Porro, A., Rastetter, A., Dalle, C., Rivolta, I., Bauer, D., et al. (2018)
[HCN1 Mutation Spectrum: From Neonatal Epileptic Encephalopathy to Benign Generalized Epilepsy and Beyond](#). *Brain* 141.11, pp. 3160–3178. DOI: [10.1093/brain/awy263](#) (cited on pp. 16, 33–35, 38, 63).
- Marrink, S. J., Risselada, H. J., Yefimov, S., Tieleman, D. P., de Vries, A. H., de Vries†, A. H., et al. (2007)
[The MARTINI Force Field: Coarse Grained Model for Biomolecular Simulations](#). *Journal of Physical Chemistry B* 111.27, pp. 7812–7824. DOI: [10.1021/JP071097F](#) (cited on p. 25).
- Martín-García, F., Papaleo, E., Gomez-Puertas, P., Boomsma, W., and Lindorff-Larsen, K. (2015)
[Comparing Molecular Dynamics Force Fields in the Essential Subspace](#). *PLoS One* 10.3, pp. 1–16. DOI: [10.1371/journal.pone.0121114](#) (cited on p. 27).
- McCormick, D. A. and Bal, T. (1997)
[Sleep and Arousal: Thalamocortical Mechanisms](#). *Annual Review of Neuroscience* 20.1, pp. 185–215. DOI: [10.1146/annurev.neuro.20.1.185](#) (cited on p. 15).

- McTague, A. and Cross, J. H. (2013)
[Treatment of Epileptic Encephalopathies](#). *CNS drugs* 27.3, pp. 175–184. DOI: 10.1007/s40263-013-0041-6 (cited on p. 34).
- Medovoy, D., Perozo, E., and Roux, B. (2016)
[Multi-Ion Free Energy Landscapes Underscore the Microscopic Mechanism of Ion Selectivity in the KcsA Channel](#). *Biochimica et Biophysica Acta - Biomembranes*. New Approaches for Bridging Computation and Experiment on Membrane Proteins 1858 (7, Part B), pp. 1722–1732. DOI: 10.1016/j.bbamem.2016.02.019 (cited on pp. 26, 55).
- Melchiorre, M., Del Lungo, M., Guandalini, L., Martini, E., Dei, S., Manetti, D., et al. (2010)
[Design, Synthesis, and Preliminary Biological Evaluation of New Isoform-Selective f-Current Blockers](#). *Journal of Medicinal Chemistry* 53.18, pp. 6773–6777. DOI: 10.1021/jm1006758 (cited on p. 16).
- Michaud-Agrawal, N., Denning, E. J., Woolf, T. B., and Beckstein, O. (2011)
[MDAnalysis: A Toolkit for the Analysis of Molecular Dynamics Simulations](#). *Journal of Computational Chemistry* 32.10, pp. 2319–2327. DOI: 10.1002/jcc.21787 (cited on p. 94).
- Miller, E. B., Murphy, R. B., Sindhikara, D., Borrelli, K. W., Grisewood, M. J., Ranalli, F., et al. (2021)
[Reliable and Accurate Solution to the Induced Fit Docking Problem for Protein–Ligand Binding](#). *Journal of Chemical Theory and Computation* 17.4, pp. 2630–2639. DOI: 10.1021/acs.jctc.1c00136 (cited on p. 28).
- Mironenko, A., Zachariae, U., de Groot, B. L., and Kopec, W. (2021)
[The Persistent Question of Potassium Channel Permeation Mechanisms](#). *Journal of Molecular Biology* 433.17, p. 167002. DOI: 10.1016/j.jmb.2021.167002 (cited on p. 49).
- Mistriák, P., Pfeifer, A., and Biel, M. (2006)
[The Enhancement of HCN Channel Instantaneous Current Facilitated by Slow Deactivation Is Regulated by Intracellular Chloride Concentration](#). *Pflügers Archiv - European Journal of Physiology* 452.6, pp. 718–727. DOI: 10.1007/s00424-006-0095-0 (cited on p. 17).
- Moldenhauer, H., Díaz-Franulic, I., González-Nilo, F., and Naranjo, D. (2016)
[Effective Pore Size and Radius of Capture for K⁺ Ions in K-Channels](#). *Scientific Reports* 6.1, p. 19893. DOI: 10.1038/srep19893 (cited on pp. 35, 36, 42).
- Monteggia, L. M., Eisch, A. J., Tang, M. D., Kaczmarek, L. K., and Nestler, E. J. (2000)
[Cloning and Localization of the Hyperpolarization-Activated Cyclic Nucleotide-Gated Channel Family in Rat Brain](#). *Molecular Brain Research* 81.1-2, pp. 129–139. DOI: 10.1016/S0169-328X(00)00155-8 (cited on p. 15).
- Monticelli, L., Kandasamy, S. K., Periole, X., Larson, R. G., Tieleman, D. P., and Marrink, S. J. (2008)
[The MARTINI Coarse-Grained Force Field: Extension to Proteins](#). *Journal of Chemical Theory and Computation* 4.5, pp. 819–834. DOI: 10.1021/ct700324x (cited on p. 25).
- Monticelli, L. and Tieleman, D. P. (2013)
[Force Fields for Classical Molecular Dynamics](#). *Methods in Molecular Biology* 924, pp. 197–213. DOI: 10.1007/978-1-62703-017-5_8 (cited on pp. 22, 23, 27).
- Moosmang, S., Stieber, J., Zong, X., Biel, M., Hofmann, F., and Ludwig, A. (2001)
[Cellular Expression and Functional Characterization of Four Hyperpolarization-Activated Pacemaker Channels in Cardiac and Neuronal Tissues](#). *European Journal of Biochemistry* 268.6, pp. 1646–1652. DOI: 10.1046/j.1432-1327.2001.02036.x (cited on p. 15).

- Morais-Cabral, J. H., Zhou, Y., and MacKinnon, R. (2001)
[Energetic Optimization of Ion Conduction Rate by the K⁺ Selectivity Filter](#). *Nature* 414.6859, pp. 37–42. DOI: 10.1038/35102000 (cited on pp. 12, 64).
- Moroni, A., Barbuti, A., Altomare, C., Viscomi, C., Morgan, J., Baruscotti, M., et al. (2000)
[Kinetic and Ionic Properties of the Human HCN₂ Pacemaker Channel](#). *Pflügers Archiv - European Journal of Physiology* 439.5, pp. 618–626. DOI: 10.1007/s004249900225 (cited on pp. 17, 41, 48).
- Morris, G. M., Goodsell, D. S., Halliday, R. S., Huey, R., Hart, W. E., Belew, R. K., et al. (1998)
[Automated Docking Using a Lamarckian Genetic Algorithm and an Empirical Binding Free Energy Function](#). *Journal of Computational Chemistry* 19.14, pp. 1639–1662. DOI: 10.1002/(SICI)1096-987X(19981115)19:14<1639::AID-JCC10>3.0.CO;2-B (cited on p. 28).
- Morris, G. M., Huey, R., Lindstrom, W., Sanner, M. F., Belew, R. K., Goodsell, D. S., et al. (2009)
[AutoDock4 and AutoDockTools4: Automated Docking with Selective Receptor Flexibility](#). *Journal of Computational Chemistry* 30.16, pp. 2785–2791. DOI: 10.1002/jcc.21256 (cited on pp. 28, 95).
- Nava, C., Dalle, C., Rastetter, A., Striano, P., De Kovel, C. G., Nabbout, R., et al. (2014)
[De Novo Mutations in HCN1 Cause Early Infantile Epileptic Encephalopathy](#). *Nature Genetics* 46.6, pp. 640–645. DOI: 10.1038/ng.2952 (cited on p. 16).
- Neher, E. and Sakmann, B. (1976)
[Single-Channel Currents Recorded from Membrane of Denervated Frog Muscle Fibres](#). *Nature* 260.5554, pp. 799–802. DOI: 10.1038/260799a0 (cited on p. 7).
- Nernst, W. (1889)
[Die Elektromotorische Wirksamkeit Der Jonen](#). *Zeitschrift für Physikalische Chemie* 4U.1, pp. 129–181. DOI: 10.1515/zpch-1889-0412 (cited on p. 7).
- Nof, E., Luria, D., Brass, D., Marek, D., Lahat, H., Reznik-Wolf, H., et al. (2007)
[Point Mutation in the HCN₄ Cardiac Ion Channel Pore Affecting Synthesis, Trafficking, and Functional Expression Is Associated with Familial Asymptomatic Sinus Bradycardia](#). *Circulation* 116.5, pp. 463–470. DOI: 10.1161/CIRCULATIONAHA.107.706887 (cited on p. 16).
- Noskov, S. Y. and Roux, B. (2006)
[Ion Selectivity in Potassium Channels](#). *Biophysical Chemistry* 124.3, pp. 279–291. DOI: 10.1016/j.bpc.2006.05.033 (cited on p. 13).
- Noskov, S. Y., Bernèche, S., and Roux, B. (2004)
[Control of Ion Selectivity in Potassium Channels by Electrostatic and Dynamic Properties of Carbonyl Ligands](#). *Nature* 431.7010 (7010), pp. 830–834. DOI: 10.1038/nature02943 (cited on p. 13).
- Olsson, M. H. M., Søndergaard, C. R., Rostkowski, M., and Jensen, J. H. (2011)
[PROPKA₃: Consistent Treatment of Internal and Surface Residues in Empirical pK_a Predictions](#). *Journal of Chemical Theory and Computation* 7.2, pp. 525–537. DOI: 10.1021/ct100578z (cited on p. 93).
- Öster, C., Hendriks, K., Kopec, W., Chevelkov, V., Shi, C., Michl, D., et al. (2019)
[The Conduction Pathway of Potassium Channels Is Water Free under Physiological Conditions](#). *Science Advances* 5.7, eaaw6756. DOI: 10.1126/sciadv.aaw6756 (cited on pp. 12, 64).
- Pagadala, N. S., Syed, K., and Tuszynski, J. (2017)
[Software for Molecular Docking: A Review](#). *Biophysical reviews* 9.2, pp. 91–102. DOI: 10.1007/s12551-016-0247-1 (cited on p. 28).

- Papazian, D. M., Schwarz, T. L., Tempel, B. L., Jan, Y. N., and Jan, L. Y. (1987)
[Cloning of Genomic and Complementary DNA from Shaker, a Putative Potassium Channel Gene from *Drosophila*](#). *Science* 237.4816, pp. 749–53. DOI: 10.1126/science.2441470 (cited on p. 7).
- Parrinello, M. and Rahman, A. (1981)
[Polymorphic Transitions in Single Crystals: A New Molecular Dynamics Method](#). *Journal of Applied Physics* 52.12, p. 7182. DOI: 10.1063/1.328693 (cited on pp. 94, 96).
- Parsegian, V. A. (1975)
[Ion-Membrane Interactions as Structural Forces](#). *Annals of the New York Academy of Sciences* 264.1, pp. 161–171. DOI: 10.1111/j.1749-6632.1975.tb31481.x (cited on p. 7).
- Poolos, N. P. (2012)
 “Hyperpolarization-Activated Cyclic Nucleotide-Gated (HCN) Ion Channelopathy in Epilepsy”. *Jasper’s Basic Mechanisms of the Epilepsies*. 4th ed. Bethesda: National Center for Biotechnology Information (cited on p. 15).
- Porro, A., Saponaro, A., Gasparri, F., Bauer, D., Gross, C., Pisoni, M., et al. (2019)
[The HCN Domain Couples Voltage Gating and cAMP Response in Hyperpolarization-Activated Cyclic Nucleotide-Gated Channels](#). *eLife* 8, e49672. DOI: 10.7554/eLife.49672 (cited on pp. 18, 34, 38, 63).
- Prasad, S., Mobley, D. L., Braun, E., Mayes, H. B., Monroe, J. I., Zuckerman, D. M., et al. (2018)
[Best Practices for Foundations in Molecular Simulations \[Article vi.0\]](#). *Living Journal of Computational Molecular Science* 1.1, pp. 1–28. DOI: 10.33011/livecoms.1.1.5957 (cited on p. 21).
- Prins, S., Langron, E., Hastings, C., Hill, E. J., Stefan, A. C., Griffin, L. D., et al. (2020)
[Fluorescence Assay for Simultaneous Quantification of CFTR Ion-Channel Function and Plasma Membrane Proximity](#). *Journal of Biological Chemistry* 295.49, pp. 16529–16544. DOI: 10.1074/jbc.RA120.014061 (cited on p. 33).
- Pronk, S., Páll, S., Schulz, R., Larsson, P., Bjelkmar, P., Apostolov, R., et al. (2013)
[GROMACS 4.5: A High-Throughput and Highly Parallel Open Source Molecular Simulation Toolkit](#). *Bioinformatics* 29.7, pp. 845–854. DOI: 10.1093/bioinformatics/btt055 (cited on p. 93).
- Ramentol, R., Perez, M. E., and Larsson, P. (2021)
[A Second S4 Movement Opens Hyperpolarization-Activated HCN Channels](#). *Biophysical Journal* 120.3, 244a. DOI: 10.1016/j.bpj.2020.11.1597 (cited on p. 18).
- Ramirez, J. M. and Richter, D. W. (1996)
[The Neuronal Mechanisms of Respiratory Rhythm Generation](#). *Current Opinion in Neurobiology* 6.6, pp. 817–825. DOI: 10.1016/s0959-4388(96)80033-x (cited on p. 15).
- Rappe, A. K., Casewit, C. J., Colwell, K. S., Goddard, W. A., and Skiff, W. M. (1992)
[UFF, a Full Periodic Table Force Field for Molecular Mechanics and Molecular Dynamics Simulations](#). *Journal of the American Chemical Society* 114.25, pp. 10024–10035. DOI: 10.1021/ja00051a040 (cited on p. 95).
- Resta, F., Micheli, L., Laurino, A., Spinelli, V., Mello, T., Sartiani, L., et al. (2018)
[Selective HCN1 Block as a Strategy to Control Oxaliplatin-Induced Neuropathy](#). *Neuropharmacology* 131, pp. 403–413. DOI: 10.1016/j.neuropharm.2018.01.014 (cited on p. 16).
- Riordan, J. R., Rommens, J. M., Kerem, B., Alon, N., Rozmahel, R., Grzelczak, Z., et al. (1989)
[Identification of the Cystic Fibrosis Gene: Cloning and Characterization of Complementary DNA](#). *Science* 245.4922, pp. 1066–1073. DOI: 10.1126/science.2475911 (cited on p. 33).

- Rivolta, I., Binda, A., Masi, A., and DiFrancesco, J. C. (2020)
[Cardiac and Neuronal HCN Channelopathies](#). *Pflügers Archiv - European Journal of Physiology* 472.7, pp. 931–951. DOI: [10.1007/s00424-020-02384-3](#) (cited on p. 33).
- Romanelli, M. N., Del Lungo, M., Guandalini, L., Zobeiri, M., Gyökeres, A., Árpádfy-Lovas, T., et al. (2019)
[EC18 as a Tool To Understand the Role of HCN₄ Channels in Mediating Hyperpolarization-Activated Current in Tissues](#). *ACS Medicinal Chemistry Letters* 10.4, pp. 584–589. DOI: [10.1021/acsmchemlett.8b00587](#) (cited on p. 16).
- Roux, B. (2008)
[The Membrane Potential and Its Representation by a Constant Electric Field in Computer Simulations](#). *Biophysical Journal* 95.9, pp. 4205–16. DOI: [10.1529/biophysj.108.136499](#) (cited on p. 25).
- Roy, R. N., Hendriks, K., Kopec, W., Abdolvand, S., Weiss, K. L., de Groot, B. L., et al. (2021)
[Structural Plasticity of the Selectivity Filter in a Nonselective Ion Channel](#). *IUCrJ* 8.3(3). DOI: [10.1107/S205225252100213X](#) (cited on p. 42).
- Salamon, P., Wales, D., Segall, A., Lai, Y.-A., Schön, J. C., Hoffmann, K. H., et al. (2015)
[Rate Constants, Timescales, and Free Energy Barriers](#). *Journal of Non-Equilibrium Thermodynamics* 41.1, pp. 13–18. DOI: [10.1515/jnet-2015-0038](#) (cited on pp. 29, 53).
- Sali, A. and Blundell, T. L. (1993)
[Comparative Protein Modelling by Satisfaction of Spatial Restraints](#). *Journal of Molecular Biology* 234.3, pp. 779–815. DOI: [10.1006/jmbi.1993.1626](#) (cited on p. 93).
- Santoro, B., Liu, D. T., Yao, H., Bartsch, D., Kandel, E. R., Siegelbaum, S. A., et al. (1998)
[Identification of a Gene Encoding a Hyperpolarization-Activated Pacemaker Channel of Brain](#). *Cell* 93.5, pp. 717–729. DOI: [10.1016/S0092-8674\(00\)81434-8](#) (cited on pp. 17, 41, 48).
- Santoro, B. and Shah, M. M. (2020)
[Hyperpolarization-Activated Cyclic Nucleotide-Gated Channels as Drug Targets for Neurological Disorders](#). *Annual Review of Pharmacology and Toxicology* 60.1, pp. 109–131. DOI: [10.1146/annurev-pharmtox-010919-023356](#) (cited on pp. 15, 16, 34).
- Saponaro, A., Bauer, D., Giese, M. H., Swuec, P., Porro, A., Gasparri, F., et al. (2021)
[Gating Movements and Ion Permeation in HCN₄ Pacemaker Channels](#). *Molecular Cell* 81.14, pp. 2929–2943. DOI: [10.1016/j.molcel.2021.05.033](#) (cited on pp. 11, 13, 17–19, 41, 42, 55).
- Schulze-Bahr, E., Neu, A., Friederich, P., Kaupp, U. B., Breithardt, G., Pongs, O., et al. (2003)
[Pacemaker Channel Dysfunction in a Patient with Sinus Node Disease](#). *Journal of Clinical Investigation* 111.10, pp. 1537–1545. DOI: [10.1172/JCI200316387](#) (cited on p. 16).
- Seifert, R., Scholten, A., Gauss, R., Mincheva, A., Lichter, P., and Kaupp, U. B. (1999)
[Molecular Characterization of a Slowly Gating Human Hyperpolarization-Activated Channel Predominantly Expressed in Thalamus, Heart, and Testis](#). *Proceedings of the National Academy of Sciences* 96.16, pp. 9391–9396. DOI: [10.1073/pnas.96.16.9391](#) (cited on p. 17).
- Shen, H., Liu, D., Wu, K., Lei, J., and Yan, N. (2019)
[Structures of Human Nav1.7 Channel in Complex with Auxiliary Subunits and Animal Toxins](#). *Science* 363.6433, pp. 1303–1308. DOI: [10.1126/science.aaw2493](#) (cited on p. 7).
- Shi, C., He, Y., Hendriks, K., De Groot, B. L., Cai, X., Tian, C., et al. (2018)
[A Single NaK Channel Conformation Is Not Enough for Non-Selective Ion Conduction](#). *Nature Communications* 9.1, pp. 1–8. DOI: [10.1038/s41467-018-03179-y](#) (cited on pp. 13, 19, 25, 42).

- Smart, O. S., Neduvilil, J. G., Wang, X., Wallace, B., and Sansom, M. S. (1996)
[HOLE: A Program for the Analysis of the Pore Dimensions of Ion Channel Structural Models](#). *Journal of Molecular Graphics* 14.6, pp. 354–360. DOI: [10.1016/S0263-7855\(97\)00009-X](#) (cited on pp. 94, 95).
- Sosnay, P. R., Castellani, C., Corey, M., Dorfman, R., Zielenski, J., Karchin, R., et al. (2011)
 “Evaluation of the Disease Liability of CFTR Variants”. *Cystic Fibrosis*. Vol. 742. Methods in Molecular Biology. Humana Press, pp. 355–372. DOI: [10.1007/978-1-61779-120-8_21](#) (cited on p. 33).
- Souaille, M. and Roux, B. (2001)
[Extension to the Weighted Histogram Analysis Method: Combining Umbrella Sampling with Free Energy Calculations](#). *Computer Physics Communications* 135.1, pp. 40–57. DOI: [10.1016/S0010-4655\(00\)00215-0](#) (cited on p. 26).
- Souza, P. C. T., Alessandri, R., Barnoud, J., Thallmair, S., Faustino, I., Grünewald, F., et al. (2021)
[Martini 3: A General Purpose Force Field for Coarse-Grained Molecular Dynamics](#). *Nature Methods* 18.4 (4), pp. 382–388. DOI: [10.1038/s41592-021-01098-3](#) (cited on p. 25).
- Stieber, J., Hofmann, F., and Ludwig, A. (2004)
[Pacemaker Channels and Sinus Node Arrhythmia](#). *Trends in Cardiovascular Medicine* 14.1, pp. 23–28. DOI: [10.1016/j.tcm.2003.09.006](#) (cited on p. 16).
- Stock, L., Delemotte, L., Carnevale, V., Treptow, W., and Klein, M. L. (2013)
[Conduction in a Biological Sodium Selective Channel](#). *The Journal of Physical Chemistry B* 117.14, pp. 3782–3789. DOI: [10.1021/jp401403b](#) (cited on pp. 45, 96).
- Strauss, U., Kole, M. H. P., Bräuer, A. U., Pahnke, J., Bajorat, R., Rolfs, A., et al. (2004)
[An Impaired Neocortical Ih Is Associated with Enhanced Excitability and Absence Epilepsy](#). *The European Journal of Neuroscience* 19.11, pp. 3048–3058. DOI: [10.1111/j.0953-816X.2004.03392.x](#) (cited on p. 16).
- Sulfi, S. and Timmis, A. D. (2006)
[Ivabradine – the First Selective Sinus Node If Channel Inhibitor in the Treatment of Stable Angina](#). *International Journal of Clinical Practice* 60.2, pp. 222–228. DOI: [10.1111/j.1742-1241.2006.00817.x](#) (cited on p. 16).
- Sun, Q., Xing, G.-G., Tu, H.-Y., Han, J.-S., and Wan, Y. (2005)
[Inhibition of Hyperpolarization-Activated Current by ZD7288 Suppresses Ectopic Discharges of Injured Dorsal Root Ganglion Neurons in a Rat Model of Neuropathic Pain](#). *Brain Research* 1032.1-2, pp. 63–69. DOI: [10.1016/j.brainres.2004.10.033](#) (cited on p. 16).
- Sunkara, M. R., Schwabe, T., Ehrlich, G., Kusch, J., and Benndorf, K. (2018)
[All Four Subunits of HCN2 Channels Contribute to the Activation Gating in an Additive but Intricate Manner](#). *The Journal of General Physiology* 150.9, pp. 1261–1271. DOI: [10.1085/jgp.201711935](#) (cited on p. 11).
- Tanguay, J., Callahan, K. M., and D’Avanzo, N. (2019)
[Characterization of Drug Binding within the HCN1 Channel Pore](#). *Scientific Reports* 9.1, p. 465. DOI: [10.1038/s41598-018-37116-2](#) (cited on pp. 44, 45).
- Tao, X. and MacKinnon, R. (2019)
[Cryo-EM Structure of the KvAP Channel Reveals a Non-Domain-Swapped Voltage Sensor Topology](#). *eLife* 8. DOI: [10.7554/eLife.52164](#) (cited on p. 8).

- Tayefeh, S., Kloss, T., Thiel, G., Hertel, B., Moroni, A., and Kast, S. M. (2007)
[Molecular Dynamics Simulation of the Cytosolic Mouth in Kcv-Type Potassium Channels †](#). *Biochemistry* 46.16, pp. 4826–4839. DOI: [10.1021/bi602468r](#) (cited on p. 37).
- Thompson, A. N., Kim, I., Panosian, T. D., Iverson, T. M., Allen, T. W., and Nimigean, C. M. (2009)
[Mechanism of Potassium Channel Selectivity Revealed by Na⁺ and Li⁺ Binding Sites within the KcsA Pore](#). *Nature structural & molecular biology* 16.12, pp. 1317–1324. DOI: [10.1038/nsmb.1703](#) (cited on pp. 13, 41, 49).
- Thon, S., Schmauder, R., and Benndorf, K. (2013)
[Elementary Functional Properties of Single HCN₂ Channels](#). *Biophysical Journal* 105.7, pp. 1581–1589. DOI: [10.1016/j.bpj.2013.08.027](#) (cited on pp. 54, 55).
- Trudeau, M. C. and Zheng, J. (2015)
 Handbook of Ion Channels. 1st ed. CRC Press (cited on pp. 7, 8, 10, 11).
- Tuckerman, M. E. and Martyna, G. J. (2000)
[Understanding Modern Molecular Dynamics: Techniques and Applications](#). *The Journal of Physical Chemistry B* 104.2, pp. 159–178. DOI: [10.1021/jp992433y](#) (cited on p. 21).
- Twomey, E. C., Yelshanskaya, M. V., Grassucci, R. A., Frank, J., and Sobolevsky, A. I. (2017)
[Channel Opening and Gating Mechanism in AMPA-Subtype Glutamate Receptors](#). *Nature* 549.7670 (7670), pp. 60–65. DOI: [10.1038/nature23479](#) (cited on p. 7).
- Van Der Spoel, D., Lindahl, E., Hess, B., Groenhof, G., Mark, A. E., and Berendsen, H. J. C. (2005)
[GROMACS: Fast, Flexible, and Free](#). *Journal of Computational Chemistry* 26.16, pp. 1701–1718. DOI: [10.1002/jcc.20291](#) (cited on pp. 93, 96).
- Van Duin, A. C. T., Dasgupta, S., Lorant, F., and Goddard, W. A. (2001)
[ReaxFF: A Reactive Force Field for Hydrocarbons](#). *The Journal of Physical Chemistry A* 105.41, pp. 9396–9409. DOI: [10.1021/jp004368u](#) (cited on p. 27).
- Vanommeslaeghe, K., Hatcher, E., Acharya, C., Kundu, S., Zhong, S., Shim, J., et al. (2010)
[CHARMM General Force Field: A Force Field for Drug-like Molecules Compatible with the CHARMM All-Atom Additive Biological Force Fields](#). *Journal of Computational Chemistry* 31.4, pp. 671–90. DOI: [10.1002/jcc.21367](#) (cited on p. 24).
- Vora, T., Bisset, D., and Chung, S.-H. (2008)
[Conduction of Na⁺ and K⁺ through the NaK Channel: Molecular and Brownian Dynamics Studies](#). *Biophysical Journal* 95.4, pp. 1600–11. DOI: [10.1529/biophysj.107.126722](#) (cited on pp. 46, 49).
- Wahl-Schott, C., Baumann, L., Zong, X., and Biel, M. (2005)
[An Arginine Residue in the Pore Region Is a Key Determinant of Chloride Dependence in Cardiac Pacemaker Channels *](#). *Journal of Biological Chemistry* 280.14, pp. 13694–13700. DOI: [10.1074/jbc.M413197200](#) (cited on p. 17).
- Wainger, B. J., DeGennaro, M., Santoro, B., Siegelbaum, S. A., and Tibbs, G. R. (2001)
[Molecular Mechanism of cAMP Modulation of HCN Pacemaker Channels](#). *Nature* 411.6839 (6839), pp. 805–810. DOI: [10.1038/35081088](#) (cited on p. 93).
- Wang, W. and MacKinnon, R. (2017)
[Cryo-EM Structure of the Open Human Ether-à-Go-Go-Related K⁺ Channel hERG](#). *Cell* 169.3, 422–430.e10. DOI: [10.1016/j.cell.2017.03.048](#) (cited on pp. 7, 43).
- Wassenaar, T. A., Pluhackova, K., Böckmann, R. A., Marrink, S. J., and Tieleman, D. P. (2014)
[Going Backward: A Flexible Geometric Approach to Reverse Transformation from Coarse Grained](#)

- to Atomistic Models. *Journal of Chemical Theory and Computation* 10.2, pp. 676–690. DOI: 10.1021/ct400617g (cited on p. 25).
- Wojtas-Niziurski, W., Meng, Y., Roux, B., and Bernèche, S. (2013)
Self-Learning Adaptive Umbrella Sampling Method for the Determination of Free Energy Landscapes in Multiple Dimensions. *Journal of Chemical Theory and Computation* 9.4, pp. 1885–1895. DOI: 10.1021/ct300978b (cited on pp. 26, 55, 98).
- Wolf, M. G., Hoefling, M., Aponte-Santamaría, C., Grubmüller, H., and Groenhof, G. (2010)
G_membed: Efficient Insertion of a Membrane Protein into an Equilibrated Lipid Bilayer with Minimal Perturbation. *Journal of Computational Chemistry* 31.11, pp. 2169–2174. DOI: 10.1002/jcc.21507 (cited on pp. 93, 95).
- Wu, E. L., Cheng, X., Jo, S., Rui, H., Song, K. C., Dávila-Contreras, E. M., et al. (2014)
CHARMM-GUI Membrane Builder toward Realistic Biological Membrane Simulations. *Journal of Computational Chemistry* 35.27, pp. 1997–2004. DOI: 10.1002/jcc.23702 (cited on pp. 25, 95).
- Xie, W., Orozco, M., Truhlar, D. G., and Gao, J. (2009)
X-Pol Potential: An Electronic Structure-Based Force Field for Molecular Dynamics Simulation of a Solvated Protein in Water. *Journal of Chemical Theory and Computation* 5.3, pp. 459–467. DOI: 10.1021/ct800239q (cited on p. 27).
- Ye, S., Li, Y., and Jiang, Y. (2010)
Novel Insights into K⁺ Selectivity from High-Resolution Structures of an Open K⁺ Channel Pore. *Nature Structural & Molecular Biology* 17.8 (8), pp. 1019–1023. DOI: 10.1038/nsmb.1865 (cited on pp. 11, 43).
- Yellen, G. (2002)
The Voltage-Gated Potassium Channels and Their Relatives. *Nature* 419.6902, pp. 35–42. DOI: 10.1038/nature00978 (cited on p. 13).
- Yu, X., Chen, X.-W., Zhou, P., Yao, L., Liu, T., Zhang, B., et al. (2007)
Calcium Influx through If Channels in Rat Ventricular Myocytes. *American Journal of Physiology-Cell Physiology* 292.3, pp. C1147–C1155. DOI: 10.1152/ajpcell.00598.2005 (cited on p. 17).
- Yu, X., Duan, K.-L., Shang, C.-F., Yu, H.-G., and Zhou, Z. (2004)
Calcium Influx through Hyperpolarization-Activated Cation Channels (Ih Channels) Contributes to Activity-Evoked Neuronal Secretion. *Proceedings of the National Academy of Sciences* 101.4, pp. 1051–1056. DOI: 10.1073/pnas.0305167101 (cited on p. 17).
- Zhou, Y. and MacKinnon, R. (2003)
The Occupancy of Ions in the K⁺ Selectivity Filter: Charge Balance and Coupling of Ion Binding to a Protein Conformational Change Underlie High Conduction Rates. *Journal of Molecular Biology* 333.5, pp. 965–975. DOI: 10.1016/j.jmb.2003.09.022 (cited on p. 49).
- Zhou, Y., Morais-Cabral, J. H., Kaufman, A., and MacKinnon, R. (2001)
Chemistry of Ion Coordination and Hydration Revealed by a K⁺ Channel–Fab Complex at 2.0 Å Resolution. *Nature* 414.6859 (6859), pp. 43–48. DOI: 10.1038/35102009 (cited on pp. 12, 13, 49, 64).

Part IV

Appendix

CHAPTER A

Abbreviations

AA	amino acid
Ca ²⁺	calcium
cAMP	cyclic-adenosine monophosphate
CF	cystic fibrosis
CFTR	cystic fibrosis transmembrane conductance regulator
cGMP	cyclic-guanosine monophosphate
Cl ⁻	chloride
CNBD	cyclic-nucleotide binding-domain
COM	center-of-mass
CV	collective variable
FES	free energy surface
HCN	hyperpolarization-activated cyclic nucleotide-gated
HCND	HCN domain
I _f	funny current
K _v	voltage-gated potassium channel
K ⁺	potassium
K ⁺ channel	potassium channel
KTN	nucleotide-binding domain
LBD	ligand-binding domain
LJ	Lennard-Jones
MD	molecular dynamics
MFEP	minimal free energy pathway
Na ⁺	sodium
NEB	nudged elastic band
PBC	periodic boundary conditions
PD	pore domain
PME	particle-mesh Ewald
PMF	potential of mean force
POPC	palmitoylcholine
RDF	radial distribution function
SAN	sinoatrial node
SF	selectivity filter
TEA ⁺	tetraethylazanium
TMH	transmembrane helix
TPCs	two-pore channels
TRIP8b	tetratricopeptide repeat-containing Rab8b-interacting protein
TST	transition state theory
US	umbrella sampling
VdW	Van der Waals

VGIC voltage-gated ion channel
VSD voltage sensor domain
WHAM Weighted Histogram Analysis Method
wt wildtype

CHAPTER B

Sequence Alignment of HCN channels

	HCNA	HCNB	HCNC	
hHCN1 O60741	F T S M L Q P G V N K F S L R M F G S Q K A V E K E Q E R V			127
hHCN2 Q9UL51	F G A L L Q P G V N K F S L R M F G S Q K A V E R E Q E R V			196
hHCN3 Q9P1Z3	L G T L L Q P T V N K F S L R V F G S H K A V E I E Q E R V			78
hHCN4 Q9Y3Q4	F C A M L Q P G V N K F S L R M F G S Q K A V E R E Q E R V			247
spHCN O76977	L W T V L Q P S D N R L S M K L F G S K K G L Q K E K Y R L			200
	218 219 220 221 222 223 224 225 226 227 228	F109	230 231 232 233 234 235 236 237 238 239 240 241 242 243 244 245 246 247	

	S1			
hHCN1 O60741	K T A G F W I I H P Y S D F R F Y W D L I M L I M M V G N L			157
hHCN2 Q9UL51	K S A G A W I I H P Y S D F R F Y W D F T M L L F M V G N L			226
hHCN3 Q9P1Z3	K S A G A W I I H P Y S D F R F Y W D L I M L L L M V G N L			108
hHCN4 Q9Y3Q4	K S A G F W I I H P Y S D F R F Y W D L T M L L L M V G N L			277
spHCN O76977	R K A G V L I I H P C S H R F R F Y W D L L M L C L I M A N V			230
	248 249 250 251 252 253 254 255 256 257 258 259 260 261 262 263 264 265 266 267 268 269 270 271 272 273 274 275 276 277			

	S1		S2	
hHCN1 O60741	V I I P V G I T F F K . E Q T T P W I I F N V A S D T V F			186
hHCN2 Q9UL51	I I I P V G I T F F K . D E T T A P W I V F N V S D T F F			255
hHCN3 Q9P1Z3	I V L P V G I T F F K . E E N S P W I V F N V L S D T F F			137
hHCN4 Q9Y3Q4	I I I P V G I T F F K . D E N T T P W I V F N V S D T F F			306
spHCN O76977	I L L P V V I T F F H N K D M S T G W L I F N C F S D T F F			260
	278 279 280 281 282 283 284 285 286 287 288		289 290 291 292 293 294 295 296 297 298 299 300 301 302 303 304 305 306	

	S2		S3	
hHCN1 O60741	L L D L I M N F R T G T V N E D S S E . I I L D P K V I K M			215
hHCN2 Q9UL51	L M D L V L N F R T G I V I E D N T E . I I L D P E K I K K			284
hHCN3 Q9P1Z3	L L D L V L N F R T G I V V E E G A E . I L L A P R A I R T			166
hHCN4 Q9Y3Q4	L I D L V L N F R T G I V V E D N T E . I I L D P Q R I K M			335
spHCN O76977	I L D L I C N F R T G I M N P K S A E Q V I L N P R Q I A Y			290
	307 308 309 310 311 312 313 314 315 316 317 318 319 320 321 322 323 324 325		326 327 328 329 330 331 332 333 334 335	

	S3			
hHCN1 O60741	N Y L K S W F V V D F I S S I P V D Y I F L I V E K G . . M			243
hHCN2 Q9UL51	K Y L R T W F V V D F V S S I P V D Y I F L I V E K G . . I			312
hHCN3 Q9P1Z3	R Y L R T W F L V D L I S S I P V D Y I F L V V E L E P R L			196
hHCN4 Q9Y3Q4	K Y L K S W F M V D F I S S I P V D Y I F L I V E T R . . I			363
spHCN O76977	H Y L R S W F I I D L V S S I P M D Y I F L L A G G Q . . .			317
	336 337 338 339 340 341 342 343 344 345 346 347 348 349 350 351 352 353 354 355 356 357 358 359 360 361 362 363			

		S4	
hHCN1 O60741	DSEVYKTARALRIVRFTKILSLRLLRSLR		273
hHCN2 Q9UL51	DSEVYKTARALRIVRFTKILSLRLLRSLR		342
hHCN3 Q9P1Z3	DAEVYKTARALRIVRFTKILSLRLLRSLR		226
hHCN4 Q9Y3Q4	DSEVYKTARALRIVRFTKILSLRLLRSLR		393
spHCN O76977	NRHFLEVSRALKILRFKLLSLRLLRSLR		347
	364 365 366 367 368 369 370 371 372 373 374 375 376 377 378 379 380 381 382 383 384 385 386 387 388 389 390 391 392 393		

		S4		S5													
hHCN1 O60741	LIRYIHQWEEIFHMTYDLASAVVRI	F	N	L	I	G	303										
hHCN2 Q9UL51	LIRYIHQWEEIFHMTYDLASAVM	R	I	C	N	L	I	S	372								
hHCN3 Q9P1Z3	LIRYIHQWEEIFHMTYDLASAVVRI	F	N	L	I	G	256										
hHCN4 Q9Y3Q4	LIRYIHQWEEIFHMTYDLASAVVRI	V	N	L	I	G	423										
spHCN O76977	LMRFVSVQWEQAFN	...	V	A	N	A	V	I	R	I	C	N	L	V	C	373	
	394 395 396 397 398 399 400 401 402 403 404 405 406 407 408 409 410 411 412 413 414 415 416 417 418 419 420 421 422 423																

		S5															
hHCN1 O60741	MMLLLCHWDGCLQFLVPL	L	L	Q	D	F	F	P	D	C	W	V	S	L	333		
hHCN2 Q9UL51	MMLLLCHWDGCLQFLVPL	M	L	Q	D	F	F	P	R	N	C	W	V	S	I	402	
hHCN3 Q9P1Z3	MMLLLCHWDGCLQFLVPL	M	L	Q	D	F	F	P	D	C	W	V	S	I	286		
hHCN4 Q9Y3Q4	MMLLLCHWDGCLQFLVPL	M	L	Q	D	F	F	P	D	C	W	V	S	I	453		
spHCN O76977	MMLLIGHWNGCLQY	L	V	P	M	L	Q	E	Y	P	D	Q	S	W	A	I	403
	424 425 426 427 428 429 430 431 432 433 434 435 436 437 438 439 440 441 442 443 444 445 446 447 448 449 450 451 452 453																

				p-Helix		SF		
hHCN1 O60741	NEMVND	SWGK	QYSY	ALFKAMSHML	CIGY	G	A	363
hHCN2 Q9UL51	NGMVNHSW	SELYS	FALFKAMSHML	CIGY	G	R	A	432
hHCN3 Q9P1Z3	NHMVNHSWGR	QYSH	ALFKAMSHML	CIGY	G	Q		316
hHCN4 Q9Y3Q4	NNMVNNSWGK	QYSY	ALFKAMSHML	CIGY	G	R		483
spHCN O76977	NGLEHAHWWE	QYTW	ALFKAL	SHML	CIGY	G	K	433
	454 455 456 457 458 459 460 461 462 463 464 465 466 467 468 469 470 471 472 473 474 475 476 477 478 479 480 481 482 483							

		S6						
hHCN1 O60741	QAPVMS	SDLW	ITMLSMIVGATCYAMFV	GHA	393			
hHCN2 Q9UL51	QAPES	SMTDI	WLTMLSMIVGATCYAMF	IGHA	462			
hHCN3 Q9P1Z3	QAPV	GMPDV	WLTMLSMIVGATCYAMF	IGHA	346			
hHCN4 Q9Y3Q4	QAPV	GMSDV	WLTMLSMIVGATCYAMF	IGHA	513			
spHCN O76977	FPP	Q	SITD	VWLTIVSMVSGATCF	ALF	I	GHA	463
	484 485 486 487 488 489 490 491 492 493 494 495 496 497 498 499 500 501 502 503 504 505 506 507 508 509 510 511 512 513							

HCN1 G391E

		S6		C-linker A	
hHCN1 O60741	TALIQSLDSSRRQY	QEKYKQVE	QYMSFHKL	423	
hHCN2 Q9UL51	TALIQSLDSSRRQY	QEKYKQVE	QYMSFHKL	492	
hHCN3 Q9P1Z3	TALIQSLDSSRRQY	QEKYKQVE	QYMSFHKL	376	
hHCN4 Q9Y3Q4	TALIQSLDSSRRQY	QEKYKQVE	QYMSFHKL	543	
spHCN O76977	TNLIQSM	DSSSRQYREK	LKQVEYMQYRKL	493	
	514 515 516 517 518 519 520 521 522 523 524 525 526 527 528 529 530 531 532 533 534 535 536 537 538 539 540 541 542 543				

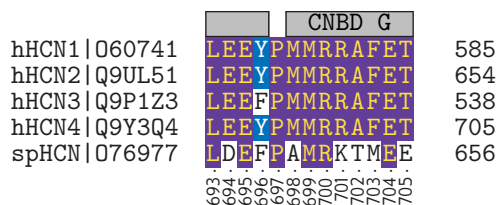
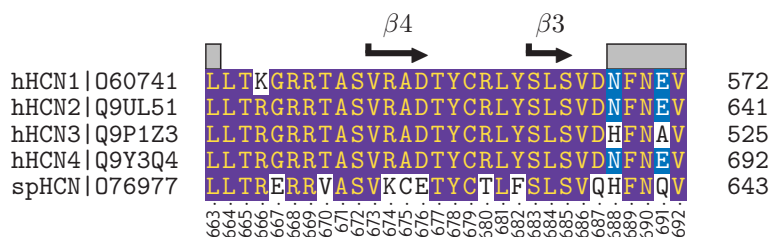
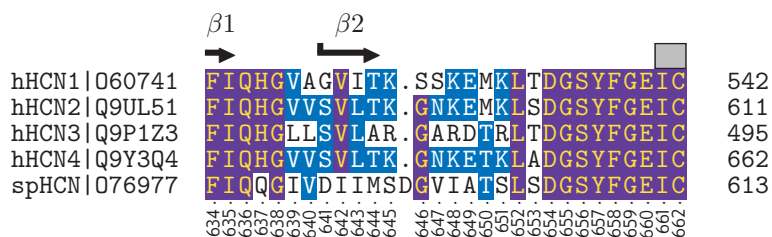
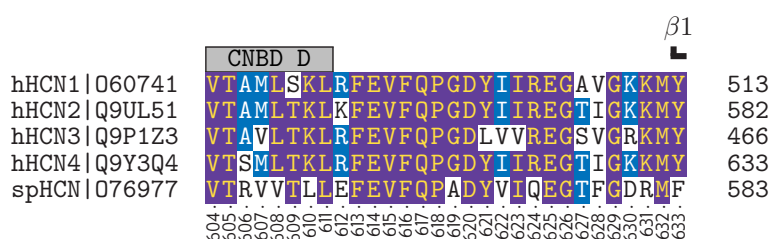
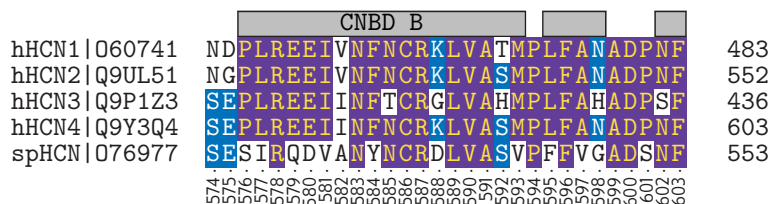
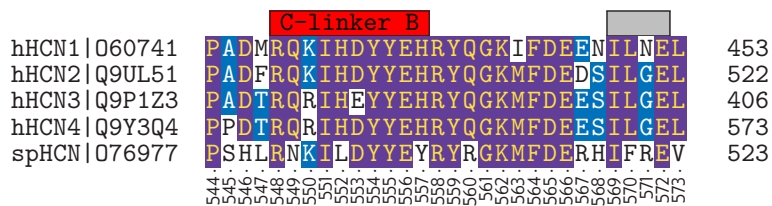


Figure B.1: Alignment of several HCN channels. Only amino acids from HCN4 residues 218-705 are shown. Important domains are labeled as α -helices (helices) and beta sheets (arrows) and other regions of interest are highlighted in red. The multiple-sequence alignment was calculated with ClustalW: Larkin et al. (2007).

CHAPTER C

Simulation Details

C.1 MODELING MUTATIONS

C.1.1 Simulation Setup and Analysis

The Cryo-EM structure of human HCN1 (PDB: 5U6P)¹ was used as starting point for mutational studies. Unresolved residues of the loop regions and point-mutations were introduced via homology modeling with Modeller 9.19². Titratable side chains were protonated according to their estimated pKa value using PROPKA3³. For some simulations, the C-linker and CNBD were cut-off to save simulation time (R4O4X). This truncation model (HCN1_{TMD} from here on) was shown to still be sensitive to voltage while maintaining apo-like activation kinetics⁴. However, if not mentioned otherwise, the fully resolved protein (HCN1 from here on) ranging from residue M94 to D608 was used.

The proteins were embedded into a solvated and pre-equilibrated palmitoylcholine (POPC) bilayer using `g_membed` and K⁺ ions were placed in the SF at binding site s_4 and in the central cavity (s_{cav})⁵. Finally, the internal cavity was solvated with VOID00/FLOOD⁶ and charge imbalances were balanced out by randomly replacing solvent molecules with K⁺ or Cl⁻ ions in the solution. A detailed composition of investigated systems is given in Table C.1.

	#Molecules				Simulation time / ns
	POPC	TIP3P	K ⁺	Cl ⁻	
HCN1	560	68,852	187	199	100
HCN1 _{G391C}	560	68,852	187	199	100
HCN1 _{G391S}	560	68,852	187	195	100
HCN1 _{G391D}	560	68,852	187	199	100
HCN1 _{TMD}	495	41,933	122	114	50
HCN1 _{TMD,G391D}	494	41,967	126	114	100
HCN1 _{TMD,AC=G391D}	494	41,911	124	114	100
HCN1 _{TMD,AB=G381D}	494	41,970	124	114	100
HCN1	487	66,415	180	184	50
HCN1 _{F109W}	491	66,454	179	183	50
HCN1 _{F109M}	491	66,453	179	183	50
HCN1 _{F109V}	487	66,416	179	183	50
HCN1 _{F109A}	491	66,416	180	184	50
HCN1 _{F109E}	491	66,448	182	182	50

Simulations were performed with GROMACS 2018 in combination with the CHARMM36m forcefield⁷. The TIP3P water model with additional LJ potentials as implemented in CHARMM36m was used⁸. The integration time step was 2 fs. Van der Waals forces were switched to zero

¹ Lee and MacKinnon (2017).

² Sali and Blundell (1993); Fiser, Do, and Šali (2000).

³ Olsson et al. (2011).

⁴ Wainger et al. (2001).

⁵ Wolf et al. (2010).

⁶ Kleywegt and T. A. Jones (1994).

Table C.1: Overview over simulation systems used for mutation studies. The subscript “TMD” marks simulations with a truncated model that does not contain the CNBD. If only some subunits are mutated, this is also indicated by the subscript.

⁷ Van Der Spoel et al. (2005); Pronk et al. (2013); Huang and MacKerell (2013).

⁸ Jorgensen et al. (1983).

between 0.8 and 1.2 nm. Electrostatic interactions were represented using the PME method with a Coulomb cut-off of 1.2 nm⁹. Hydrogen bonds were kept constant using the LINCS algorithm¹⁰. The stochastic velocity-rescale thermostat with a coupling time constant of 0.1 ps was used to keep the simulation temperature at 298 K¹¹. The pressure was kept at 1 bar (semiisotropic) using the Parrinello-Rahman barostat with a coupling constant of 5 ps¹². Prior to 100 ns restraint-free production simulation, systems were energy minimized (steepest descend, 5000 steps) and equilibrated (10 ns NPT simulation). During equilibration, protein heavy atoms were restrained to their initial position by a force constant of 1000 kJ mol⁻¹ nm⁻².

⁹ Essmann et al. (1995).

¹⁰ Hess et al. (1997).

¹¹ Bussi, Donadio, and Parrinello (2007).

¹² Parrinello and Rahman (1981).

Analysis

- General analysis was performed using GROMACS, Biotite (various versions) and MDAnalysis 0.20¹³.
- The pore radii of channels were calculated with HOLE using van der Waals radii from the AMBER united atom force field and a sample plane distance of 1 Å¹⁴. For trajectories, HOLE calculations were run for every time step of the equilibrated system and the results were averaged. The standard error was then estimated via a percentile bootstrapping approach and shows the 95 % confidence interval over 10,000 bootstrapping runs.
- Hydrogen bonds were calculated using the Baker-Hubbard algorithm ($d_{H,A}=2.5 \text{ \AA}$, $\theta_{D,H,A}=120^\circ$)¹⁵.
- Pore solvation was estimated based on the distance between water molecules and selected residues inside the HCN1 PD. Therefore, only water molecules with their oxygen atom closer than 5 Å to the side chain of either Y386 or V390 were considered as inside the central pore.
- The solvent RDF was calculated on the last 25 ns of each trajectory for the center-of-mass (COM) of a subset of representative atoms for each amino acid side chain terminal group. For example, for glutamic acid, the COM of the two carboxyl oxygens was used. For the solvent selection, only water oxygen atoms were considered. The resulting RDF from the four subunits was averaged.
- Average minimal distances were calculated from the last 25 ns of each trajectory by calculating the distance between all atoms of one residue's side chain with all atoms from another residue's side chain and taking the minimum distance for each time step. The Spearman correlation coefficient ρ_S between distances and $\Delta V_{1/2}$ shifts was then calculated between the average minimum distance and the average $\Delta V_{1/2}$.

¹³ Kunzmann and Hamacher (2018); Gowers et al. (2016); Michaud-Agrawal et al. (2011).

¹⁴ Smart et al. (1996).

¹⁵ E. N. Baker and Hubbard (1984).

C.2 ION CONDUCTION SIMULATIONS

C.2.1 Hole Analysis

Pore radii of HCN₄_{holo} (PDB: 7NP4), HCN₄_{apo} (PDB: 7NP3), closed HCN₁ (PDB: 5U6P) and open hERG (PDB: 5VA2) were calculated with HOLE using Amber van der Waals radii and a sampling distance of 1 Å along the principal axis of the protein¹⁶.

¹⁶ Smart et al. (1996).

C.2.2 Molecular Docking

In-silico docking experiments were performed on HCN₄_{holo} (PDB: 7NP4), HCN₄_{apo} (PDB: 7NP3) and closed HCN₁ (PDB: 5U6P). AutoDock 4.2.6 in conjunction with AutoDockTools 1.5.6 was used for preparation of proteins and ligands¹⁷. Ligands were drawn and energy-minimized with Avogadro using the UFF force field¹⁸. All bound ligands, detergents and water molecules were removed from protein structures prior to model preparation. Gasteiger charges were used. A cubic box with $x=4.725$ nm and a grid spacing of 0.0375 nm was centered below the SF to include the central pore module and C-linker. 250 docking attempts with 2,500,000 evaluations were performed per protein-ligand system and clustered based on RMSD. The density of ivabradine was calculated from docked poses as 3D histogram over the atomic coordinates with a grid spacing of 0.1 nm. Only bins with a count of at least 3 were considered for density profiles.

¹⁷ Morris, Huey, et al. (2009).

¹⁸ Hanwell et al. (2012); Rappe et al. (1992).

C.2.3 Simulation Setup and Analysis

Molecular Dynamics

Simulations and Analysis of full channel constructs were performed using the full structure of HCN₄_{holo} (PDB: 7NP4) or HCN₄_{apo} (PDB: 7NP3). Simulations of only the pore domain (residues 412 to 523) were performed on either of the HCN₄_{apo} structures solved in LMNG (PDB: 7NP3) or amphipols (PDB: 7NMN).

For molecular dynamics simulations, proteins were embedded into a pre-equilibrated POPC bilayer using `g_membed` or the solvent-membrane system was built around the protein via the CHARMM-GUI web server¹⁹. The central cavity was solvated with VOIDOO/FLOOD, followed by placement of additional ions in the selectivity filter and cavity²⁰. Ion starting configurations were selected based on testing different variations in the initial positioning of the ions (either one or two K⁺/Na⁺ inside the SF, with or without a separating water molecule) prior to production runs. Based on results from these preliminary trial runs, the following configurations were selected: For simulations in pure KCl solution, K⁺ ions were initially placed at positions $[p_{23}, s_4]$, separated by a single water molecule. For pure NaCl and mixed KCl:NaCl solutions, a single Na⁺ ion was placed inside the SF at p_{34} with two wa-

¹⁹ Wolf et al. (2010); Jo et al. (2008); Wu et al. (2014).

²⁰ Kleywegt and T. A. Jones (1994).

ter molecules above and below, due to the fact that the two ion configuration was not stable. For simulations of HCN₄^{holo}, a single K⁺ was placed at binding site s₄. Individual simulation conditions and the final composition of each system in production runs are summarized in the appropriate section below.

All simulations were carried out with GROMACS 2019 in conjunction with the Amber99sb*-ILDN force field, the TIP3P water model, Berger-derived POPC lipids and ion parameters by Joung and Cheatham²¹. Van der Waals interactions were cut-off at 1 nm and electrostatics were treated by PME beyond 1 nm²². Temperature and Pressure were kept at 310 K and 1 bar using the V-Rescale Thermostat and Parrinello-Rahman Barostat, respectively²³. All bonds were restraint using LINCS and hydrogen atoms were represented as virtual sites to allow for an integration time step of 4 fs²⁴. After preparation, systems were minimized for 2000 steps (steepest descent) followed by at least 20 ns position-restrained equilibration ($F_c=1000 \text{ kJ mol}^{-1} \text{ nm}^{-2}$). Finally, restraints were gradually lifted over 3 ns followed by unrestrained simulation. A set of distance restraints were applied on the bottom half of the S6 helix to prevent the cytosolic gate from closing²⁵. Molecular dynamics trajectories were analyzed using GROMACS tools and Biotite²⁶.

²¹ Abraham et al. (2015); Van Der Spoel et al. (2005); Best and Hummer (2009); Lindorff-Larsen et al. (2010); Jorgensen et al. (1983); Cordoní, Caltabiano, and Pardo (2012); Joung and Cheatham (2008).

²² Essmann et al. (1995).

²³ Bussi, Donadio, and Parrinello (2007); Parrinello and Rahman (1981).

²⁴ Hess et al. (1997); Feenstra, Hess, and Berendsen (1999).

²⁵ Kopec et al. (2018).

²⁶ Kunzmann and Hamacher (2018).

Pore Solvation

Pore solvation simulations were performed using the full structure of HCN₄^{holo} (PDB: 7NP4) or HCN₄^{apo} (PDB: 7NP3) as described in [Appendix C.2.3](#). Simulations were run for 100 ns without distance restraints on S6. Simulation systems consisted of the respective protein and 49,413 water molecules, 310 lipids, 135 K⁺ and 135 chloride (Cl⁻) for HCN₄^{apo} or 47,956 water molecules, 312 lipids, 130 K⁺ and 146 Cl⁻ for HCN₄^{holo} ($c_{\text{KCl}} \approx 0.15 \text{ mM}$). The pore solvation was estimated by counting the number of water molecules inside the central cavity. Molecules were counted as being “inside” when they were closer than 0.5 nm to residues T507 or I511 of any subunit.

Conduction Simulations

Conduction simulations were performed using truncated pore models of HCN₄^{apo} solved in LMNG (PDB: 7NP3) or amphipols (PDB: 7NMN) prepared as described in [Appendix C.2.3](#). Short trial simulations were also performed to test a range of applied voltages and ion solution concentrations. To increase the rate of sampling of conduction events during production runs with an applied electric field, voltages in the range of -500 mV to -700 mV and ion concentrations up to 900 mM were used²⁷. Individual simulation conditions and system compositions are listed in [Table C.2](#). However, similar results regarding the conduction mechanism were observed at hyperpolarizing voltages as low as

²⁷ Andersson, Kasimova, and Delemotte (2018); Köpfer et al. (2014); Stock et al. (2013).

–300 mV and ion concentrations as low as 150 mM (Appendix D.3).

POPC	#Molecules				Ion conc. / mM	Simulation time /ns	Voltage / mV	#Conductions K ⁺ /Na ⁺
	TIP3P	K ⁺	Na ⁺	Cl ⁺				
202	13,823	229	0	221	900	1000	–500	7/-
202	13,824	229	0	221	900	500	–500	2/-
202	13,823	229	0	221	900	100	–500	0/-
202	13,824	229	0	221	900	500	–500	0/-
202	13,824	0	229	221	900	500	–500	-/0
202	13,824	0	229	221	900	500	–500	-/0
202	13,823	0	229	221	900	1000	–500	-/0
202	13,823	0	229	221	900	1000	–500	-/0
202	13,825	114	115	221	900	100	–500	0/0
202	13,825	114	115	221	900	100	–500	1/0
202	13,824	114	115	221	900	100	–500	0/0
202	13,824	114	115	221	900	100	–500	0/0
202	13,824	114	115	221	900	1000	–500	1/1
202	13,823	114	115	221	900	1000	–500	0/0
202	13,823	114	115	221	900	100	–500	0/0
202	13,824	114	115	221	900	100	–500	0/0
202	13,823	114	115	221	900	1000	–500	0/0
202	13,823	114	115	221	900	1000	–500	0/0
202	13,823	114	115	221	900	1000	–700	6/1
182	14,778	124	124	240	900	500	–500	0/1
182	14,778	124	124	240	900	500	–500	1/0
182	14,778	124	123	239	900	500	–500	1/0
182	14,778	123	124	239	900	500	–500	1/1

Ion and Water Permeation

Ion permeation and water co-permeation was calculated by evaluating the position of relevant atoms relative to the position of the SF. For the number of water molecules between adjacent ions, trajectories were filtered for frames with at least two ions inside or in close proximity to the SF. For these frames, the number of intercalating water molecules was then calculated based on the positions of the two closest ions and water molecules in their proximity.

Table C.2: Overview over simulation parameters for ion conduction simulations.

C.3 UMBRELLA SAMPLING/FREE ENERGY

Initial simulation systems were either based on equilibrated structures from conduction simulations, or build based on HCN_{4apo} (PDB: 7NP3) as described in Appendix C.2.3. For the latter case, two or three ions, either K⁺ or Na⁺, separated by a single water molecule were placed in the selectivity filter or central cavity and the negative charge on the protein (8e⁻) was then balanced by replacing six randomly selected solvent molecules with six additional K⁺. The compositions of final systems are listed in Table C.3 together with simulation parameters. To ob-

tain sufficiently equilibrated starting structures for free energy calculations, systems were further equilibrated for 100 ns without position restraints. During equilibration, the ions inside the pore were prevented from leaving it via repulsive potential walls ($k=10,000 \text{ kJ mol}^{-1} \text{ nm}^{-2}$) and further ions were prevented from entering the pore by the same mechanism.

System	#Molecules				Starting point ($z_1, z_2/z_{2,3}$) / nm	#Simulations
	POPC	TIP3P	K ⁺	Na ⁺		
K ⁺ /K ⁺	182	14,778	8	-	0.35, -0.25	247
K ⁺ /K ⁺ (2)	182	14,778	8	-	-0.15, -0.75	197
K ⁺ /K ⁺ /K ⁺	202	13,823	8	-	0.25, -0.55	361
K ⁺ /K ⁺ /K ⁺ (2)	182	14,778	8	-	0.65, -0.55	354
Na ⁺ /Na ⁺ /Na ⁺	182	14,778	-	8	0.25, -0.55	301
Na ⁺ /Na ⁺ /Na ⁺ (2)	182	14,778	-	8	0.55, -0.55	332
Na ⁺ /K ⁺ /K ⁺	182	14,778	2	6	0.65, -0.55	221
Na ⁺ /K ⁺ /K ⁺ (2)	182	14,778	2	6	0.25, -0.55	215
K ⁺ /Na ⁺ /Na ⁺	182	14,778	1	7	0.65, -0.55	289
K ⁺ /Na ⁺ /Na ⁺ (2)	182	14,778	1	7	0.25, -0.55	330

Table C.3: Overview over umbrella sampling simulation parameters and starting configurations.

²⁸ Wojtas-Niziurski et al. (2013).

Two-dimensional PMFs were calculated using self-learning adaptive umbrella simulations (US) starting from several starting configurations (Table C.3 and Figure D.12) differing in their initial ion placement: K⁺/K⁺ (2x), K⁺/K⁺/K⁺ (2x), Na⁺/Na⁺/Na⁺ (2x), Na⁺/K⁺/K⁺ (2x), and K⁺/Na⁺/Na⁺ (2x)²⁸. A harmonic biasing potential with a force constant of $k=1,000 \text{ kJ mol}^{-1} \text{ nm}^{-2}$ was applied to the z -coordinates relative to the COM of oxygens of C478 and I480 ($z=0 \text{ nm}$) for the two CVs.

For the two ions systems (K⁺/K⁺), US boundaries were set to -0.35 to 1.85 nm and -1.55 to 0.55 nm for z_1 and z_2 , respectively. For the three ions systems, different US boundaries were used with a maximal range of -0.35 to 2.45 nm and -2.25 to -0.35 nm for z_1 and $z_{2,3}$, respectively. For all systems, the grid spacing between sampling points was 0.1 nm . Simulations were run for at least 5 ns using the NVT ensemble and the first 0.5 ns of each window was omitted from analysis. Additional longer simulations were run at regions with low sampling efficiency and along the MFEPs when required.

The results of two individual US runs with matching ion species were unbiased together using WHAM with 100×100 bins and a convergence tolerance of $10^{-6} \text{ kJ mol}^{-1}$ ²⁹. The error of the WHAM calculation was estimated via bayesian bootstrapping (100 runs). The total number of individual umbrella simulations used for unbiasing were 444 (K⁺/K⁺), 715 (K⁺/K⁺/K⁺), 633 (Na⁺/Na⁺/Na⁺), 436 (Na⁺/K⁺/K⁺), and 619 (K⁺/Na⁺/Na⁺).

Possible one-dimensional free energy paths were extracted from interpolated 2D PMFs via the nudged elastic band (NEB) method and ranked according to their energy³⁰. Representative snapshots of individual configurations along the pathways were extracted from US simulations by clustering trajectories based on the coordinates of z_1 and z_2 or z_1 and $z_{2,3}$, respectively.

²⁹ Kumar et al. (1992); Bauer (2020).

³⁰ Henkelman and Jónsson (2000).

CHAPTER D

Additional Data

D.1 G391C/S/D ADDITIONAL DATA

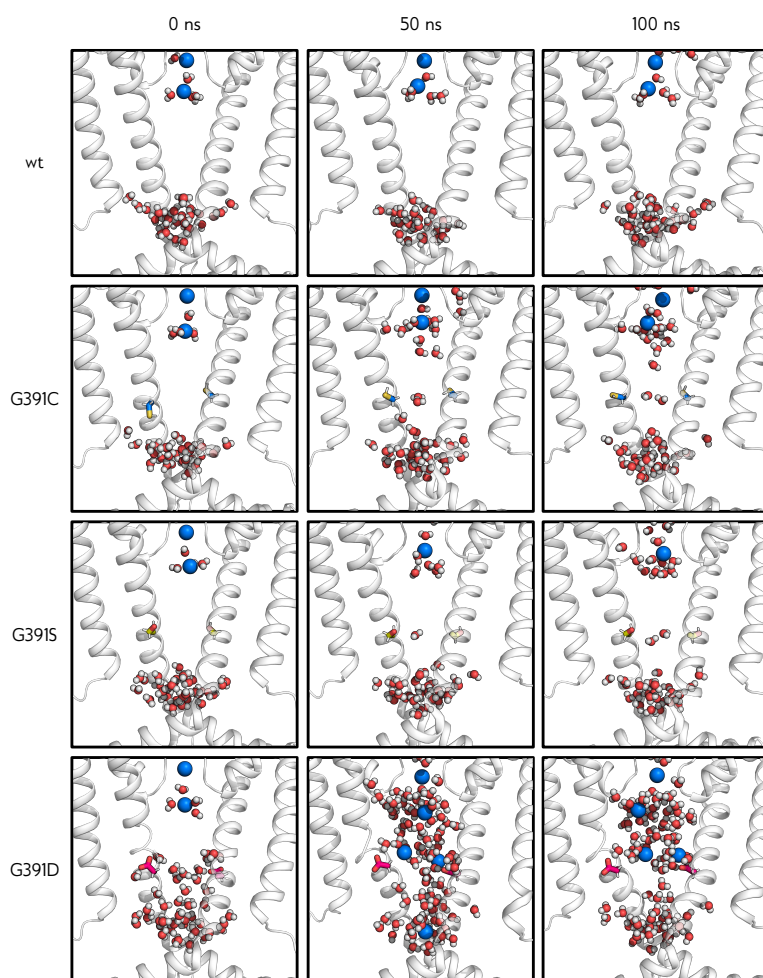


Figure D.1: Snapshots from MD simulations of HCN1_{wt} and HCN1_{G391C/S/D} after 0, 50 and 100 ns of simulation. The cavity and internal gate are shown as white cartoon from the side perspective with water molecules and ions as red/white and blue spheres, respectively. For clarity, only two of the four subunits of HCN1 and only water molecules in proximity to the pore axis are shown.

Figure D.2: C_{α} RMSD of HCN1_{wt} and $\text{HCN1}_{\text{G391C/S/D}}$.

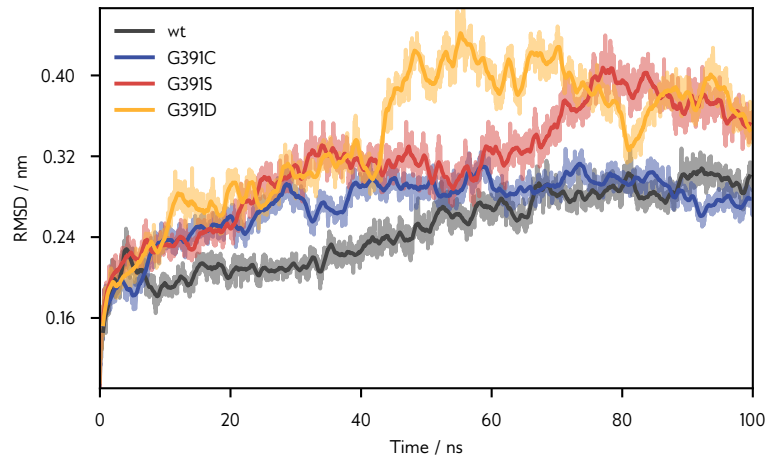
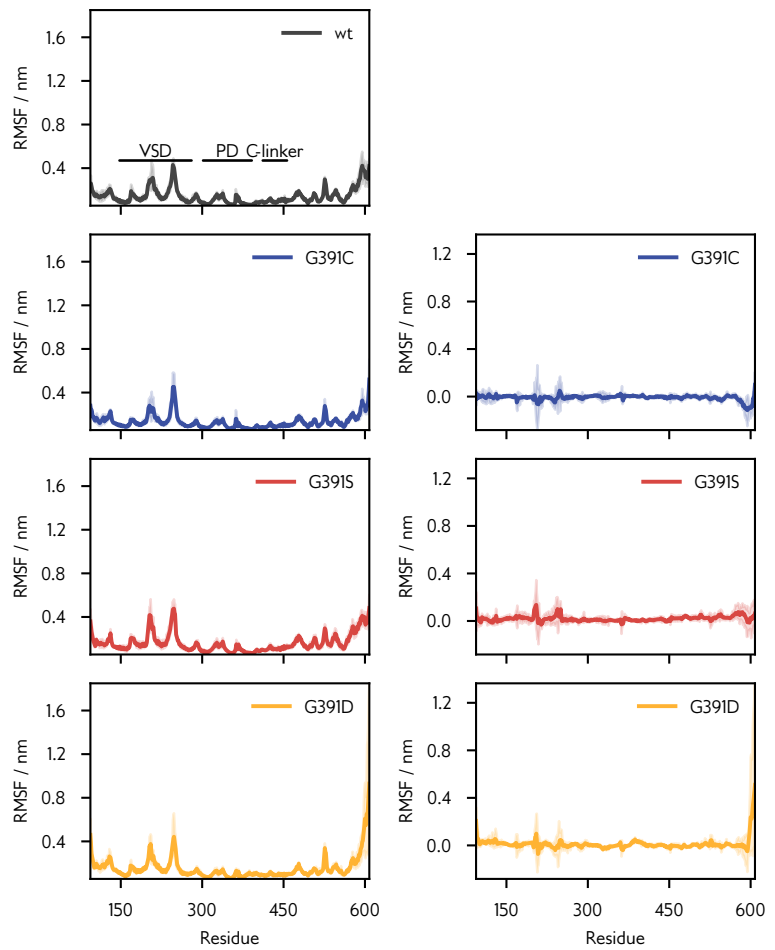


Figure D.3: Protein RMSF of HCN1_{wt} and $\text{HCN1}_{\text{G391C/S/D}}$ averaged over all four sub-units.



D.2 G391D ADDITIONAL DATA

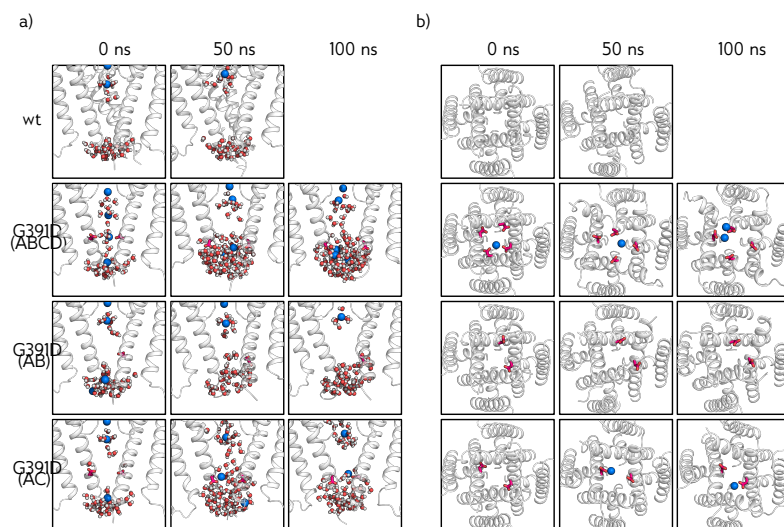


Figure D.4: Snapshots from MD simulations of HCN1_{TMD,wt} and HCN1_{TMD,G391D} with the mutation in different subunits after 0, 50 and 100 ns of simulation. The cavity and internal gate are shown as white cartoon from the side perspective with water molecules and ions as red/white and blue spheres, respectively. For clarity, only two of the four subunits of HCN1 and only water molecules in proximity to the pore axis are shown.

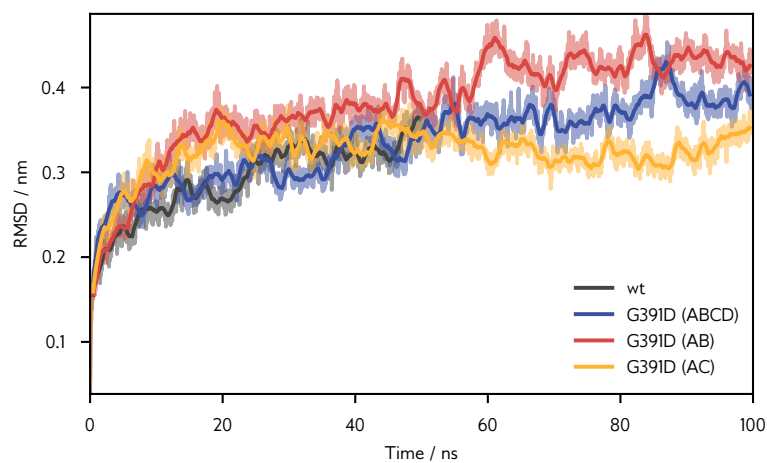
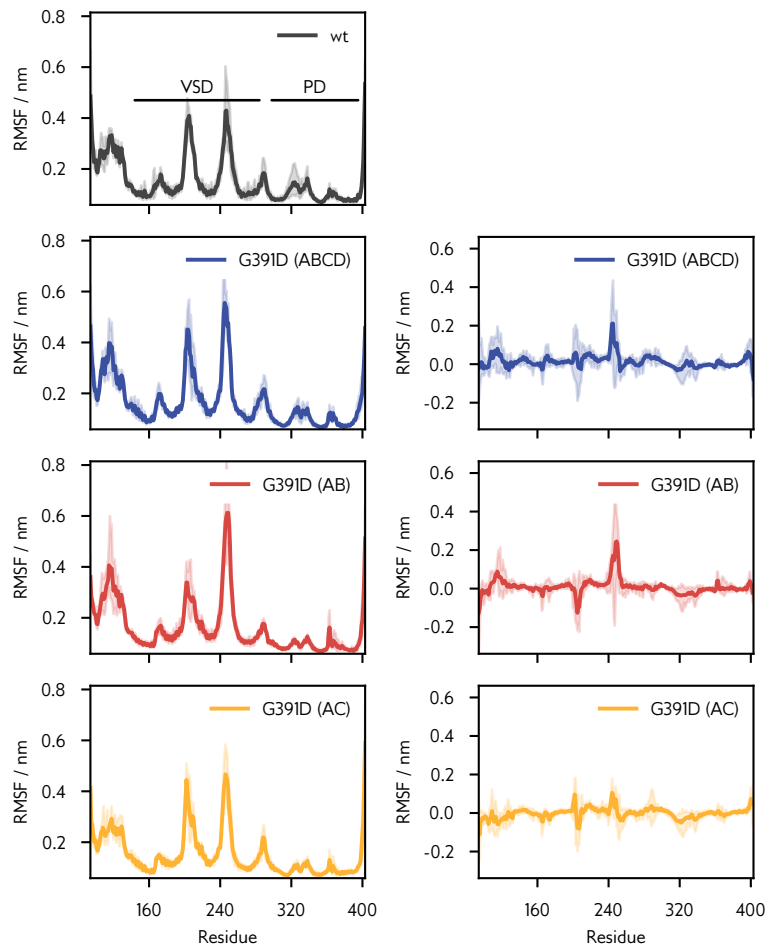


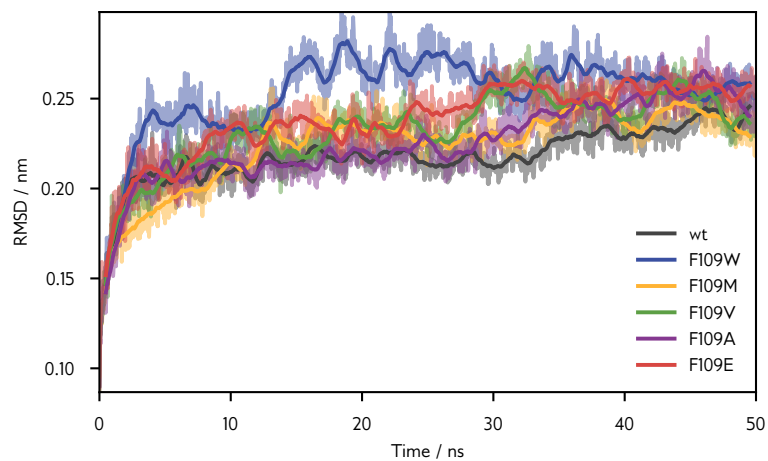
Figure D.5: C_α RMSD of HCN1_{TMD,wt} and HCN1_{TMD,G391D} variants.

Figure D.6: Protein RMSF of $\text{HCN1}_{\text{TMD,wt}}$ and $\text{HCN1}_{\text{TMD,G391D}}$ variants.



D.2.1 F109W/M/V/A/E Additional Data

Figure D.7: C_{α} RMSD of HCN1_{wt} and $\text{HCN1}_{\text{F109W/M/V/A/E}}$.



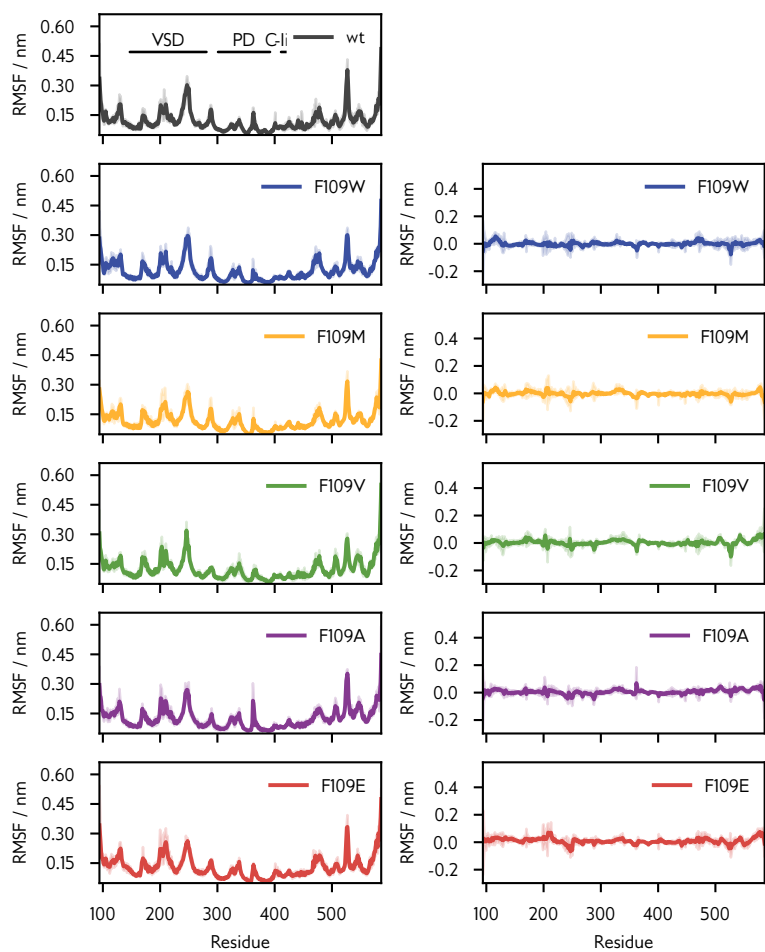


Figure D.8: Protein RMSF of HCN1_{wt} and HCN1_{F109W/M/V/A/E}.

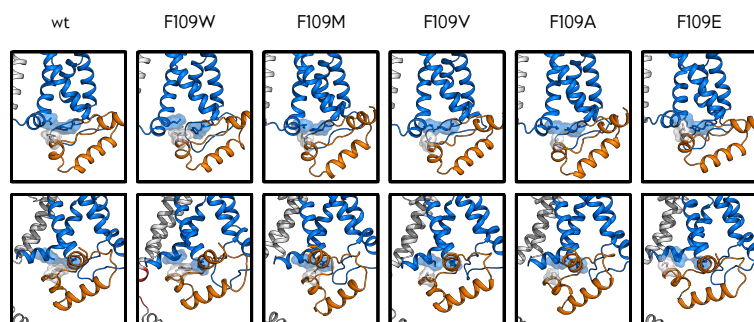
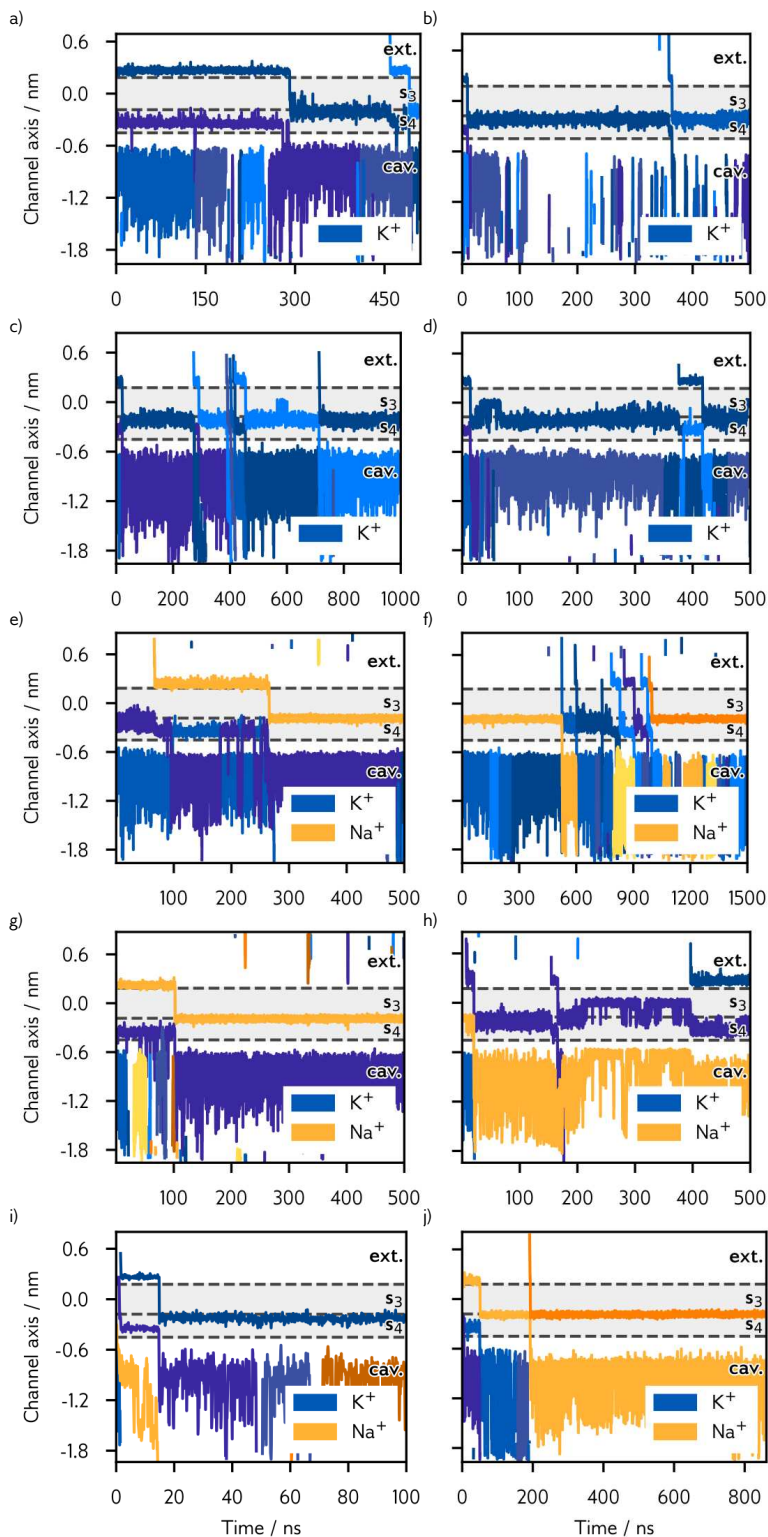


Figure D.9: Snapshots of the HCND and VSD for HCN1_{wt} and HCN1_{F109W/M/V/A/E}.

D.3 ION CONDUCTION SIMULATIONS

Figure D.10: K^+ and Na^+ conduction under different conditions: trajectory of K^+ and Na^+ ions along the channel axis. Different ions are shown in different shades of blue (K^+) and orange (Na^+). The shaded area corresponds to the SF and the position of carbonyl oxygens of residues L478 to L480 are indicated as dashed lines. Conditions: a) $V=-300$ mV, $c(K^+)=900$ mM
 b) $V=-500$ mV, $c(K^+)=150$ mM
 c) $V=-500$ mV, $c(K^+)=900$ mM
 d) $V=-500$ mV, $c(K^+)=900$ mM
 e) $V=-300$ mV, $c(K^+)=450$ mM, $c(Na^+)=450$ mM
 f) $V=-300$ mV, $c(K^+)=700$ mM, $c(Na^+)=450$ mM
 g) $V=-300$ mV, $c(K^+)=450$ mM, $c(Na^+)=450$ mM
 h) $V=-300$ mV, $c(K^+)=450$ mM, $c(Na^+)=450$ mM
 i) $V=-300$ mV, $c(K^+)=450$ mM, $c(Na^+)=450$ mM
 j) $V=-300$ mV, $c(K^+)=450$ mM, $c(Na^+)=450$ mM



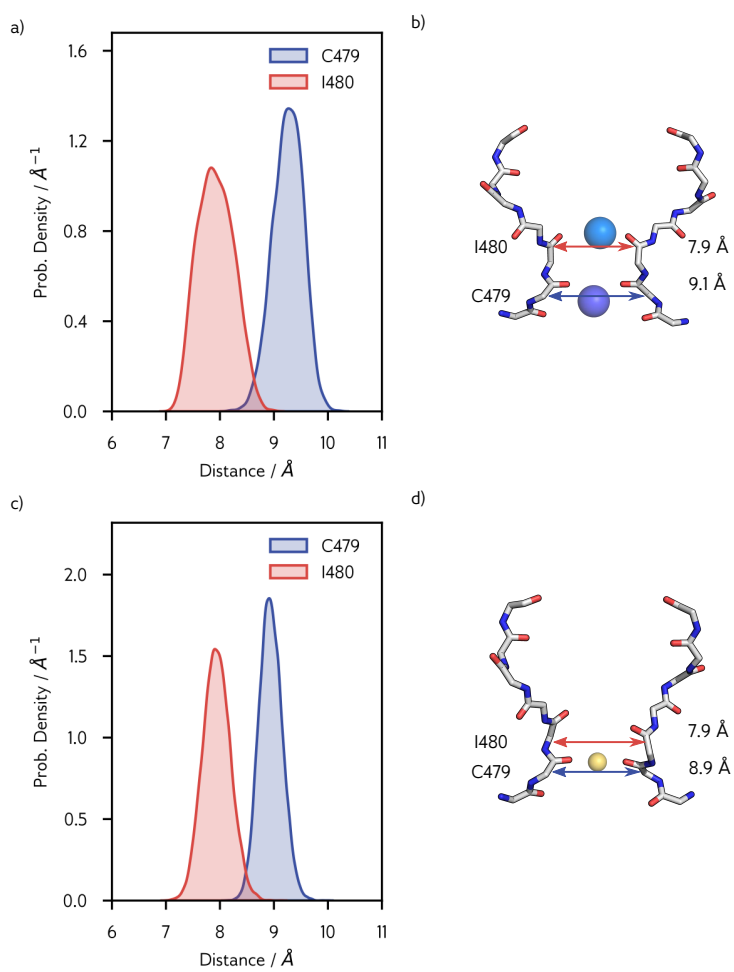
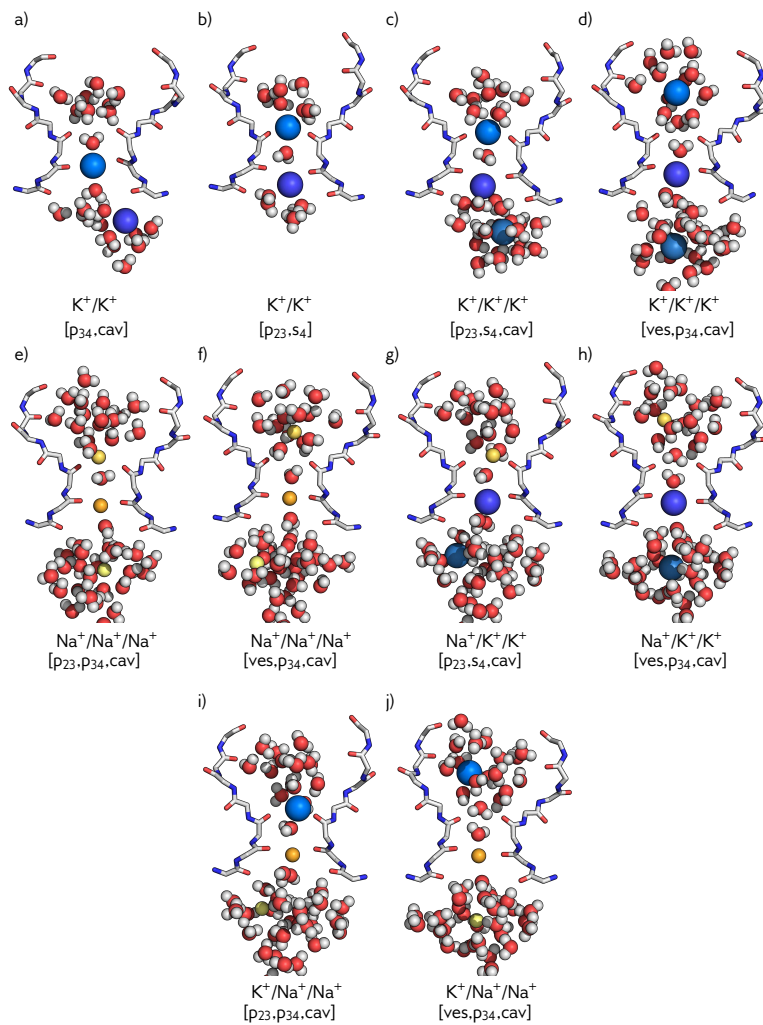


Figure D.11: The width of the SF backbone slightly depends on the bound ion, but not on the ion position. a) Probability density of the distance between opposing C_α atoms of C479 (blue) and I480 (red) during K⁺ conduction. Distances were measured for $t=[400;420]$ ns of the trajectory shown in Figure 6.8. Densities were smoothed using a Gaussian kernel density estimator. b) Snapshot with distances corresponding to the probability density maxima. c) Same as a), but for $t=[0;1000]$ ns of the sodium trajectory depicted in Figure 6.9. d) Same as b), but for c).

Figure D.12: Snapshots of the SF of starting configurations for self-learning adaptive umbrella simulations. The remaining protein ins not shown for clarity. K^+ and Na^+ ions are shown as blue and orange spheres, respectively. Water molecules in close proximity to ions are shown as red/white spheres and the SF is shown as colored sticks.



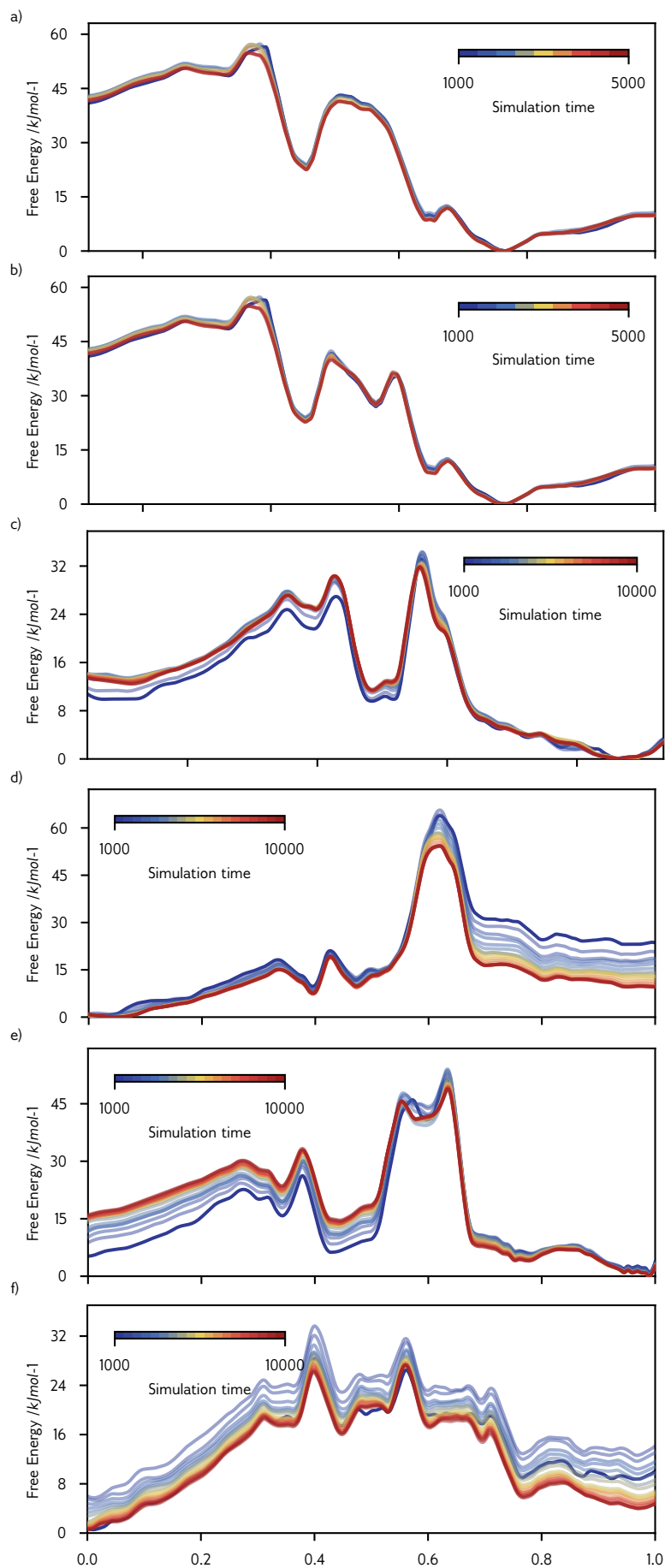


Figure D.13: Convergence of paths through 2D PMFs. Shown is the 1D free energy path along the reaction coordinate $\lambda=[O;I]$ as function of simulation time. Colors represent the free energy of the path through the PMF in 500 ps intervals (starting from 500 to 1000 ps). For each plot, the free energy path was extracted from the full simulation and was then superimposed on PMFs calculated with reduced simulation time. Systems: a-b) K^+/K^+ c) $K^+/K^+/K^+$ d) $Na^+/Na^+/Na^+$ e) $Na^+/K^+/K^+$ f) $K^+/Na^+/Na^+$.

Table D.1: Calculated free energy differences between minima $A_{i \rightarrow j}$ and the height of energy barriers for corresponding transitions $A_{i \rightarrow j}^\ddagger$ in the $\text{Na}^+/\text{K}^+/\text{K}^+$ system and $\text{K}^+/\text{Na}^+/\text{Na}^+$ system. The shown uncertainties are the result of 100 bayesian bootstrapping runs for the 2D PMF calculation.

Transition	Free Energy / kJ mol^{-1}	
	$\text{Na}^+/\text{K}^+/\text{K}^+$	$\text{K}^+/\text{Na}^+/\text{Na}^+$
$\Delta A_{1 \rightarrow 2}^\ddagger$	$+9.72 \pm 0.54$	$+8.60 \pm 0.19$
$\Delta A_{1 \rightarrow 2}$	-8.98 ± 0.54	-1.36 ± 0.20
$\Delta A_{2 \rightarrow 4}^\ddagger$	$+30.76 \pm 0.48$	$+11.15 \pm 0.27$
$\Delta A_{2 \rightarrow 4}$	$+26.75 \pm 0.49$	$+1.12 \pm 0.26$
$\Delta A_{4 \rightarrow 5}^\ddagger$	$+7.20 \pm 0.40$	$+1.18 \pm 0.21$
$\Delta A_{4 \rightarrow 5}$	-41.37 ± 0.24	-16.59 ± 0.24
$\Delta A_{5 \rightarrow 1}^\ddagger$	$+30.20 \pm 0.30$	$+17.96 \pm 0.17$
$\Delta A_{5 \rightarrow 1}$	$+23.60 \pm 0.30$	$+16.83 \pm 0.17$

Acknowledgements

The completion of this research work and my academic accomplishments would not have been possible without the help of many people. First of all, my thanks go to my supervisors Kay Hamacher and Gerhard Thiel for their guidance and feedback throughout this work as well as for funding my research. I would also like to express my gratitude to all my colleagues and collaborators: without them, this project would not have been possible. Last but not least, I am grateful for the support, encouragement, and patience of my family, my partner and my friends.

Thank you!

Ehrenwörtliche Erklärung

Ich erkläre hiermit, dass ich die vorliegende Arbeit entsprechend den Regeln guter wissenschaftlicher Praxis selbstständig und ohne unzulässige Hilfe Dritter angefertigt habe.

Sämtliche aus fremden Quellen direkt oder indirekt übernommenen Gedanken sowie sämtliche von Anderen direkt oder indirekt übernommenen Daten, Techniken und Materialien sind als solche kenntlich gemacht. Die Arbeit wurde bisher bei keiner anderen Hochschule zu Prüfungszwecken eingereicht.

Die eingereichte elektronische Version stimmt mit der schriftlichen Version überein.

Datum und Unterschrift